IMPROVING STRUCTURAL INTEGRITY OF DIRECT LASER DEPOSITED MCrAlY SUPERALLOYS BY ALLOY MODIFICATION AND HOT ISOSTATIC PRESSING

By

Aaron Michael O'Neil

A DISSERTATION

Submitted to
Michigan State University
in partial fulfillment of the requirements
for the degree of

Mechanical Engineering – Doctor of Philosophy

2023

ABSTRACT

Historically, engineers and their designs have been limited by what could be manufactured using conventional methods. The need for increased performance, efficiency, and thermal stability of mechanical systems is increasing demand for highly complex metal components made from specialty alloys. Conventional manufacturing is not a viable option to fabricate these complex components and/or materials and metal additive manufacturing processes are required to fill the demand. A portion of this demand is filled by finding new applications and manufacturing processes for existing materials.

The dual phase, β and γ/γ′ [where β = NiAl, γ = Ni(Co, Cr), and γ′ = Ni_3Al], MCrAlY (M = Ni and/or Co) family of superalloys exhibit several beneficial high-temperature (>1000 °C) strength and corrosion resistance properties which makes them ideal candidates for protecting components from harsh environments where a combination of high temperature corrosion, abrasion, and extreme loading are encountered. These alloys are difficult to manufacture by any process and can currently only be manufactured as thin coatings using particle spray, vapor deposition, or laser cladding techniques. While prior studies report laser fabrication of these materials in coating and cladding configurations, bulk structures have not been realized. MCrAlY alloys have been traditionally limited to coating applications due their propensity to hot crack during bulk manufacturing. Although aluminum is necessary for corrosion resistance in MCrAlY alloys, it also promotes the formation of β-NiAl intermetallic phases which cause microstructure embrittlement and increase an alloys susceptibility to brittle cracking induced by thermo-mechanical fatigue. This tendency to crack from thermo-mechanical fatigue is of importance for additive manufacturing processes because thermal gradients and stresses are constantly changing within a deposition during fabrication.

In order to fabricate bulk, complex structures from difficult to process materials in a reasonable amount of time, an additive manufacturing process such as directed energy deposition (DED) must be used. DED is a good candidate for this application because it is a freeform additive manufacturing process which features high deposition rates, relatively good dimensional accuracy, build volumes on the order of tens or hundreds of centimeters, and the ability to process difficult materials. This dissertation investigates the feasibility of fabricating bulk structures from an alumina forming NiCoCrAlY superalloy (tradename “Amdry 386”) using laser-DED, and develop heat treatments necessary to improve the structural integrity of laser-processed MCrAlY components.

This dissertation is dedicated to my family, friends, colleagues, and pets, without whom, none of this would have been possible… Thank you!

ACKNOWLEDGEMENTS

I would like to thank …

- My Ph.D. Advisor, Dr. Himanshu Sahasrabudhe for your guidance, patience, and support throughout the years.
- My Ph.D. Committee Members, Dr. Himanshu Sahasrabudhe (Chair), Dr. Andre Benard, Dr. Haseung Chung, and Dr. Carl Boehlert for your service.
- The staff at the Center for Advanced Microscopy at MSU, and Michigan Center for Materials Characterization $(MC)^2$ at U of M.
- Dr. Rohini Bala-Chandran and Mr. Bryan Kinzer for co-authorship and Thermo-Calc modeling.
- Dr. Lloyd Hackel and Mr. Carlos Nava for residual stress analysis.
- Mr. Chad Beamer for HIP'ing services.
- Dr. Alexandra Zevalkink for access to XRD analysis facilities.
- Dr. Stanley Flegler for access to SEM and Keyence microscopes.

* This work was supported by the Department of Energy Advanced Research Projects Agency-Energy (ARPA-E) under cooperative agreement DE-AR0001123 with Michigan State University.

TABLE OF CONTENTS

CHAPTER 1:

INTRODUCTION

1.1 Background

Historically, engineers and their designs have been limited by what could be manufactured using conventional methods. The need for increased performance, efficiency, and thermal stability is increasing demand for highly complex metal components made from specialty alloys. Conventional manufacturing is not a viable option to fabricate these complex components and/or materials and metal additive manufacturing processes are required to fill the demand. A portion of this demand is filled by finding new applications and manufacturing processes for existing materials.

Conventional manufacturing processes are capable of fabricating semi-complex structures, but specialized machinery and a series of different operations such as hot/cold working, subtractive machining, heat treatment, and assembly are required [1-4]. Each additional operation increases the lead time and manufacturing cost for a component [4]. Machines and tooling for conventional manufacturing processes require a large initial investment and their production, shipping, and implementation is very slow. Once operational, conventional manufacturing production lines can produce mass quantities of components in a relatively short period of time, but if a lesser number of components is desired, it may not be time or cost effective to use conventional manufacturing techniques, and AM should be considered. Additive manufacturing processes focus on minimizing the number of machines, operations, and resources such as time, energy, materials, labor, and infrastructure needed to fabricate a component. In contrast with conventional manufacturing techniques, additive manufacturing machines do not require part specific tooling which allows for

the low volume production of complex parts such as customized medical implants, aerospace components, and functional coatings from difficult to process materials with a relatively short lead time [5-18]. Although AM machines also require a large initial investment, their cost pales in comparison to the cost of part specific tooling, multiple large machines, and infrastructure required for conventional manufacturing processes. Due to the high cost of feedstock and low throughput, additively manufactured components are very expensive and the cost it takes to fabricate each component does not reduce as the desired quantity of parts increases as it does with conventional manufacturing. While metal additive manufacturing processes have the ability to produce complex parts from difficult to process materials for niche applications, conventional manufacturing processes still dominate the manufacturing industry with its existing infrastructure, mass production quantities, and low cost per part [19]. Conventional manufacturing processes leave room for improvement in part complexity, lead time, overall process cost, efficiency, and their limited material selection. Metal additive manufacturing processes are maturing and further demand will enable future development for reducing cost per part, improving production speed and throughput, and manufacturability of an even wider range of materials. Extensively tested metal AM processes such as DED and PBF are poised to disrupt the manufacturing industry.

The MCrAlY (M = Ni and/or Co) family of superalloys exhibit several superior high-temperature (600 - 1100 °C) [20-21] properties including mechanical strength, creep resistance, and hot corrosion resistance which makes them ideal candidates to be used as protective coatings on components exposed to extreme thermal and mechanical loading, and hot corrosion environments such as those such as those encountered in gas turbines, oil and gas extraction equipment, and nuclear irradiation environments [22-23]. Many such alloy chemistries have been developed as bond coats in thermal barrier coating (TBC) systems used to protect gas turbine

components such as blades, stators, and rotors [24-26]. Although extremely useful, these alloys are difficult to manufacture by conventional processes, and currently can only be manufactured as thin coatings using particle spray, vapor deposition, or laser cladding techniques which can yield high deposition rates (excluding vapor deposition) and high structural integrity with minimal defects [27-31]. MCrAlY alloys have been traditionally limited to coating applications due their propensity to crack during bulk manufacturing. Although aluminum is necessary for corrosion resistance in MCrAlY alloys, it also promotes the formation of β-NiAl intermetallic phases which cause microstructure embrittlement and increase an alloys susceptibility to brittle cracking induced by thermo-mechanical fatigue. This tendency to crack from thermo-mechanical fatigue is of importance for additive manufacturing processes because thermal gradients and stresses are constantly changing within a deposition during fabrication. The improved manufacturability of previously difficult to manufacture materials such as MCrAlY alloys, which exhibit improved mechanical properties and corrosion resistance, will allow design engineers to increase performance and thermal stability of mechanical systems [32-39]. Gas turbine components fabricated completely from MCrAlY alloys would exhibit greater high temperature corrosion resistance than any current Ni-based laser fabricable alloys, and mechanical properties similar to or greater than common aerospace component base materials such as MAR-M247 (CMSX alloy), Inconel, and René alloys [40-41]. Such advancements would enable fabrication of components that could withstand higher service temperatures, and operational loads for longer periods of time.

While prior studies report laser fabrication of MCrAlY alloys in coating and cladding configurations, bulk structures (thickness > 2 mm) have not been realized. In order to fabricate bulk, complex structures from difficult to process materials in a reasonable amount of time, an additive manufacturing process such as directed energy deposition (DED) must be used. DED is a

good candidate for this application because it is a versatile, freeform additive manufacturing process which features high deposition rates, unmatched 3D capabilities, relatively good dimensional accuracy, build volumes on the order of hundreds or thousands of millimeters, and the ability to manufacture relatively defect-free, complex components from difficult to process materials [42-43].

Laser-DED fabrication of bulk structures from a commercially available, hot corrosion resistant NiCo-based coating alloy, tradename "Amdry 386" (A386), was unsuccessful and hot cracking was observed. The laser processed microstructure became embrittled by the formation of relatively high amounts of the β-NiAl intermetallic phase. The alloys susceptibility to hot cracking and residual stresses formed by rapid melting and solidification enabled the formation of cracks and delaminations in the bulk material during laser-DED fabrication. To overcome the embrittlement and relieve residual stresses, this study was designed to systematically evaluate the effects of modifying the composition of the selected A386 alloy and increasing the structural integrity of laser processed structures through hot isostatic pressing (HIP). Amdy 386 (A386) feedstock powder (predominantly β with lesser γ/γ') was modified by adding successive amounts, (10, 20, 30% by weight), of a powdered 80%Ni-20%Cr (NiCr) alloy (mainly γ/γ' phase). The additions created three new compositions of A386 and NiCr alloys – A386 + 10%, 20%, and 30% NiCr which were subsequently processed using laser-DED. While cutting the mixture coupons for further analysis, the residual stresses within the material caused warping and cracking which rendered the coupons useless except for metallographic analysis. To relieve the residual stresses and reduce the amount of internal defects, HIP treatments were investigated. Microstructural and phase analysis of all as-processed (AP) and HIP'd mixture coupons was conducted to investigate the effects of the chemical composition modifications and HIP treatments. Two sets of large

coupons were successfully fabricated from the A386 + 20% NiCr and A386 + 30% NiCr mixtures for residual stress measurements of coupons in the AP and HIP'd states, and to test the high temperature mechanical performance of HIP'd A386 + NiCr mixture alloys. This dissertation presents the modification of a nickel-based alumina forming coating alloy for bulk applications manufactured by laser-DED, and the development of post processing treatments to increase the structural integrity of laser processed superalloys. Post processting heat treatments to increase mechanical strength of HIP'd MCrAlY alloys is also explored.

1.2 MCrAlY Superalloys and Their Applications

MCrAlY (M = Ni and/or Co) superalloys possess several beneficial high-temperature (>1000 °C) properties including high mechanical strength, creep resistance, and corrosion resistance. MCrAlY's combination of superior strength and corrosion resistance at high temperatures make them ideal candidates for protecting components which are subjected to combined thermal and mechanical loads with simultaneous reactive environments such as those encountered in aerospace rocket engines, oil and gas extraction equipment, nuclear power generation, and most commonly, internal gas turbine components such as blades, vanes, stators seen in Figure 1 [44-46].

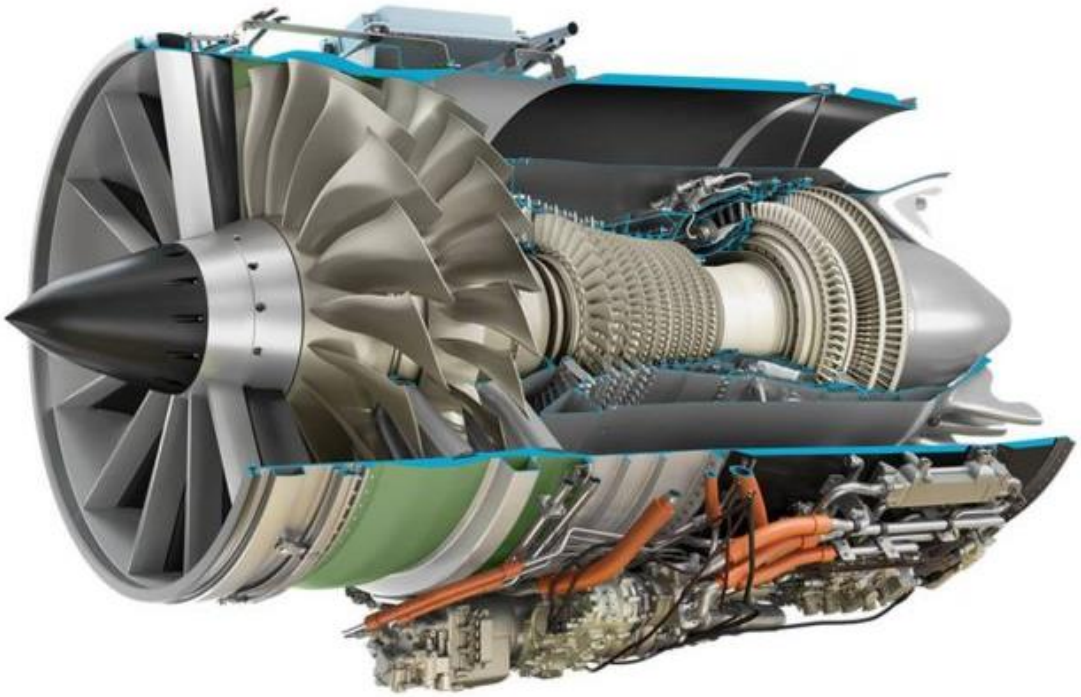

Figure 1: Aerospace jet turbine engine [47].

MCrAlY coating alloys exhibit a dual phase microstructure in which the brittle, Al-rich β phase is embedded in a matrix of the ductile γ/γ' phase (β = NiAl, γ = Ni(Co, Cr), and γ' = Ni_3Al). The MCrAlY family of superalloys exhibit superior hot corrosion resistance because of their high (> 6%) aluminum content which causes the formation of alumina during exposure to hot and corrosive environments. These alloys are designed to achieve an optimum balance between the corrosion resistance of the β phase and mechanical strength of the γ/γ' phase.

A majority of MCrAlY alloy chemistries have been developed as a bond coat material in layered functional coatings known as thermal barrier coatings (TBC). These coatings are used to protect underlying components from hot corrosion and insulate them from extremely high temperatures. TBC's such as those seen in Figure 2 are applied on superalloy components in two layers, the MCrAlY bond coat, and porous ceramic top coat. MCrAlY bond coats increase adhesion of the top coat to the underlying superalloy component, and protect the component from corrosion. During operation, a third layer known as a thermally grown oxide (TGO) film is

formed on the surface of the MCrAlY bond coat when aluminum from the bond coat reacts with oxygen at high temperatures. TGO's give thermal barrier coatings their ability to resist hot corrosion caused by sulfur, vanadium, and sodium salt impurities present in the turbine's fuel. The outermost layer of the TBC is a ceramic top coat which insulates underlying components from extreme heat and is the first line of defense against erosion and corrosion of the component. Porous top coats can reduce the superalloy substrate surface temperature by as much as 170 °C [48].

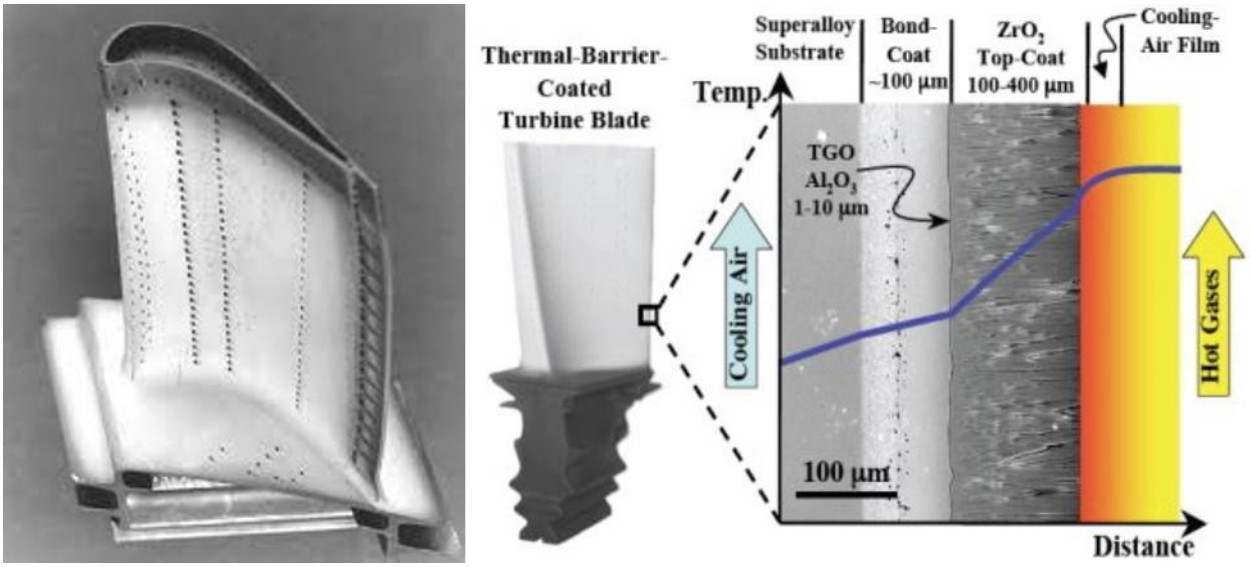

Figure 2: Jet turbine blade and thermal barrier coating (TBC) [49-50].

1.3 Fabricability of MCrAlY Alloys

The MCrAlY family of alloys used in cladding and functional coatings are typically deposited using particle spray, vapor deposition, or laser cladding methods. Particle spray processes can have relatively high deposition rates, but they have very low geometric accuracy and produce coatings with many defects such as porosity, lack of fusion, and inclusions if deposition parameters are not optimized. Vapor deposition processes create fully dense, defect free coatings, but have poor geometric accuracy and very low material deposition rate. The drawbacks from these modern coating fabrication processes make them unable to fabricate fully dense,

structurally sound, bulk, 3D structures in a reasonable amount of time. Therefore, it is necessary to find suitable processing routes for bulk (thicknesses > 2 mm) component fabrication of alloy chemistries that have been traditionally limited to thin coatings. Such advancements would enable fabrication of complex components that could withstand higher service temperatures, operational loads, and hot corrosion for longer periods of time. Prior studies have demonstrated the ability to successfully deposit defect free MCrAlY coatings using laser cladding techniques, but bulk structures have not been realized [51-55].

In contrast with particle spray and vapor deposition techniques, beam and arc based additive manufacturing technologies such as DED have been used for decades to quickly fabricate virtually defect free, near net shape structures with large (dimensions on the order of tens of cm) and complex 3D geometries from "weldable" superalloys. Weldable superalloys have less than 6% of Al and are generally used for their superior high temperature strength and ability to be cast into single crystal structures rather than corrosion resistance. Large amounts of Al causes the formation of relatively higher proportions of the Al rich β phase. The β phase causes microstructure embrittlement and increases an alloys susceptibility to brittle cracking induced by thermo-mechanical fatigue. This susceptibility is of importance for fabricating MCrAlY alloys using beam or arc based additive manufacturing processes because thermal gradients and stresses are constantly changing within a deposit during fabrication. Although it is possible to fabricate components from weldable superalloy compositions using additive manufacturing processes, the rapid melting and solidification rates encountered in the DED process cause immense residual stresses within a deposit. These thermal gradients and residual stresses cause hot cracking and delaminations in unweldable alloys during deposition. The β phase also reduces the low temperature fracture toughness which is exacerbated by residual stresses imparted in deposits

during complete cooling. This combination of reduced fracture toughness and residual stresses often cause severe cracking in structures during fabrication, removal from the baseplate, or post process machining. To eliminate this cracking, high aluminum content MCrAlY structures fabricated using beam or arc based AM processes should be annealed to relieve residual stresses before machining.

1.4 Down Time and Repair Cost Reduction

As with all coatings, TBC's inevitably incur damage, wear out, or flake off during operation. After this happens, the component needs to be recoated, repaired, or replaced to avoid catastrophic damage to the mechanical system. These operations are very expensive due to the high costs of new components, downtime, skilled labor, and specialized machinery needed to repair the coatings. Instead of recoating and repair, it may be more cost effective to fabricate complete components from coating materials to extend a component's lifespan. In theory, components fabricated completely from the MCrAlY coating alloys would not need to be recoated or replaced as often as the traditional coated superalloy components. Since bulk components of MCrAlY are difficult to manufacture by conventional methods, additive manufacturing processes such as DED need to be utilized for this application. Gas turbine components fabricated completely from MCrAlY alloys would exhibit greater high temperature corrosion resistance than any Ni-based laser processable alloys, and mechanical properties similar to common aerospace component base materials such as CMSX, Inconel, and René alloys [56-57]. Although the corrosion rate would increase with the reduction of aluminum required for successful beam or arc based AM fabrication, it may be possible to offset the effects of an increased corrosion rate and loss of efficiency with the reduction of downtime and recoating costs incurred by maintaining a

traditionally MCrAlY coated component throughout its lifespan. Reducing the frequency of system maintenance would lessen downtime and decrease component replacement or repair costs.

Additive manufacturing (AM) techniques aim to address the limitations associated with conventional manufacturing methods [58-60]. Conventional manufacturing processes can fabricate semi-complex structures, but multiple machines and operations [61-63] such as hot/cold working, heat treatment, subtractive machining, and assembly are necessary to produce a complete component. Each additional machine and/or operation increases the lead time and manufacturing cost per component [2, 64-65]. The specialized machines and associated tooling required for conventional manufacturing processes are expensive and require a large initial investment. Conventional manufacturing processes are often designed to produce large batches of a single component with a lengthy lead time. The large batches and extended lead times allow manufacturers to reduce the overall manufacturing cost of each component through careful planning and mass production. If lesser amounts of components are desired in a short period of time, it may not be cost or time effective to use conventional manufacturing processes and AM processes should be considered.

1.5 Structural Integrity

Structural integrity is the ability of a structure or component to withstand its intended loading without failure due to fracture or deformation. In the following studies, structural integrity is used to describe the state of a structure after fabrication or post processing machining. Defects and factors which negatively affect structural integrity are cracks, large porosity, lack of fusion, residual stresses, and thermo-mechanical fatigue. During fabrication, metallic components often develop defects and residual stresses due to sub-optimal processing parameters, hot/cold forming, and unequal thermal gradients. These defects and residual stresses are difficult to avoid during

metal manufacturing processes, but minor defects and residual stresses can be removed from a component by post processing heat treatments. Large defects such as open fractures are generally irreparable without substantial machining and/or welding operations and lead to the scrapping of components. If a manufacturing process is continually producing scrap components, significant changes need to be made to the process or modifications to the metal alloy need to be made to allow for increased fabricability.

CHAPTER 2:

STATE OF THE ART

2.1 Introduction

The ASTM standards define additive manufacturing, also known as 3D printing, as "a process of joining materials to fabricate objects from 3D model data, usually layer upon layer, as opposed to subtractive manufacturing methodologies" [66]. With the maturation of metal additive manufacturing processes, applications have evolved from rapid prototypes with minimal functionality to fully functional components used in safety-critical applications. The ability to fabricate functional and complex components with few design limitations has completely transformed the manufacturing industry. Previously, difficult to process materials such as Ni, Co, Cr, or W alloys, have been developed for improved mechanical properties and corrosion resistance which allow designers to increase performance and thermal stability of mechanical systems. Metal additive manufacturing processes can now produce complex components from these materials for a wide variety of applications in the aerospace [67-69], medical device and implant [70-72], nuclear energy [73-75], oil and gas refinement [76-78], and defense [79-81] industries.

2.2 MCrAlY Manufacturing Processes

2.2.1 Particle Spray Processes

Particle spray processes are manufacturing techniques which are used to deposit protective coatings on substrates or components. Particle spray processes are split into three categories, thermal spray, plasma spray, and cold spray. The thermal spray and plasma spray processes utilize fuel gas combustion or a plasma jet to melt and deposit powder whereas the cold spray process utilizes a supersonic nozzle to accelerate and deposit solid powder particles on a substrate. These processes have very high deposition rates and can deposit metals, ceramics, or

combinations of the two. Particle spray coatings adhere well to their substrates through different combinations of mechanical interlocking, metallurgical bonding, and chemical bonding. Particle spray processes are capable of producing near full density coatings, but non-optimized coating parameters can cause defects such as porosity, inclusions, and unmelted particles. Examples of coatings produced by the three particle spray processes are shown in Figure 3. Particles deposited by spray processes deform when they impact a substrate

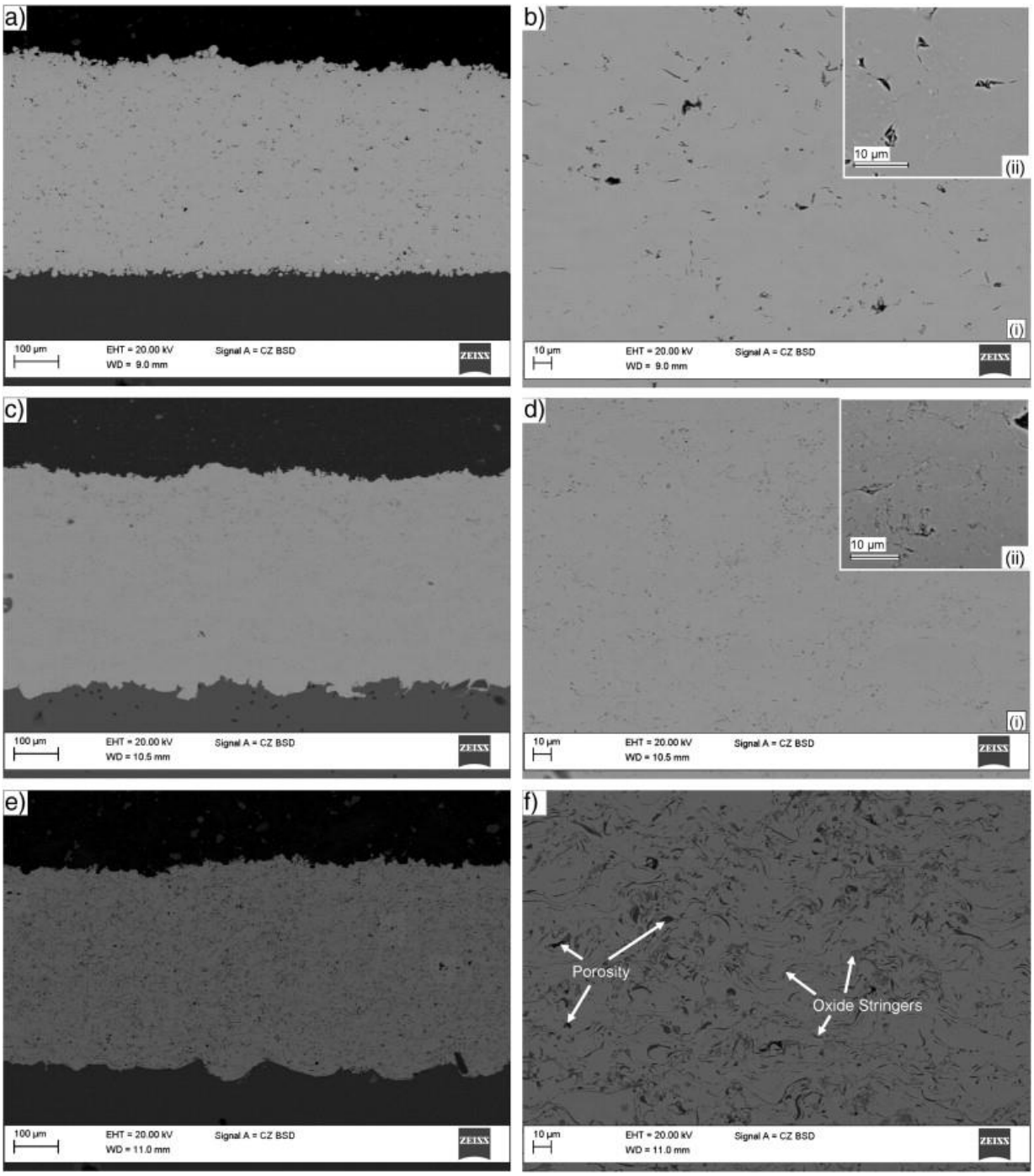

Figure 3: Particle spray coatings, (a-b) cold spray coating with 1.0 ± 0.3% porosity, (c-d) thermal spray coating with 0.5 ± 0.1% porosity, (e-f) plasma spray coating with 5.3 ± 0.5% porosity [82].

surface or previously deposited particles forming a splash or disk shaped "splat." Particle spray techniques are rough and robust processes which gives them poor geometric accuracy. Due to the lack of geometric control, these processes are only used in cladding or coating applications where

thickness is the only dimension of interest. Metal spray coatings can range in thickness from several microns to several hundred microns.

2.2.2 Vapor Deposition

Vapor deposition processes are thin coating processes in which materials in a vapor state are applied on a substrate by means of condensation or chemical reaction. Vapor deposition processes are split into two different categories, physical vapor deposition (PVD) and chemical vapor deposition (CVD). Vapor deposition processes require low pressure so coating application is often conducted inside a vacuum chamber. In physical vapor deposition, a coating material is heated until vaporization and then condenses on a relatively cooler substrate surface forming a coating [83]. The PVD process can produce inexpensive coatings [84] with superior adhesion strength [85]. PVD has a low material deposition rate with coating thickness growth rates only reaching 100 µm/min. PVD coatings vary from 2 µm to hundreds of microns thick. A diagram of the PVD process and microstructure of a PVD coating is shown in Figure 4. In the chemical

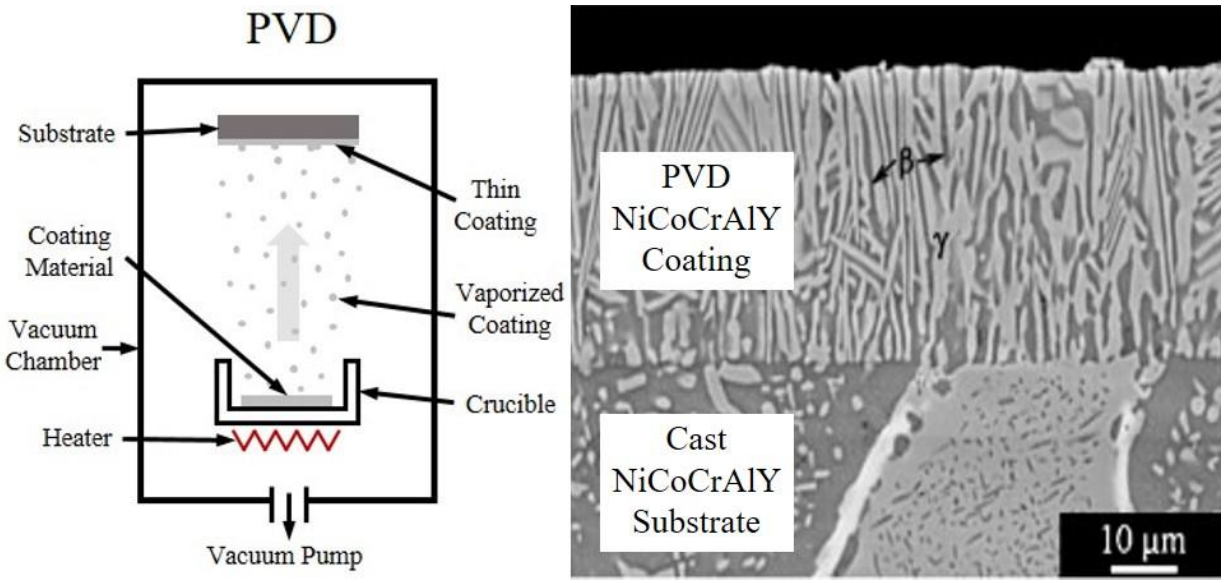

Figure 4: Physical vapor deposition process diagram and PVD coating [86].

vapor deposition process, vaporized precursor molecules chemically react with a heated substrate onto which the coating is deposited [87]. In this chemical reaction, precursor molecules decompose

to form the coating material while gaseous molecules containing carrier gas atoms and surface reaction products are removed by a vacuum pump [88]. The CVD process produces virtually fully dense coatings with superior bond strength such as that seen in the micrograph of Figure 5. CVD processes are expensive due to the high cost of equipment and precursor gases [89]. CVD processes produce coatings thicknesses varying from 1 nm to hundreds of microns, but they have very low material deposition rates with coating thickness growth only reaching 1-2 µm/min [90-91].

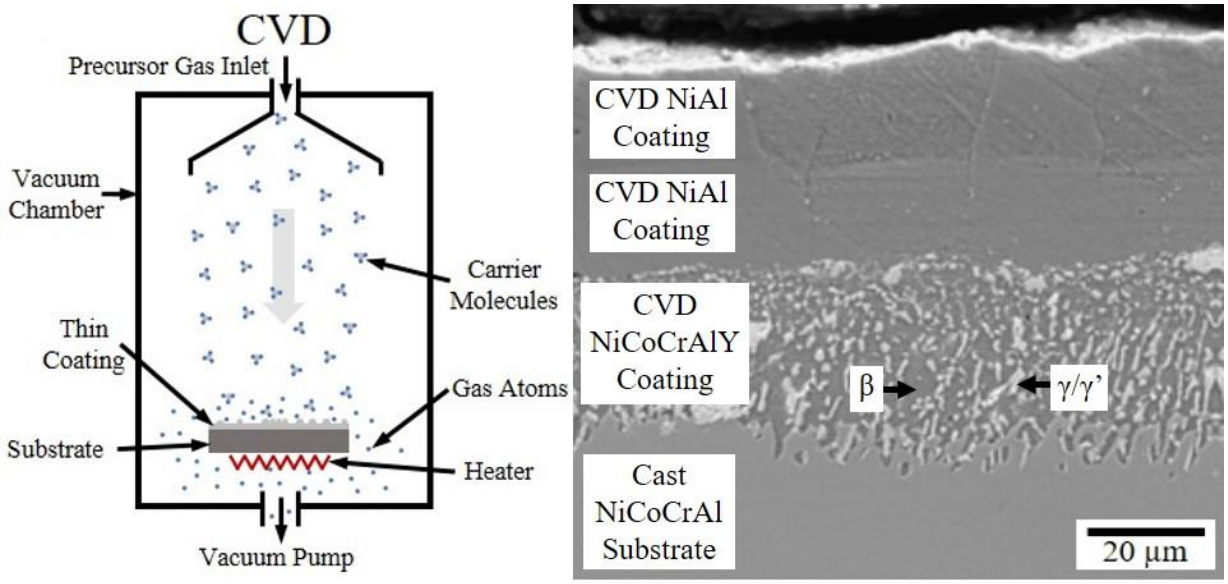

Figure 5: Chemical vapor deposition (CVD) process diagram and CVD coating [92].

2.2.3 Laser Cladding

Laser cladding is a coating process in which metal or ceramic coating material in powder or wire form is melted and deposited on the surface of a part. Laser cladding processes have high deposition rates and can quickly produce virtually fully dense coatings with less than 1% porosity [93], such as those seen in Figure 6. Laser claddings range in thickness from tens of μm to tens of mm [94]. In the past, laser cladding processes were limited by their geometric capabilities, but the implementation of cladding deposition heads combined with multiple axis of motion has allowed cladding techniques to go from simple coating applications to the fabrication of complex 3D components. Advancements in cladding technologies have led to the development of freeform additive manufacturing techniques such as directed energy deposition (DED).

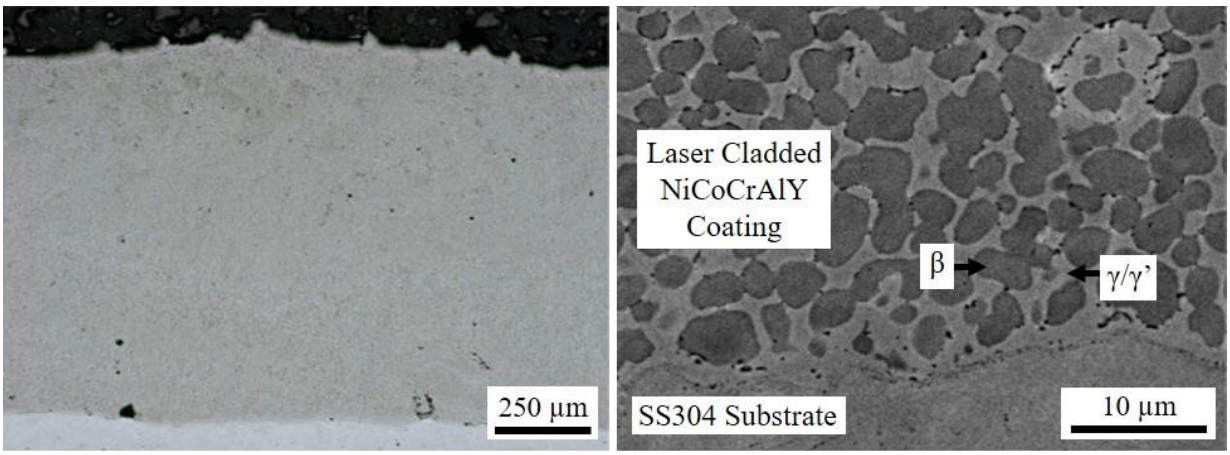

Figure 6: Laser cladded NiCoCrAlY microstructure [95].

2.3 Directed Energy Deposition (DED) - Bulk Metal Additive Manufacturing

Directed energy deposition (DED) is a freeform AM process which utilizes a heat source such as laser, electron beam or electric arc to create a melt pool into which powder or wire feedstock is fed. As feedstock is fed into the melt pool, the heat source is scanned across a substrate or previously deposited material to form a new deposited layer. After each layer scan, the energy source and material feeder are moved up in small increments equal to the deposited layer thickness.

Successive scans deposit material in a layer-by-layer fashion and a 3D component is formed. A diagram of the DED process is shown in Figure 7.

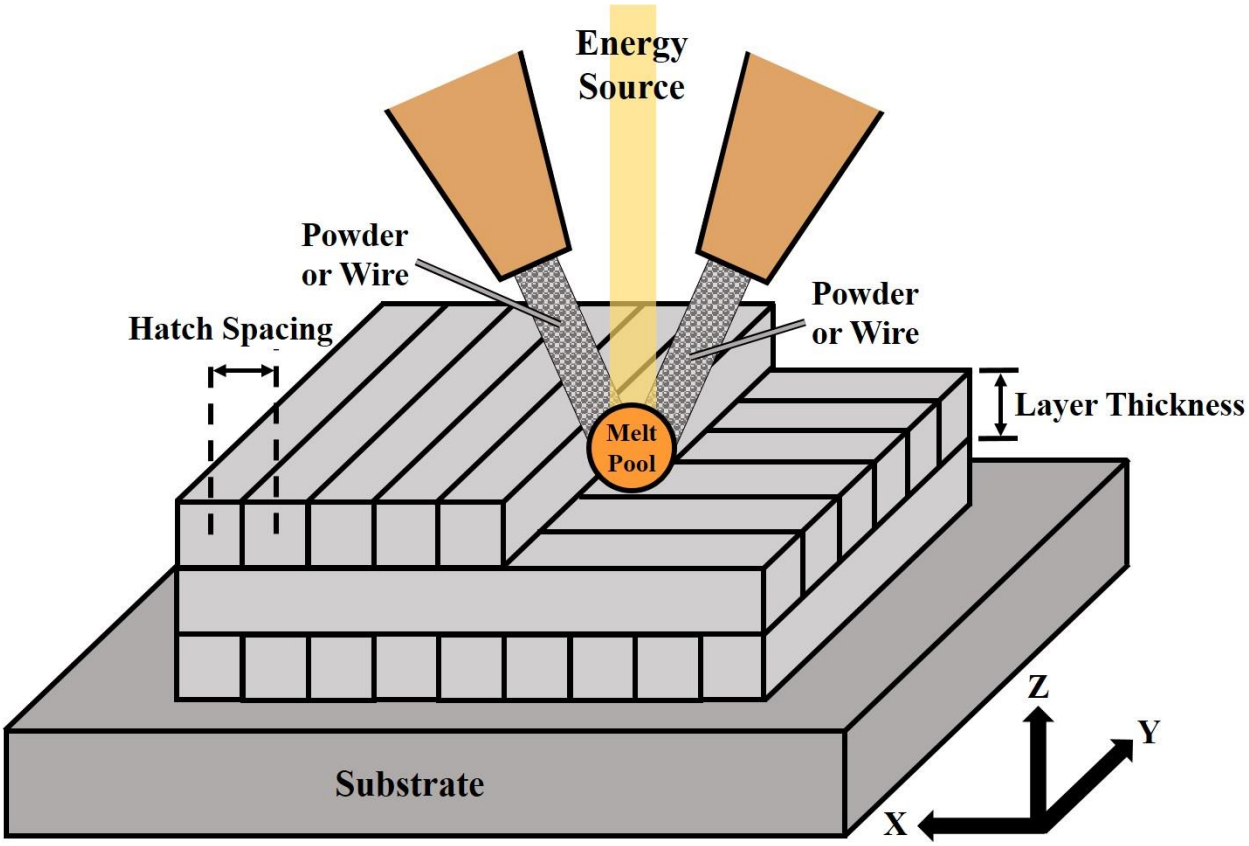

Figure 7: Directed energy deposition (DED) process diagram.

DED is a versatile manufacturing technique with nearly limitless applications that offers the advantages of high deposition rates [96], high feedstock utilization efficiency, rapid fabrication of near net shaped 3D components [97], large build envelopes [98], the ability to fabricate functionally graded and multi-material structures, and the ability to refurbish worn or damaged components [99]. The DED process, and its commercial variants such as the LENS^{TM} technique, have been used for processing difficult to manufacture materials such as ceramics, metal-ceramic mixtures, Ni, Co, Cr, Ti, and refractory alloys. DED has been utilized extensively to research and develop novel metallic alloys and fabricate near net-shape 3D structures which conventional methods cannot manufacture from previously unprocessible materials. DED is

scalable process so it can fabricate structures which have dimensions of a few millimeters or a few meters just by changing the laser power density, feedstock feed rate, and CAD model slicing parameters.

2.4 Hot Isostatic Pressing (HIP)

Hot isostatic pressing is a manufacturing process in which extreme heat and pressure is used to consolidate and sinter powder or densify existing components by collapsing internal porosity and mitigating lack of fusion defects. Modern HIP machines are able to control cooling rates which allows for a range of in-situ heat treatments varying from furnace cooling to quenching [100]. HIP treatments have been researched extensively and are now the industry standard for removing porosity and other defects in critical components. The basic components of a HIP machine include a pressure vessel, heating elements, water jacket, and a high pressure gas pump. During a HIP cycle, a controller adjusts the temperature and pressure to desired set points for specified lengths of time. The pressure, temperature, and hold time can be varied depending on the material being HIP'd, and the desired results. A diagram of a HIP machine and visual representation of the effects of HIP'ing are shown in Figure 8.

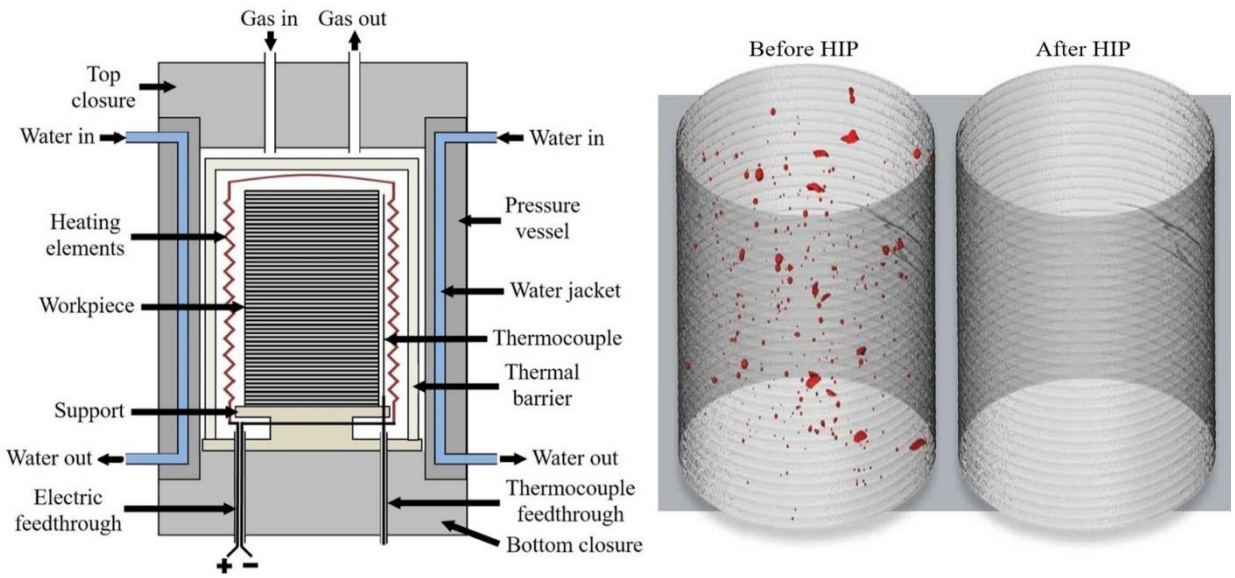

Figure 8: Diagram of HIP machine and visual representation of the effects of HIP [101].

CHAPTER 3:

LASER-DED OF MCrAlY ALLOYS

3.1 Introduction

MCrAlY superalloys with high Al content (> 6%), such as A386, present significant challenges for laser fabrication of bulk structures stemming from the presence of relatively higher amounts of β phase (β = NiAl) than γ/γ′ phase (γ = Ni(Co, Cr) / γ′ = Ni_3Al), which increases an alloys susceptibility to hot cracking during laser-based manufacturing processes [102]. To investigate this challenge, the present study was developed to systematically evaluate the effects of modifying the A386 parent alloy by adding 10, 20, and 30% by weight of a 80%Ni–20%Cr (NiCr) alloy (mainly γ/γ′). While prior studies report laser fabrication of MCrAlY alloys in coating and cladding configurations, bulk structures (thickness > 2 mm) have not been realized. Experimental materials characterization tools are applied to provide insights on phase and microstructural evolution of the NiCoCrAlY alloy as Ni and Cr contents increase. A novel, laser fabricable NiCo-based superalloy chemistry, containing a higher concentration of Al than current "weldable" Ni-based alloys, is reported.

3.2 Materials and Methods

3.2.1 Laser-DED Fabrication

Laser-DED is an AM process which utilizes concentrated laser energy to melt and deposit metallic and/or ceramic powder on a substrate in a layer-wise fashion to form 3D structures. A 3D CAD model was designed and subsequently "sliced" into individual horizontal layers using a proprietary "slicing" software from Optomec Inc. Each slice represents a 2D toolpath which the CNC controller interprets to fabricate the selected layer. Powdered feedstock material is fluidized by the argon carrier gas and blown through nozzles directly into the laser melt pool. The laser

rapidly melts the incoming powder and a deposit is formed upon solidification. As the toolpath follows the deconstructed 3D model, repeated raster scanning, and layer-wise incremental movements in the positive Z direction, a complete 3D component is formed.

To test the laser-DED fabricability of MCrAlY alloys with high aluminum content, a commercially available NiCoCrAlY coating alloy (tradename "Amdry 386" (A386)), was deposited on a SS 304 baseplate. This test was unsuccessful due to severe hot cracking during deposition. A design of experiment (DOE) was constructed where process parameters such as laser power density (laser power & spot size), laser scan speed, hatch spacing, and layer thickness, were varied. The results of this DOE were inconclusive due to all samples cracking severely regardless of the processing parameters. It was concluded that bulk structures of A386 were not fabricable using laser-DED. Initial analysis of these samples showed a relatively large amount of the brittle NiAl phase which was thought to be the main cause of cracking.

Individual A386 alloy and NiCr alloy powders (Oerlicon Metco – MI, USA), with particle size in the range of 45-125 μm (0.00177 – 0.00492 in) were pre-mixed via manual hand mixing and used as the feedstock material in this study. Table 1 shows the weight proportions of the constituent alloying elements for A386, NiCr, and the compositions of the alloys modified with the addition of 10%, 20% and 30% NiCr. The A386 + NiCr alloy coupons were fabricated using a Laser Engineered Net Shaping (LENS™) print engine (Optomec Inc. – NM, USA) equipped with a YLS 1000 W 1070 nm laser (IPG Photonics – MA, USA) within a glove box containing an argon environment. During fabrication, the moisture and oxygen levels were continuously monitored and maintained below 10 ppm. The powder mixtures were processed at 500 W laser power with a 900 μm diameter laser spot size, resulting in a power density of approximately 800 MW/m^2. A cuboidal geometry was selected with a square cross section, 25 mm × 25 mm, that was

built to a height of 6 mm for all the coupons. The deposition speed used was 20 mm/s along with hatch spacing and layer thickness of 0.5 mm. These coupons were deposited on a 6 mm thick stainless steel 304 (SS 304) substrate.

Table 1: Compositions of the A386 and NiCr parent alloy powders as obtained from the powder supplier and their mixtures.

Coupons (wt%)	Weight percentage of constituent elements									
	Ni	Co	Cr	Fe	Si	Mn	Al	C	Hf	Y
100% A386	45.8	22.8	17.3	-	0.46	-	12.4	0.02	0.28	0.61
*Ni-20%Cr	79.3	-	19.4	0.11	0.76	0.39	-	-	-	-
A386 + 10% NiCr	49.1	20.6	17.5	0.01	0.49	0.04	11.2	0.02	0.25	0.55
A386 + 20% NiCr	52.5	18.3	17.7	0.02	0.52	0.08	9.94	0.02	0.22	0.49
A386 + 30% NiCr	55.8	16.0	17.9	0.03	0.55	0.12	8.70	0.01	0.20	0.43

3.2.2 Characterization and Structural Integrity Assessment

Individual laser-DED fabricated coupons were cut from the SS 304 substrate and sectioned with an abrasive cutoff saw (Presi Mecatome T260 – Eybens, FRANCE). One sample was harvested from each coupon in the build direction for microstructural analysis. Each sample was mounted in a thermosetting polymer mounting compound and wet ground from 60 to 1200 grit. The coupons were polished using a 0.06 μm colloidal silica solution until all scratches were removed. After polishing, the coupons were cleaned in a 100% ethanol ultrasonic bath (SharperTEK XP PRO – MI, USA).

The laser-DED processed coupons were characterized to assess the structural integrity, microstructural features and phase evolution using optical microscopy, scanning electron microscopy (SEM), energy dispersive spectroscopy (SEM-EDS), X-ray diffraction (XRD), and microhardness. SEM imaging was performed on a field emission scanning electron microscope operating at 15 kV (JEOL 6610LV – Tokyo, JAPAN). The chemical analysis was conducted using an Energy Dispersive Spectroscopy (EDS) detector (Oxford Instruments X-Max detector –

Abingdon, UK). Optical microscopy was performed using a Keyence microscope and Keyence analysis software (Keyence VHX S650E – Osaka, Japan) to achieve a composite image with high magnification (1000X) and large field-of-view (3 mm × 3 mm). Phase analysis was conducted using Rigaku Smartlab System (Tokyo, JAPAN) with Cu Kβ filter at 40 kV for 2θ from 20° to 100° with a 0.05° step size. The surface roughness of the samples and all other XRD analysis parameters were kept constant in between different samples to allow for comparison of the XRD data. A Vickers microhardness tester (Phase II – NJ, USA) was used to measure the hardness of each coupon. Hardness tests were performed with a constant load of 100 g (0.220 lb) and a 15 s dwell time.

3.3 Results and Discussion

3.3.1 Structural Integrity of Laser-DED Fabricated Coupons

Figure 9 shows that all bulk coupons fabricated by laser-DED are of the desired dimensions of 25 mm × 25 mm × 6 mm, and deposited on the SS 304 substrate. The sample comprised of 100% A386 showed severe cracking and delamination during deposition.

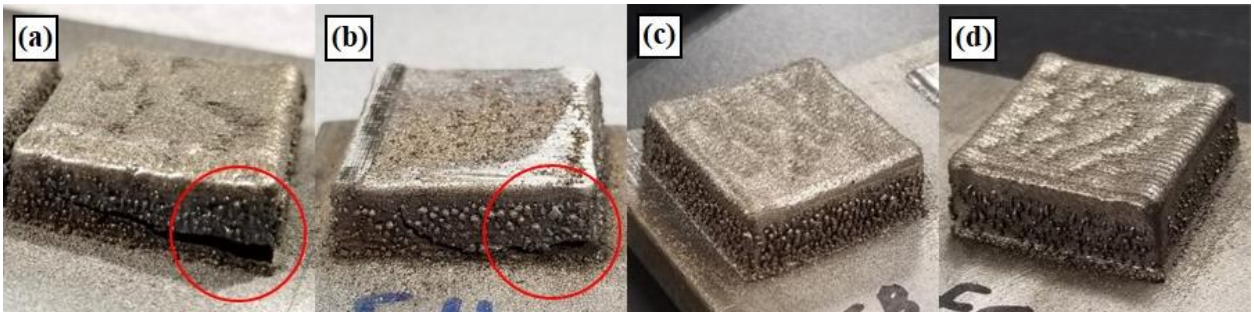

Figure 9: Four different A386 + NiCr mixtures fabricated using laser DED technique for (a) A386, (b) A386 + 10% NiCr, (c) A386 + 20% NiCr, (d) A386 + 30% NiCr. Circled areas show the presence of defects in (a) and (b), and the absence of visible defects in (c) and (d). All coupons measure 25 mm × 25 mm × 6 mm, approximately.

A DOE was constructed, and even with modifications to the process parameters, such as laser power (varied between 400-700 W), deposition speed (varied between 17-25 mm/s), and the CAD

deconstruction parameters such as hatch spacing and layer thickness (both varied between 0.3 - 0.5 mm), it was not possible to fabricate a structurally sound coupon from the 100% A386 alloy powder. These DOE parameter ranges were chosen based on those used in successful L-DED fabrication of other Ni-based superalloys such as Haynes 214 and Inconel 718 in similar works performed by the author. As NiCr was added to A386 in increasing amounts, the cracking and delamination was reduced and the coupons showed improved structural integrity. The red circles in Figures 9(a) and (b) highlight the visible zones of defects such as hot cracking and delamination that occurred during fabrication. Even with the reduced tendency to delaminate and crack with the addition of 10% NiCr, these coupons cracked and failed during sectioning. Small sections or pieces from 100% A386 and A386 + 10% NiCr alloy mixtures were used for microstructural and phase analysis, but owing to their poor structural integrity, A386 and the A386 + 10% NiCr mixture are inferred to be less suitable for fabrication via laser-DED processing. The laser-DED fabrication of the mixtures with higher NiCr content such as A386 + 20% NiCr and A386 + 30% NiCr, were more successful. Upon visual inspection, these coupons (Figures 9(c) and (d)) showed no external cracks or delamination. The coupons were structurally sound and did not fracture during sectioning, grinding, or polishing. A386 + 20% NiCr revealed internal cracking similar to the A386 and A386 + 10% NiCr samples when imaged using optical microscopy (Figure 10(c)).

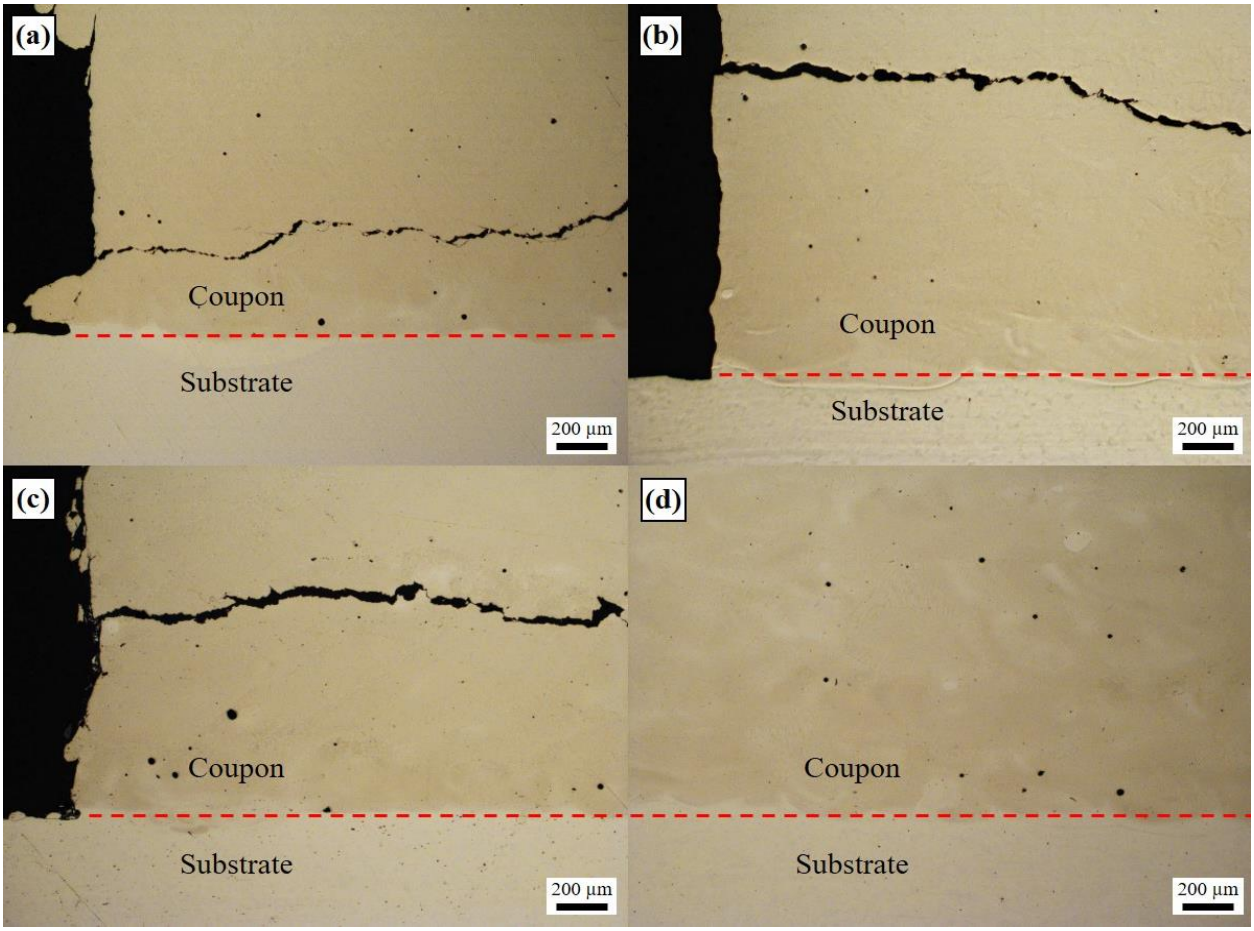

Figure 10: Optical images of mixture samples' crossections showing cracks and porosity (a) A386, (b) A386 + 10% NiCr, (c) A386 + 20% NiCr, and (d) A386 + 30% NiCr.

The lack of severe defects in the A386 + 20% NiCr and A386 + 30% NiCr coupons can be attributed to the increase in γ/γ' as NiCr additions increased. Although the predominant phase transitions from β to γ/γ' between the A386 and A386 + 10% NiCr mixtures, its stabilizing effects are not observed until the NiCr addition reaches 20%. Since the A386 + 30% NiCr coupon was free of structural defects, it was deemed a good choice for bulk, freeform depositions using direct laser fabrication. It may be possible that mixture compositions between 20% and 30% of NiCr in A386 also lead to defect-free fabrication. However, due to the limited supply of specialty alloy powders, these intermediate compositions were not evaluated. A porosity and phase area analysis was performed using optical micrographs and Keyence analysis software (shown in Figure 11),

which found the planar porosity to be less than 0.1%. These results demonstrate the substantial influence of the alloy composition on the structural integrity of laser-DED manufactured coupons. Amongst the tested mixtures, the composition of A386 + 30% NiCr addition resulted in the most successful as-fabricated coupons that were devoid of bulk cracking and interfacial delamination.

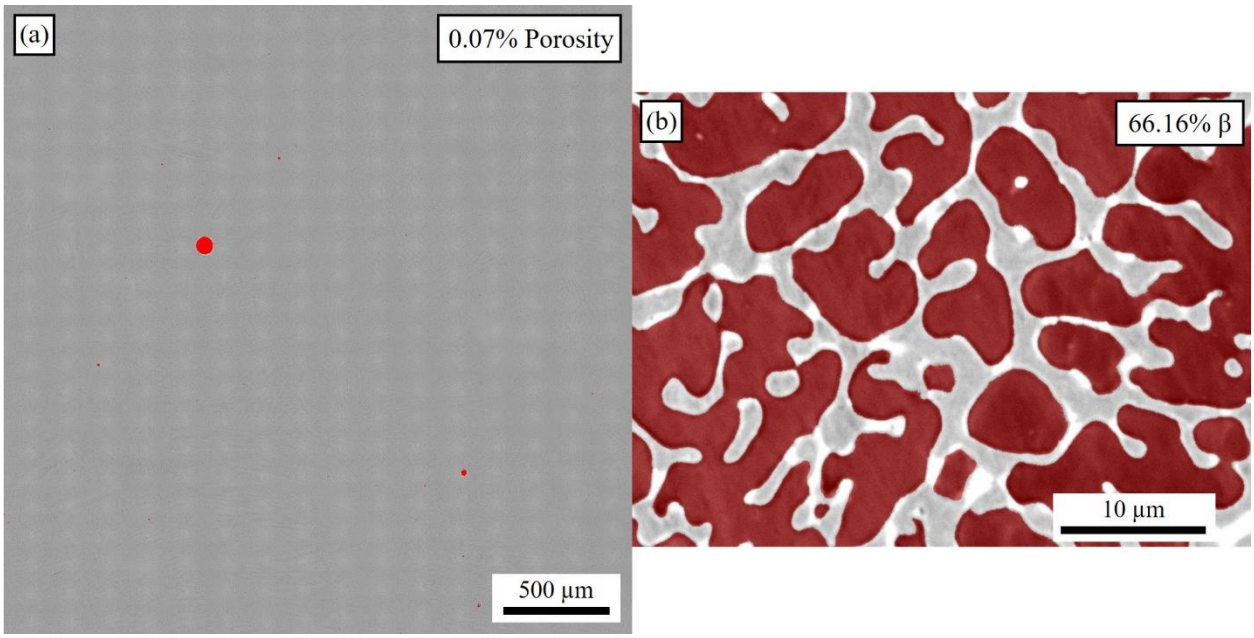

Figure 11: Stitched Keyence micrograph and thresholded % phase area image (a) large field of view (3 mm × 3 mm) and high resolution stitched micrograph of as-processed A386 at 1000X showing amount of porosity, (b) thresholded backscatter electron image of as-processed A386 at 5000X showing amount of β phase compared to γ/γ' phase.

3.3.2 Hot cracking

Hot cracking in Ni-based superalloys has become a complex challenge for manufacturers to overcome. Hot cracking typically occurs in hot manufacturing processes such as welding, casting, forging, and laser or electron beam additive manufacturing techniques in which the manufacturing process temperature is above the workpiece alloys solidus temperature. Hot cracking can be broken down into two different types of cracking, solidification cracking, and liquation cracking. Solidification cracking occurs when the amount of liquid remaining in a melt pool is insufficient to fill gaps between dendrites as they grow during solidification [103]. These

gaps between dendrites act as crack nucleation points which coalesce to form solidification cracks when the solidifying material is unable to accommodate the strain from thermal shrinkage. Liquation cracking refers to cracking caused by the partial melting of previously deposited material during hot manufacturing processes [104]. When partial melting occurs, low melting point eutectic phases (Ni_5Y for this alloy) liquefy and form an intergranular film which allows liquation cracks to form and propagate intergranularly [105-106]. These films reduce microstructural stability and initiate liquation cracks when subjected to sufficient thermal stresses [107].

Hot cracking is common during DED fabrication of "unweldable" Ni-based superalloys which contain more than 6% of Al [108-111]. Figure 12(a) shows transgranular cracking evident by the bright contrast streaks which are fractured crossections of Y-rich phases present at the grain boundaries. Figure 12(b) shows gaps between partially formed dendrites caused by an insufficient amount of liquid metal present in the semi-solid microstructure during the latter stages of solidification. Hot cracking in the laser processed A386 + NiCr coupons was identified as solidification cracking from the fracture surfaces, and the processing parameter DOE results conclude that cracking in the laser-DED samples is not due to suboptimal processing parameters and cannot be avoided for the A386 and A386 + 10% NiCr alloys.

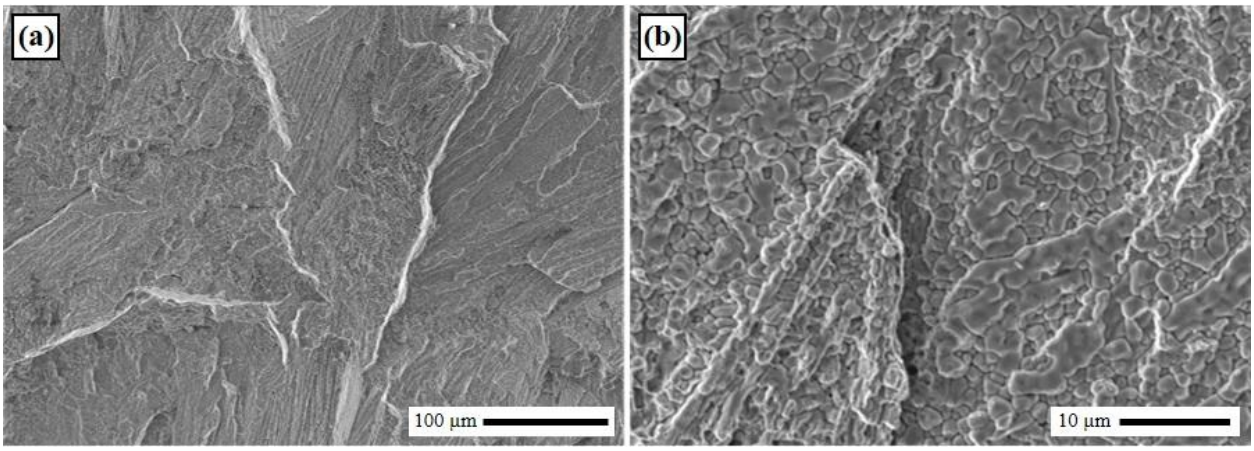

Figure 12: Fracture surface of hot crack in A386 + 10% NiCr (a) transgranular fracture, (b) partially formed dendrites with open spaces in-between.

3.3.3 Phase Analysis

3.3.3.1 SEM Backscatter

In the NiCoCrAl alloy system, γ/γ’ and β are the two prevailing phases [112-113]. The reported microstructures of the A386 + NiCr mixtures are similar to other laser processed NiCoCrAlY microstructures [114, 115]. The SEM backscatter images in Figure 13 reveal the microstructure of the A386 + NiCr mixtures consisting of the light contrast γ/γ’ phase and the dark contrast β phase. From these four micrographs, it is clear that the relative proportion of β is reduced as more NiCr is added to the Amdry 386 composition. The microstructure of laser processed coupons with lesser NiCr additions has a matrix of β phase with sparse, interconnected γ/γ’ phases shown in Figures 13(a - c). As the NiCr content increases, the γ/γ’ phases are stabilized and form coarse dendritic features seen in Figure 13(d).

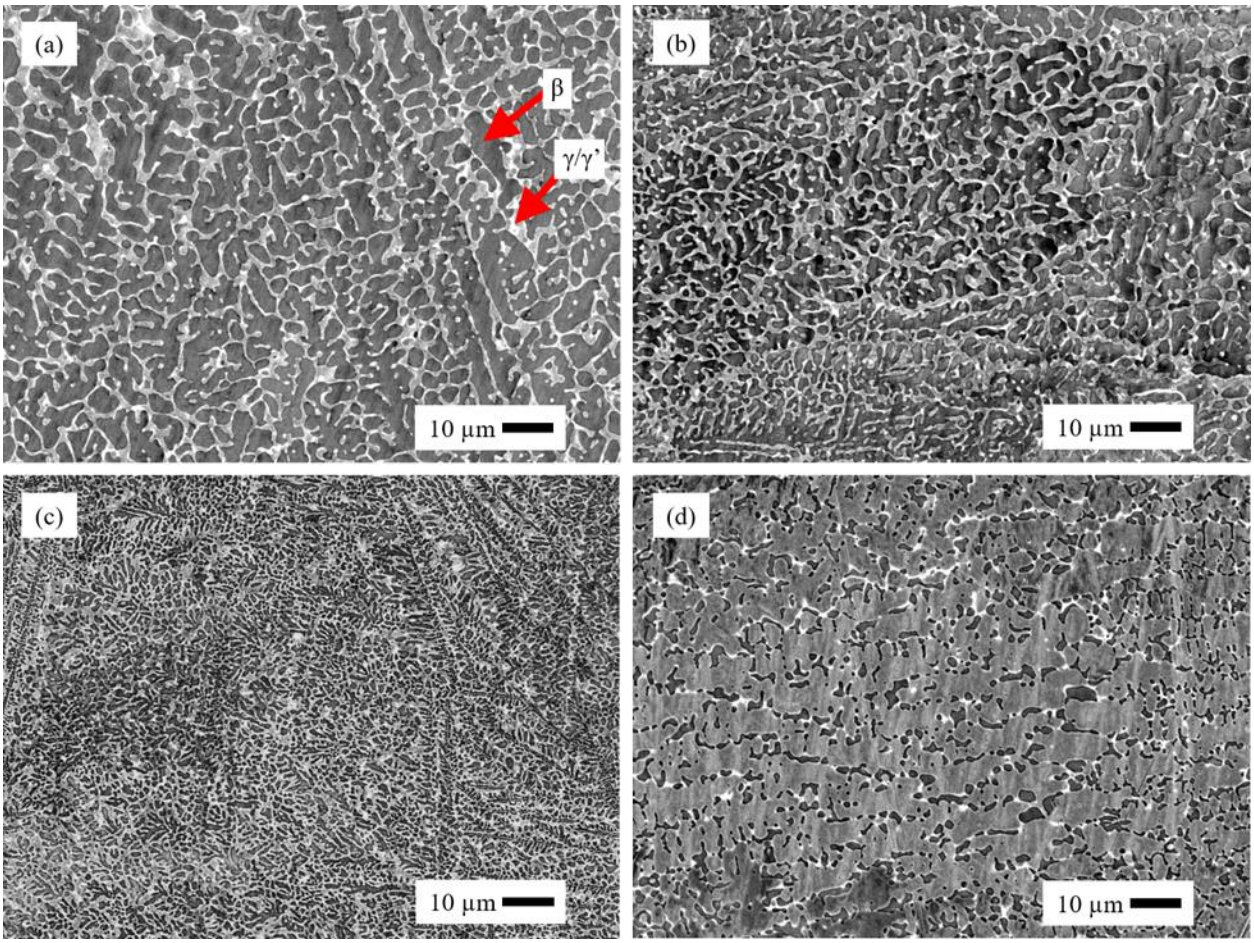

Figure 13: SEM backscatter microstructures of DED fabricated A386 + NiCr mixtures: (a) 100% A386, (b) A386 + 10% NiCr, (c) A386 + 20% NiCr, (d) A386 + 30% NiCr.

The results of the phase area analysis are shown in Figure 14. It can be seen that the β phase area percentage is reduced for each increasing NiCr addition. The 30% NiCr addition is shown to reduce the amount of β phase by about 45% compared to the A386 parent alloy.

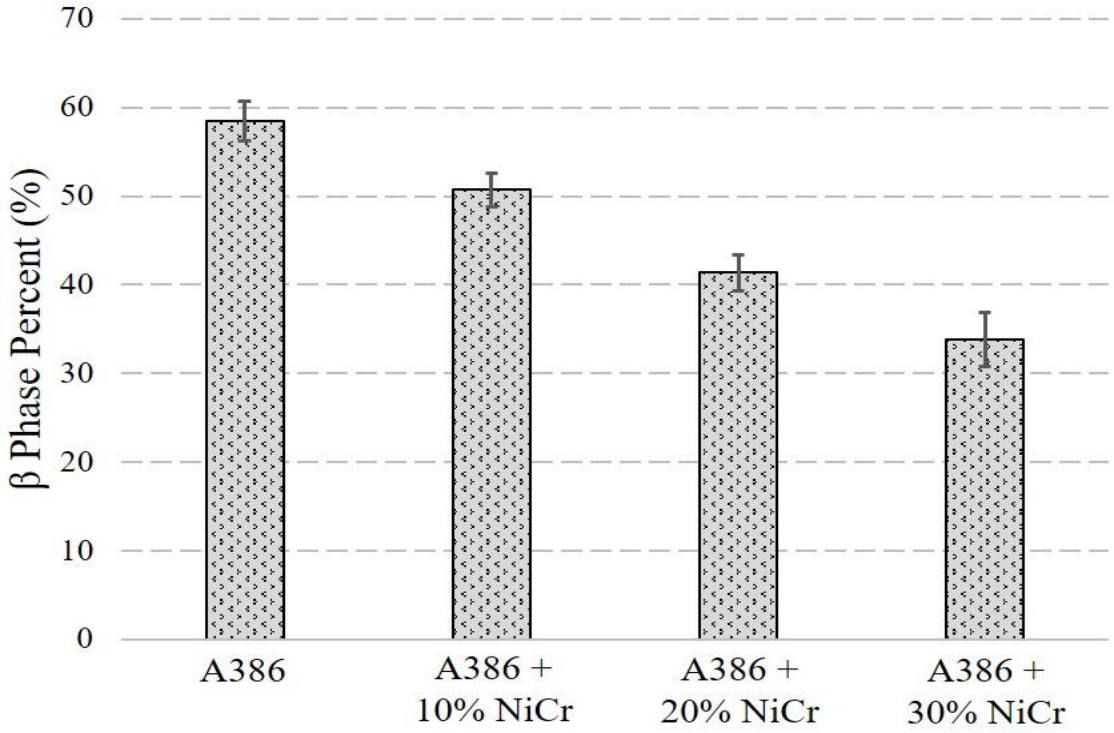

Figure 14: Percent area of β phase of AP coupons.

3.3.3.2 X-Ray Diffraction

XRD was used to understand the nature of these contrasting phases and relate them with the changes in the structural integrity of the material. An XRD comparison in Figure 15 shows XRD patterns of (a) A386 powder, (b) NiCr powder, and all four DED processed A386 + NiCr mixtures (c-f). The NiCr alloy powder contains only γ/γ’ phases, whereas the feedstock A386 powder is rich in β phases with lesser amounts of γ/γ’. After laser-DED fabrication, these β and γ/γ’ phases are retained in each A386 + NiCr mixture sample as shown in Figure 15(c-f).

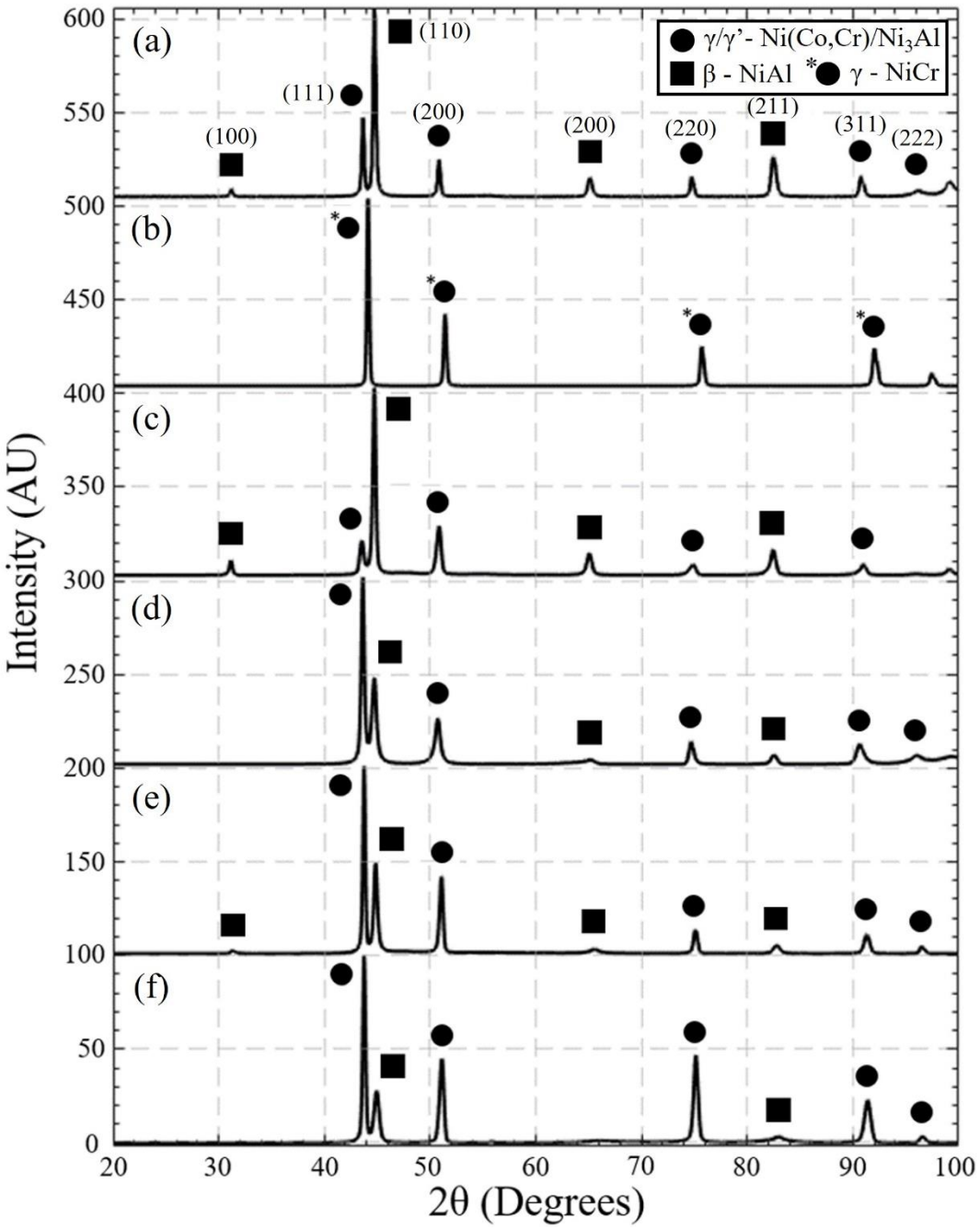

Figure 15: XRD patterns of parent alloy powders and laser-DED processed mixture coupons (a) A386 powder, (b) NiCr powder, (c) A386, (d) A386 + 10% NiCr, (e) A386 + 20% NiCr, (f) A386 + 30% NiCr.

Previous studies have identified a small amount of the Ni_5Y phase present in NiCoCrAlY microstructures [116]. The low amount of this phase is anticipated to produce low-intensity XRD peaks. However, all Ni_5Y XRD peaks coincide with high-intensity peaks from either of the two

dominant phases, which makes the peaks indistinguishable. Therefore, the presence of Ni_5Y even when theoretically established cannot be directly verified using XRD measurements alone. The A386 alloy contained a relative β phase area of 58.48 ± 2.25%, and its proportion reduced to 33.8 ± 3.02% in the A386 + 30% NiCr due to the concurrent rise in γ/γ′. Compared to the base A386 alloy, which is chemically 45.8% Ni, 22.8% Co, 17.3% Cr, and 12.4% Al, the addition of 30% NiCr alloy to A386 causes the wt% of Ni and Cr to increase to 55.8% and 17.9%, respectively, whereas the Al and Co were reduced to 8.69% and 16.0%, respectively (Table 1). Therefore, as the NiCr addition exceeds 10%, the fraction of γ/γ′ begins to dominate the microstructure and an increase in structural integrity is observed.

3.3.3.3 SEM-EDS

The phase transformation and subsequent improvement in the structural integrity of A386 + NiCr alloys are also supported by SEM–EDS analysis. In the 100% A386 mixture, major elements such as Ni, Co, and Cr are evenly distributed whereas Al is segregated at the microscopic scale, with stronger signal of Al corresponding to the darker β phase (Figure 16).

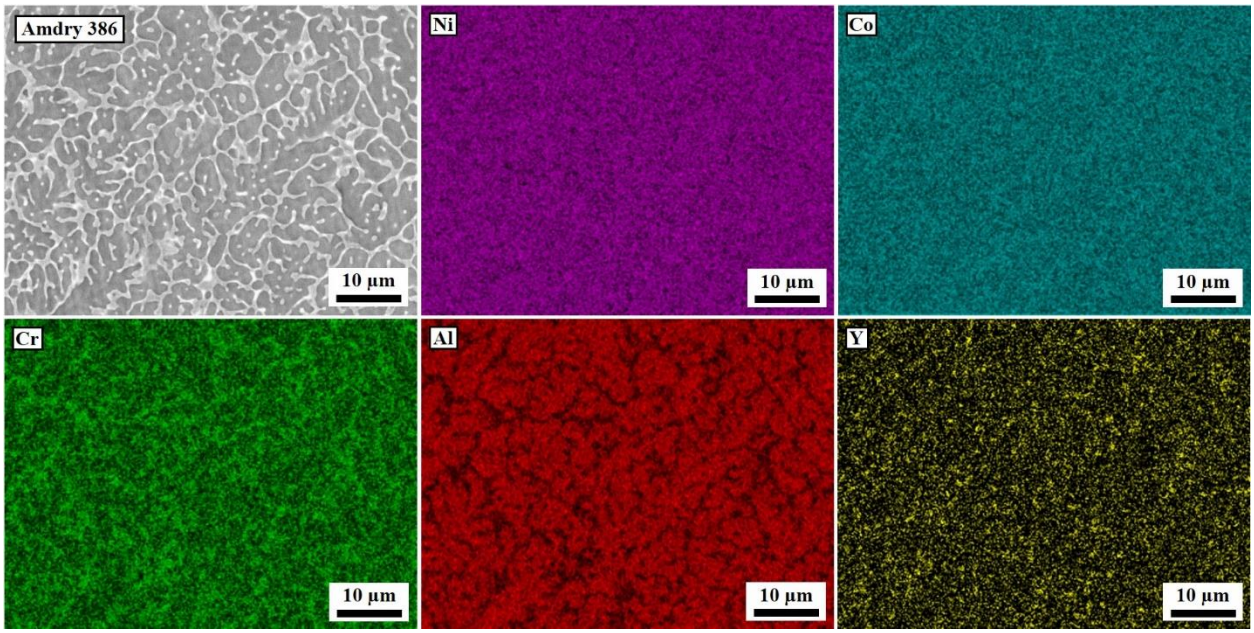

Figure 16: SEM-EDS maps of laser-DED fabricated A386 coupon.

Similarly, in the A386 + 30% NiCr coupon, Al is richer in the darker β phase regions (Figure 17). However, in the A386 + 30% NiCr alloy, these β phase regions are significantly less than that of 100% A386. The EDS maps in Figures 16 and 17 of the A386 and A386 + 30% NiCr mixture compositions show the segregation of yttrium, which coincides with the brightest spots in the microstructure.

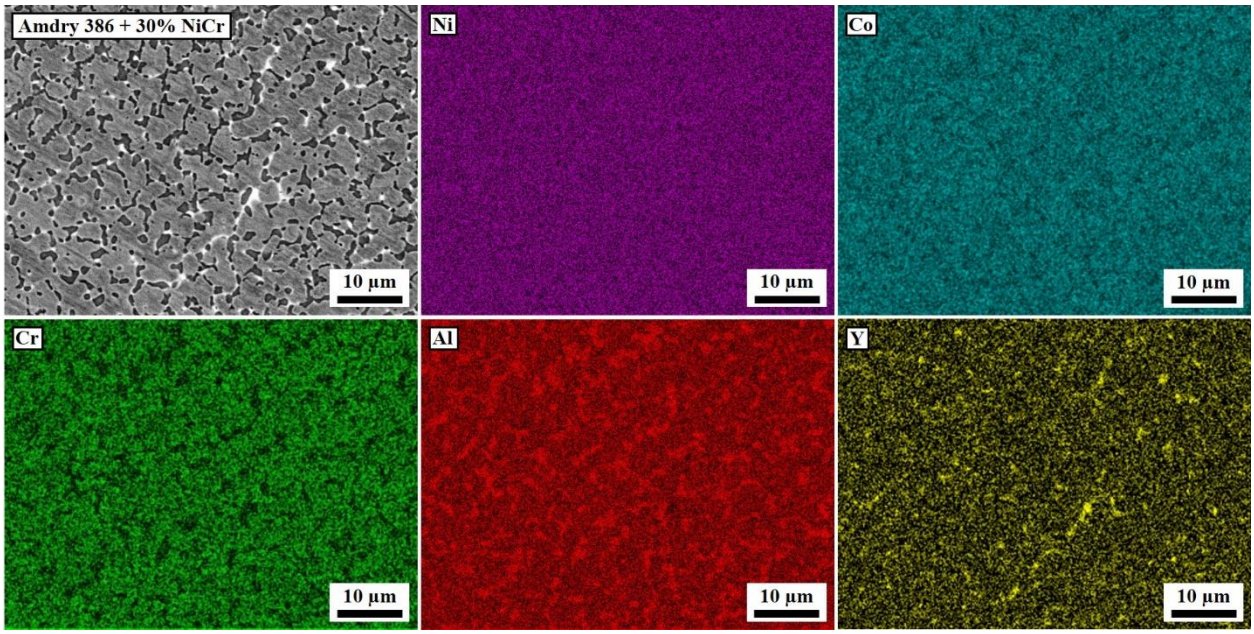

Figure 17: SEM-EDS maps of laser-DED fabricated A386 + 30% NiCr mixture coupon.

3.4 Mechanical Behavior, Scalability, and Material Comparison

Microhardness measurements obtained from the center of each coupon are shown in Table 2. The hardness of the 100% A386 coupon is the highest at 606 ± 13.6 HV. After the additions of 10% and 20% NiCr alloy, the hardness reduces to 547 ± 13.6 HV and 475 ± 15.8, respectively, and continues decreasing to 412 ± 19.1 HV with the 30% NiCr addition. This gradual reduction in the hardness can be attributed to the reduction of β phase.

Table 2: Vicker's micro-hardness of the laser-DED processed A386 + NiCr mixture coupons.

Material	A386	A386 + 10% NiCr	A386 + 20% NiCr	A386 + 30% NiCr
Average Hardness (Vicker's)	606 ± 13.6	546.8 ± 13.6	475 ± 15.8	411.5 ± 19.1

The feasibility of the novel A386 + 30% NiCr alloy mixture for making practical components without any cracking or delamination failure is further evaluated by depositing two types of geometries. The first geometry is a bar with a build height of 120 mm and a crossectional area of 19 mm × 12.5 mm seen in Figure 18(a). The second geometry is a plate with an area of 125 mm × 75 mm, and thickness of 6 mm shown in Figure 18(b). These geometries are deposited without any interruptions in the DED process and are free of any visible cracks or delamination defects.

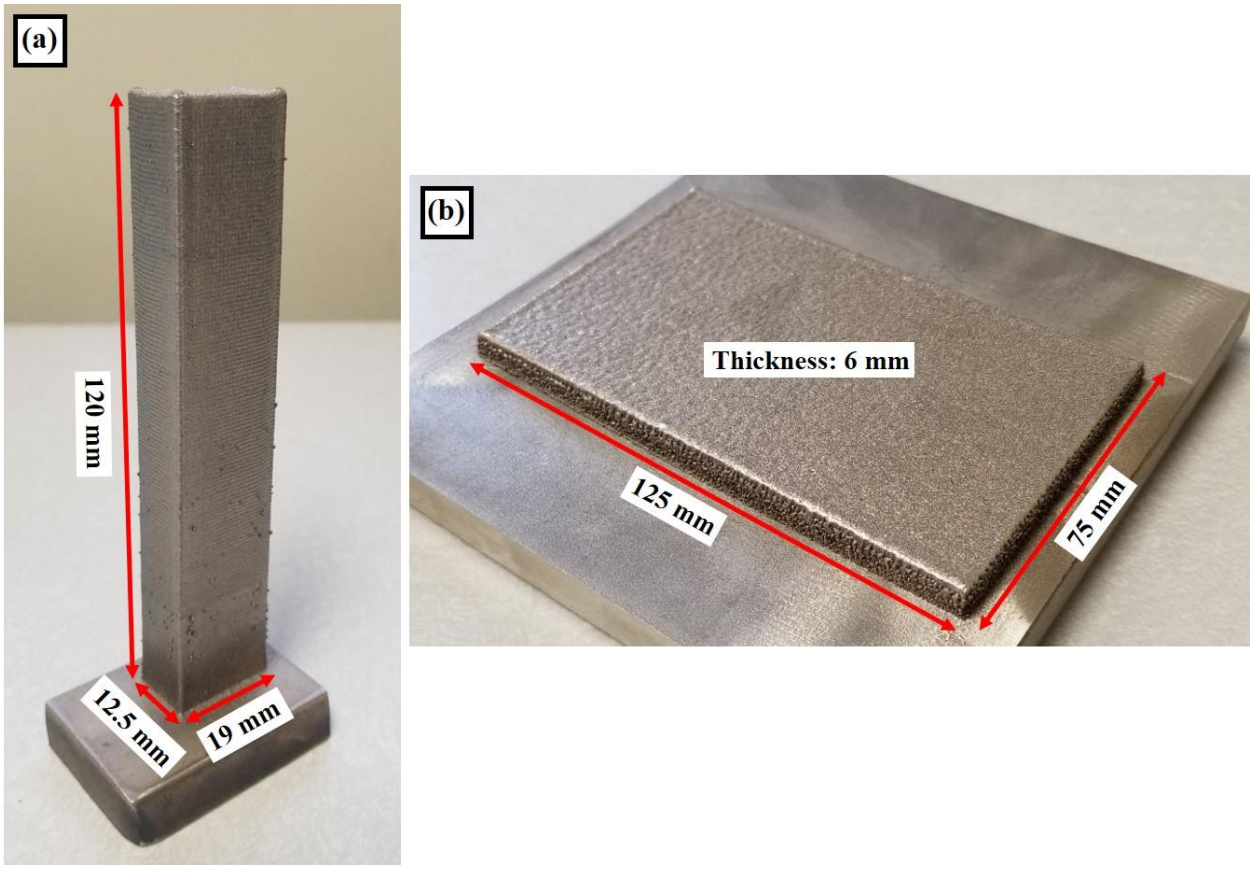

Figure 18: Large near-net shaped components fabricated from the A386 + 30% NiCr alloy mixture using laser-DED (a) bar, and (b) plate.

A386 has a composition similar to other common Ni-based superalloys listed in Table 3. NiCr additions to the A386 parent alloy do reduce the relative amount of Al in the mixture, but even the A386 + 30% NiCr has 1.4 times more Al than the commercially available laser-fabricable alumina forming Ni-based superalloys such as Inconel 713 and René N5 (6–6.2%). Therefore, the alloy composition reported here could be a strong candidate for applications where high temperatures and corrosive environments are present. The ability to fabricate near-net-shaped structures using laser-based AM processes such as laser-DED further enables the deployment of this alloy in novel structures.

Table 3: List of compositions of common laser processable Ni-based hot corrosion resistant superalloys with Al content greater than 4.5%.

Material	Weight Percentage of Constituent Elements												
	Ni	Co	Cr	Mo	Fe	Al	Ti	W	Ta	Nb	Hf	Y	Al/Cr
A386	45.8	22.8	17.3	-	-	12.4	-	-	-	-	0.28	0.61	0.72
NiCr	79.3	-	19.4	-	0.11	-	-	-	-	-	-	-	-
A386 + 10% NiCr	49.2	20.5	17.5	-	0.01	11.2	-	-	-	-	0.25	0.55	0.64
A386 + 20% NiCr	52.5	18.3	17.7	-	0.02	9.90	-	-	-	-	0.22	0.49	0.56
A386 + 30% NiCr	55.9	16.0	17.9	-	0.03	8.69	-	-	-	-	0.20	0.43	0.49
Haynes 214	75.0	-	16.0	-	3.00	4.50	-	-	-	-	-	-	0.28
Inconel 100	61.4	15.0	9.50	3.00	0.50	5.50	4.75	-	-	-	-	-	0.58
Inconel 713	75.5	-	12.0	3.90	0.18	6.00	0.63	-	-	1.80	-	-	0.50
Inconel 738	61.5	8.50	12.0	3.90	0.18	6.00	0.63	-	-	1.80	-	-	0.50
MAR-M 200	60.1	10.0	9.00	-	0.75	5.00	2.00	12.0	-	1.00	-	-	0.56
MAR-M 247	57.5	9.48	9.05	0.78	-	5.52	1.12	11.2	3.78	0.12	1.18	-	0.61
René N5	60.6	8.00	7.00	2.00	-	6.20	1.00	5.00	7.00	0.10	0.10	-	0.89
René 100	61.0	15.0	9.50	3.00	0.50	5.50	4.20	-	-	-	-	-	0.58
René 142	60.8	12.0	6.80	1.50	-	6.15	-	4.90	6.35	-	1.50	-	0.90

3.5 Conclusions

The present work investigates the ability to create bulk samples of the NiCo based, dual phase superalloy A386 using laser-DED. The base alloy chemistries were modified by controlled additions of a NiCr alloy to create mixtures with varying relative amounts of Ni, Co, Cr and Al. The effects of alloy compositions on the fabricability, structural integrity, and hardness were evaluated by experimental materials characterization and testing. The as-received A386 and NiCr feedstock powders were comprised of mostly β with smaller amounts of γ/γ′ phases, and almost completely γ/γ′, respectively. The constituent phases of A386 powder were retained in relatively the same proportions after laser-DED processing. The dominating phase switches from β to γ/γ’ between the A386 and A386 + 10% NiCr mixtures, but the increase in structural integrity is not observed until the NiCr additions reach a minimum of 20%. This microstructural switch from β to

γ/γ′ increases the structural integrity further as the wt% of NiCr approaches 30%. The modified alloy chemistries allowed for the successful fabrication of larger-scale components. Specifically, A386 +30% NiCr is reported to be a viable mixture for direct laser fabrication of near-net shaped components. A plate and a bar geometry were successfully fabricated using laser-DED, with the largest dimensions on the order of tens of centimeters.

CHAPTER 4:

EFFECTS OF HIP'ING: MICROSTRUCTURE AND STRUCTURAL INTEGRITY OF LASER-DED FABRICATED NiCoCrAlY ALLOYS

4.1 Introduction

Beam-based additive manufacturing techniques impart residual stresses within deposited material due to the inherent rapid melting and solidification. Residual stresses and microstructure embrittlement can cause components to crack, or warp during post process machining or upon removal from their substrate. To reduce the tendency of low temperature cracking, the present work was developed to investigate the effects of Hot Isostatic Pressing (HIP) on bulk A386 + NiCr mixture coupons fabricated via laser-DED. HIP treatments have also been shown to heal minor cracks in Ti alloys [117], Fe alloys [118], and NiCr alloys [119-120], but crack healing in high melting point NiCo alloys such as A386 has not yet been studied.

Several HIP trials were investigated to find a set of parameters which reduced porosity, relieved internal stresses, healed cracks, and improved overall structural integrity. HIP parameters which reduced internal porosity, and relieved residual stresses leading to the elimination of cracking and warping during post process machining are reported. Residual stress measurements of the A386 + 20% and 30% NiCr samples in the AP and HIP'd states, tensile strength measurements of A386 + 20% and 30% NiCr samples in the HIP'd state, and evidence of crack healing during HIP are reported.

4.2 Materials and Methods

4.2.1 Laser-DED Fabrication

A386 and NiCr parent alloy powders (Oerlikon Metco – MI, USA) with a particle size range of 45-125 μm were pre-mixed by manual shaking and used as feedstock for DED processing.

The weight proportions of constituent alloy elements for the parent alloys and their three mixtures are listed in Table 1 located in section 3.2 of this document. A386 + NiCr mixture coupons were fabricated using a 3D CNC enabled Laser Engineered Net Shaping (LENS™) print engine (Optomec Inc. – NM, USA) equipped with a YLS 1000 W capacity, 1070 nm wavelength laser (IPG Photonics – MA, USA) contained within an argon environment. Throughout all depositions, the oxygen and moisture levels were monitored and maintained at 10 ppm or less. In this study, three sets of coupons were manufactured by laser-DED to investigate the effects of HIP on the microstructure, defects, mechanical properties, and residual stress of laser-DED fabricated A386 + NiCr mixture coupons.

4.2.1.1 HIP Parameter Testing Coupons

Four coupons, one for each of the A386, A386 + 10% NiCr, A386 + 20% NiCr, and A386 + 30% NiCr mixtures, with crossectional dimensions of 20 mm × 20 mm, and height of 12 mm, were deposited on 6 mm thick stainless steel 304 (SS 304) plate substrates. These coupons were fabricated to test the effect of varying HIP parameters on the laser-DED mixture coupons. The deposition parameters used to deposit these coupons were 500 W laser power, 900 µm diameter spot size (approximate power density = 800 MW/m^2), 0.3 mm hatch spacing and layer thickness, and 20 mm/s laser scan speed. The preliminary coupons are shown in Figure 22.

4.2.1.2 High Temperature Tensile Bar Blanks

A set of six large bar coupons were fabricated to be used as bulk material for producing high temperature tensile bars. Three A386 + 30% NiCr mixture coupons with dimensions of 15 mm × 35 mm × 150 mm tall, and three coupons of A386 + 20% NiCr with dimensions of 15 mm × 35 mm × 180 mm tall were deposited on 12 mm thick stainless steel 304 (SS304) substrates. The A386 + 20% NiCr coupons were built taller than the A386 + 30% NiCr coupons due to cracking

near the substrate (Figure 24). The deposition parameters used to fabricate these coupons were 500 W laser power, 900 µm diameter spot size (approximate power density = 800 MW/m^2), 0.45 mm hatch spacing and layer thickness, and 25 mm/s laser scan speed. These high temperature tensile bar blanks can be seen in Figure 23.

4.2.1.3 Residual Stress Testing Coupons

The third set of coupons was comprised of four cubes, two A386 + 30% NiCr cube coupons with dimensions of 25 mm × 25 mm × 25 mm, and two A386 + 20% NiCr cube coupons with dimensions of 25 mm × 25 mm × 40 mm. The A386 + 20% NiCr coupons are taller than the A386 + 30% NiCr coupons due to cracking near the substrate. The deposition parameters used to deposit these coupons were 500 W laser power, 900 µm diameter spot size (approximate power density = 800 MW/m^2), 0.45 mm hatch spacing and layer thickness, and 22 mm/s laser scan speed. The coupons were deposited on a 12 mm thick stainless steel 304 (SS304) substrate and can be seen in Figure 25.

4.2.2 Hot Isostatic Pressing (HIP)

Common HIP temperatures and pressures used in Ni-based superalloy manufacturing range from 1100 °C – 1300 °C and 100 MPa – 200 MPa respectively [121-126]. The experimental HIP parameters for this study (Table 4) were chosen to be within these ranges. Each preliminary HIP coupon was sectioned into three samples in preparation for the HIP treatments listed in Table 4. Two samples from each preliminary coupon were HIP'd, one sample subjected to HIP1, and the other to HIP2. The third sample from each preliminary coupon was kept in the as processed condition for comparison. The HIP1 and HIP2 treatments were performed in an Eagle HIP machine (American Isostatic Presses – Ohio, USA). All tensile bar blanks and one residual stress coupon from the A386 + 20% NiCr and A386 + 30% NiCr mixtures were subjected to HIP3, which was

performed by Quintus Technologies in a QIH 15L HIP machine (Quintus Technologies – Ohio, USA).

Table 4: Process parameters of the four treatments, as processed, HIP1, HIP2, and HIP3.

Treatment	Heating Rate	Temperature (°C)	Pressure	Hold Time	Cooling Rate
As Processed	> 1000 °C/s	> melting point	2 MPa	None	> 1000 °C/s
HIP1	5 °C/min	1250 °C	200 MPa	4 hr	5 °C/min
HIP2	5 °C/min	1150 °C	200 MPa	4 hr	5 °C/min
HIP3	10 °C/min	1150 °C	200 MPa	4 hr	10 °C/min

4.2.3 Metallurgical Sample Preparation

After deposition, all SS 304 substrates were sectioned to separate the coupons using an abrasive cutoff saw (Presi Mecatome T260 – Eybens, FRANCE). After treatment, all preliminary samples (as processed, HIP1, and HIP2), and witness samples from each tensile bar blank (HIP3) were mounted in a thermoplastic mounting compound and wet ground from 60 to 1200 grit sandpaper and polished using a 0.06 µm colloidal silica solution. After polishing, the mounted samples were thoroughly cleaned in a 100% ethanol ultrasonic bath (SharperTEK XP PRO – MI, USA).

4.2.4 Characterization

Optical imaging of the microstructures was done using a Keyence VHX S650E microscope (Keyence Corporation – Osaka, Japan). Keyence software was used to measure porosity and relative phase area. SEM imaging was performed on a field emission scanning electron microscope operating at 15 kV (JEOL 6610LV – Tokyo, JAPAN). The chemical analysis was conducted using an Energy Dispersive Spectroscopy (EDS) detector (Oxford Instruments X-Max detector – Abingdon, UK) within the aforementioned SEM. TEM samples were made using a Thermo Fisher Helios PFIB UXe microscope. TEM and high resolution EDS was done using a Thermo Fisher Spectra 300 Probe-Corrected S/TEM microscope fitted with a Dual-X window-less detector. Phase

analysis was conducted using a Rigaku Smartlab System (Tokyo, JAPAN) with Cu Kβ filter at 40 kV for 2θ from 20° to 100° with a 0.05° step size. The surface roughness of the samples and all XRD analysis parameters were kept constant between different samples to allow for comparison of the XRD data. Nanoindentation was performed using a TI950 Triboindenter with diamond Berkovich probe operating with an indentation load of 1 N to measure the room temperature elastic modulus needed for residual stress measurements. A Vickers microhardness tester (Phase II – NJ, USA) was used to measure the hardness of each coupon. Hardness tests were performed with a constant load of 100 g and a 15 s dwell time.

4.2.5 Tensile Bar Production and Testing

After HIP3, the tensile bar blanks were machined into tensile bars using wire EDM. Metallographic samples were harvested from the EDM scraps of each tensile bar blank. Each of the tensile bar blanks yielded 13 tensile bars making for a total of 39 bars for each of the A386 + 20% NiCr and A386 + 30% NiCr compositions. About 30% of the tensile bars had visible defects and were scrapped. The high temperature tensile bar dimensions are shown below in Figure 19.

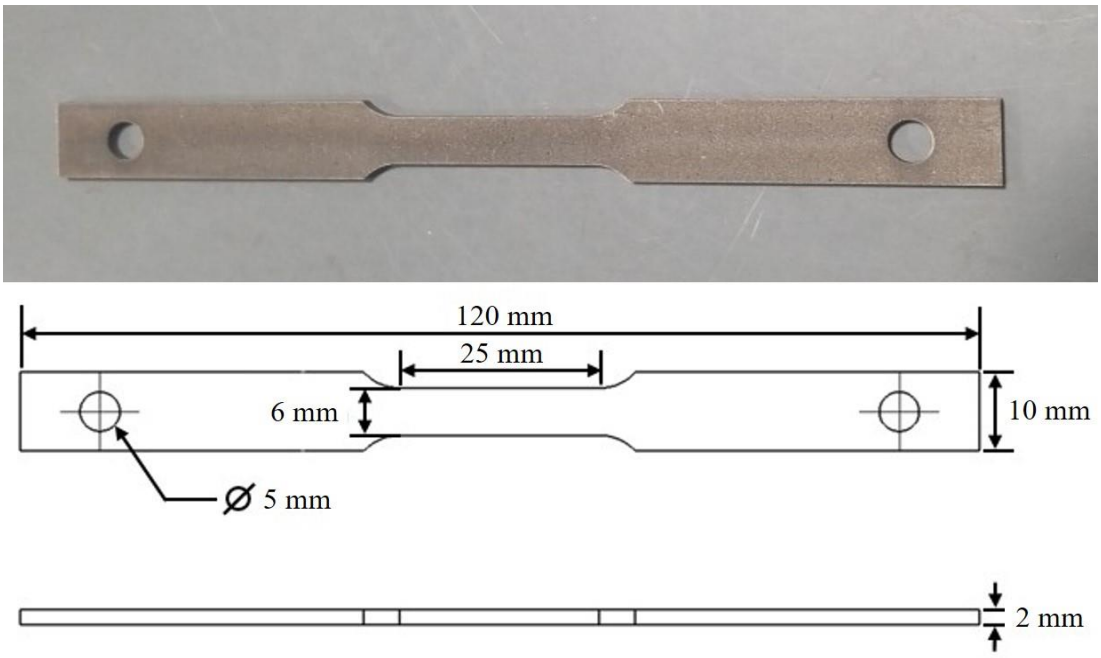

Figure 19: High temperature tensile coupon blank with dimensions.

High temperature tensile testing was conducted using a 300kN Instron MTS electromechanical load frame (MTS Systems – MN, USA), fitted with a custom high temperature furnace (AMTECO Inc – OH, USA), and high temperature extensometer (Epsilon Technology Corp – WY, USA). High temperature tensile tests were conducted at 700, 800, 900, and 1000 °C with a constant strain rate of 0.005/s. Three tensile bars were tested for each composition at each temperature. All components of the high temperature tensile testing apparatus can be seen in Figure 20.

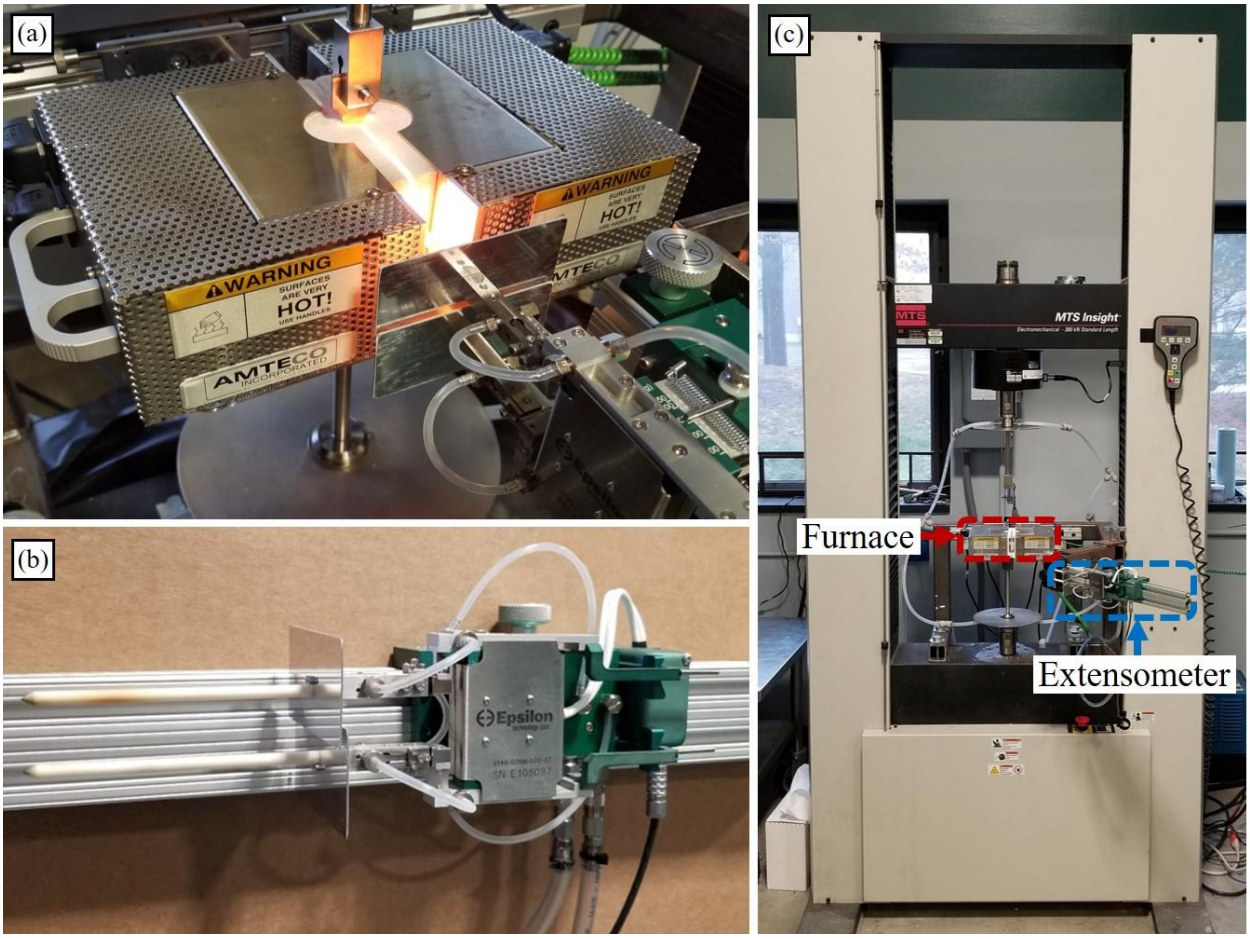

Figure 20: High temperature tensile testing apparatus: (a) high temperature furnace, (b) high temperature extensometer, (c) electromechanical load frame.

4.2.6 Residual Stress Testing

One residual stress coupon from the A386 + 20% NiCr and A386 + 30% NiCr mixtures were subjected to the HIP3 treatment, and the other was left in the AP condition. All four coupons were tested using the Slitting Method to measure their residual stresses. The residual stress testing was conducted using Micro-Measurement CEA-00- 250UW-120 strain gages, a Vishay 7000-32-SM StrainSmart data acquisition system, and a Mitsubishi FA10S wire electrical discharge machining (EDM) machine. The top 3 mm was cut from the residual stress coupons using the EDM machine. Next, a 10 mm thick slice was cut from the cube coupon. A diagram of the residual stress coupon cuts and strain gauge location is shown in Figure 21(a). The 10 mm thick slice was

loaded into the EDM machine on edge with the strain gage facing away from the EDM wire as seen in Figure 21(b). The EDM wire cut the samples forming a slit shown in Figure 21(c). The wire was advanced through the sample in increments of 0.5 mm where strain measurements were recorded.

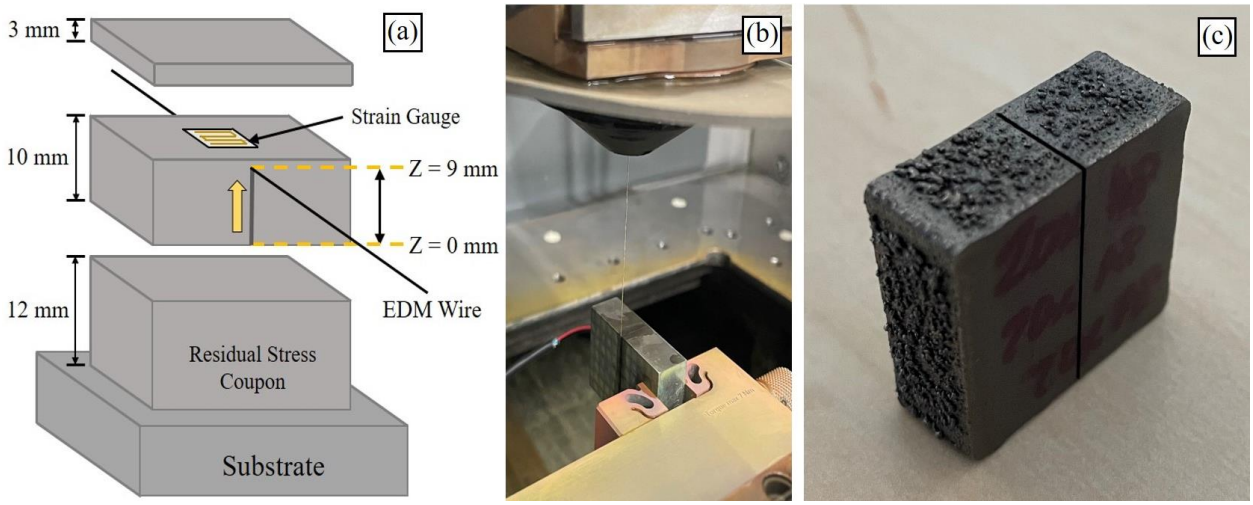

Figure 21: (a) Residual stress coupon cut diagram, (b) Residual stress sample in EDM machine, and (c) coupon after slitting.

4.3 Results & Discussion

4.3.1 Structural Integrity of Laser-DED Coupons

4.3.1.1 HIP Parameter Testing Coupons

Figure 22 shows the four preliminary coupons fabricated for HIP parameter testing. One coupon was fabricated for each of the A386, A386 + 10% NiCr, A386 + 20% NiCr, and A386 + 30% NiCr mixtures. The coupons were deposited on a 6 mm thick stainless steel 304 plate substrate and closely resemble the desired dimensions of 20 mm × 20 mm × 12 mm tall.

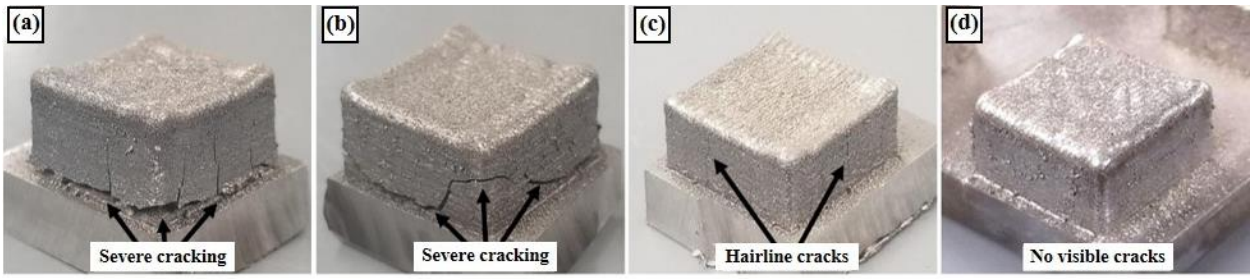

Figure 22: Preliminary HIP parameter test coupons of the mixtures: (a) A386, (b) A386 + 10% NiCr, (c) A386 + 20% NiCr, and (d) A386 + 30% NiCr.

Figures 22(a) and (b) show severe cracking in the A386 and A386 + 10% NiCr coupons which structurally failed during sectioning. Figures 22(c) and (d) show hairline cracks in the A386 + 20% NiCr coupon and no external cracking in the A386 + 30% NiCr coupon respectively. The A386 + 20% and 30% NiCr coupons withstood sectioning without failure.

4.3.1.2 High Temperature Tensile Bar Blanks

Figure 23 shows that all six tensile bar blanks are deposited on the 12 mm thick stainless steel 304 (SS304) substrate, and are of the desired dimensions of 15 mm × 35 mm × 180 mm tall for the A386 + 20% NiCr coupons, and 15 mm × 35 mm × 150 mm tall for the A386 + 30% NiCr coupons.

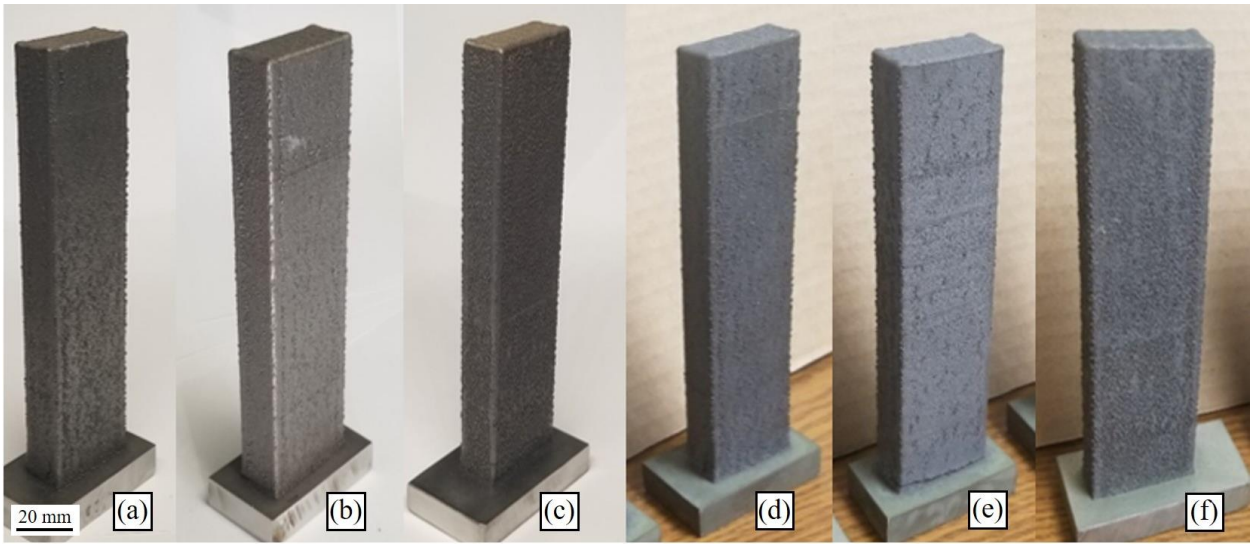

Figure 23: High temperature tensile coupon blanks: (a – c) A386 + 30% NiCr in the as processed state and (d – f) A386 + 20% NiCr after HIP'ing.

The A386 + 20% NiCr coupons (Figures 23(a - c)) are 30 mm taller than the A386 + 30% NiCr coupons (Figures 23(d – f)) to avoid the 25 – 30 mm of cracked material near the substrate seen in Figure 24. This extra height ensured a sufficient amount of defect free material above the cracks to machine high temperature tensile bars from.

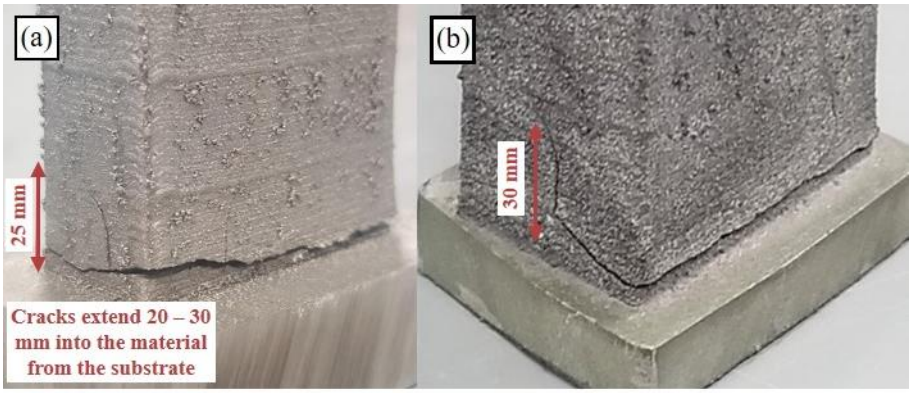

Figure 24: Cracks near substrate on A386 + 20% NiCr high temperature tensile coupon blanks: (a) before HIP, and (b) after HIP.

4.3.1.3 Residual Stress Testing Coupons

Figure 25 shows the residual stress coupons which are of the desired dimensions, 25 mm × 25 mm × 25 mm tall for A386 + 30% NiCr coupons, 25 mm × 25 mm × 40 mm tall for the A386 + 20% NiCr coupons. All residual stress coupons were bonded to the 12 mm thick stainless steel 304 (SS304) substrate. The A386 + 20% NiCr coupons are taller than the A386 + 30% NiCr coupons due to cracking near the substrate. As with the A386 + 20% NiCr tensile bar blanks, the A386 + 20% NiCr residual stress coupons have cracks near the substrate which extend 25 – 30 mm up into the sample.

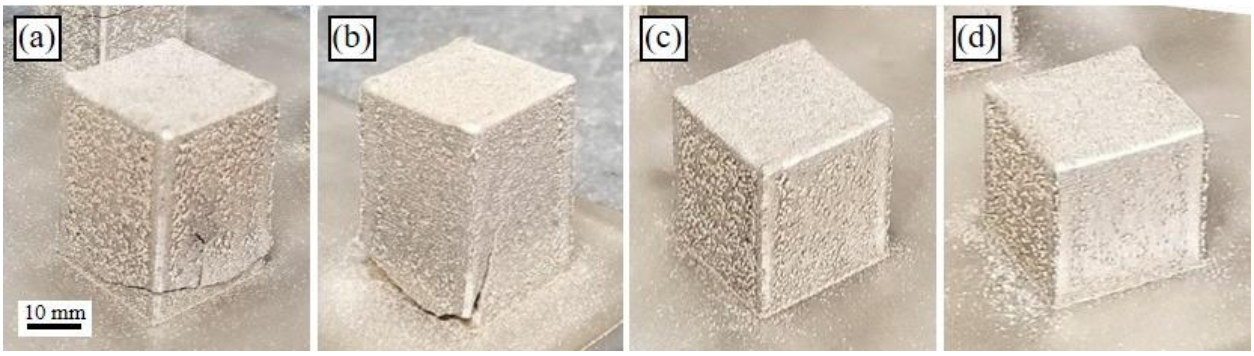

Figure 25: Residual stress testing coupons before HIP3: (a - b) A386 + 20%, and (c - d) A386 + 30% NiCr.

4.3.2 Porosity Analysis

Figure 26 is a visual representation of the reduction in porosity caused by the three HIP treatments. The optical micrographs of the AP samples in this figure show the presence of small pores in the 5 – 10 µm size range while the HIP'd micrographs show little to no porosity.

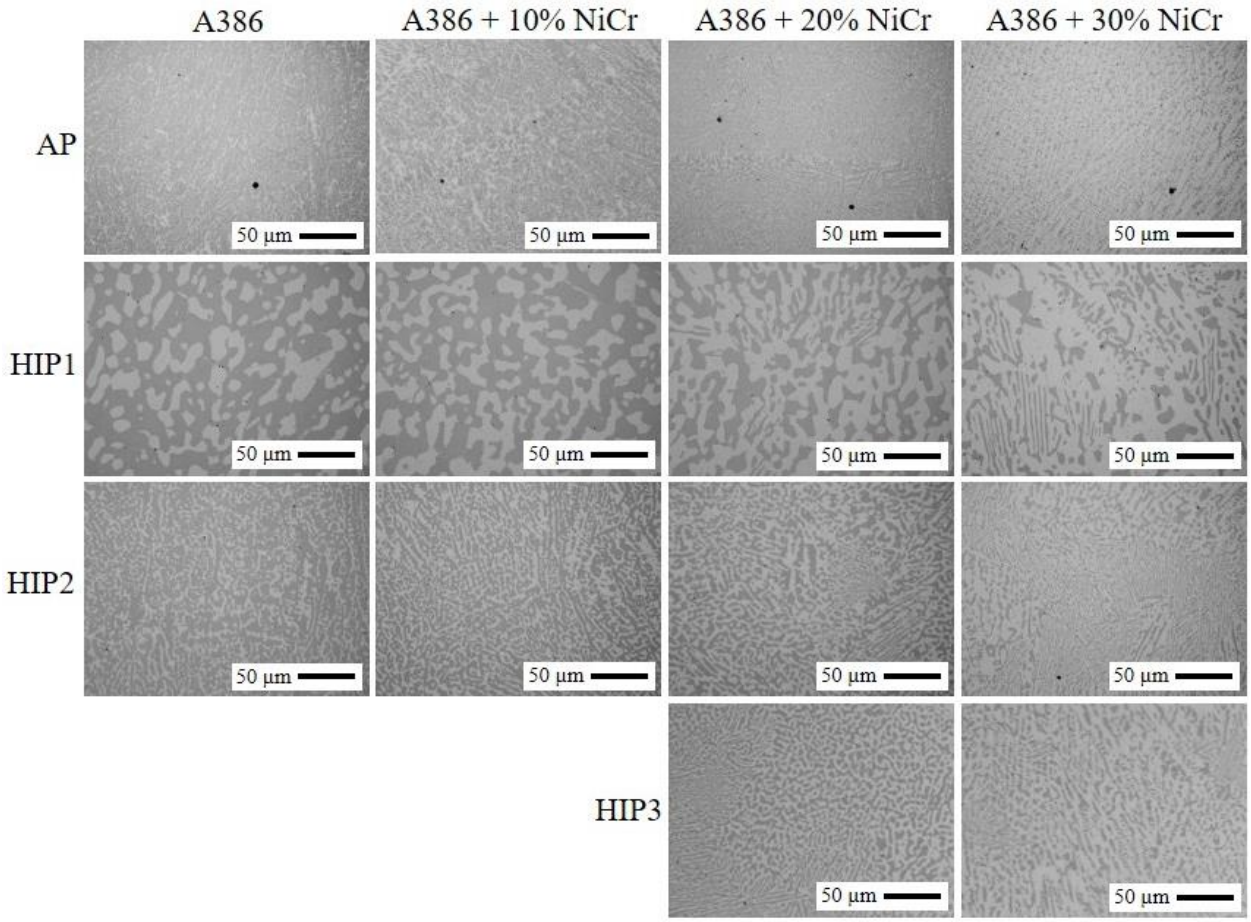

Figure 26: Optical microstructures images of DED fabricated A386 + NiCr mixtures in the AP and HIP'd states.

Figure 27 shows the average porosity area percentage values for each mixture and treatment combination. The HIP1 parameters were the most effective in removing porosity, but each of the three HIP processes produced near full density samples with average porosity values being less than 0.0085%.

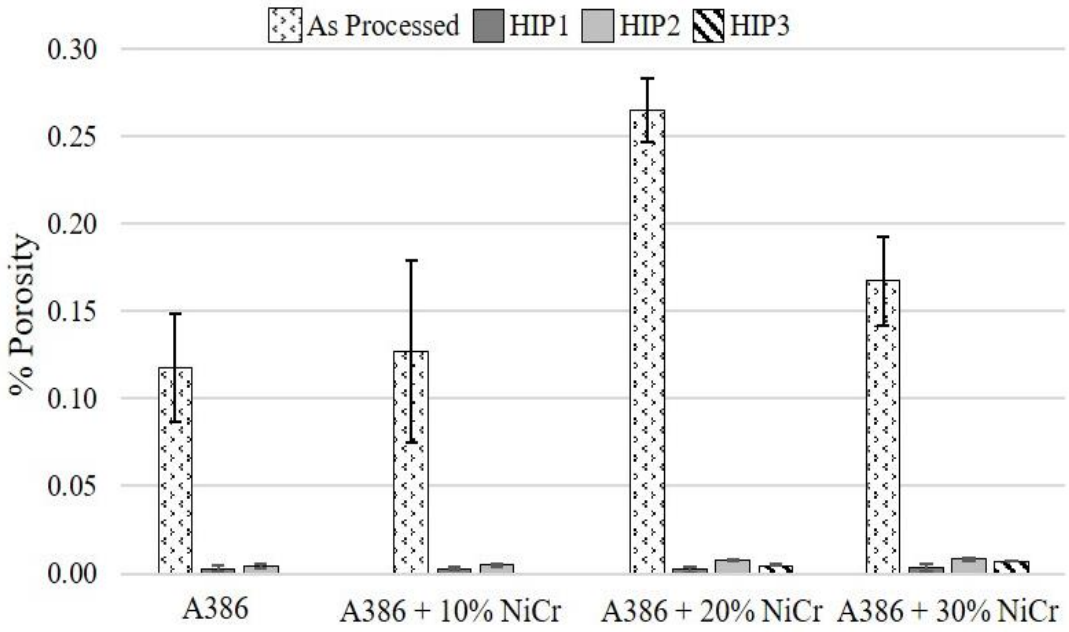

Figure 27: Average porosity % area of A386 + NiCr mixture coupons in AP and HIP'd states.

4.3.3 Phase Analysis

Figure 28 shows SEM micrographs of all AP and HIP'd sample microstructures. The AP microstructures exhibit a fine interdendritic microstructure common to laser processed superalloys [52-55]. Grain growth occurred in each mixture coupon for all three HIP treatments, with lesser grain growth observed in the lower temperature (1150 °C) HIP2 and HIP3 treatments. The highest amount of grain growth was observed in the coupons subjected to the hottest (1250 °C) treatment, HIP1. The Yttrium rich phases in the AP samples were randomly shaped and well disbursed. The HIP1 treatment caused the yttrium rich phase to segregate from the matrix and form into large, well defined agglomerations in the grain boundaries. In the HIP2 and HIP3 states, the yttrium phases also migrated to the grain boundaries, but are shown to agglomerate into small round particles with an average diameter of approximately 2 μm.

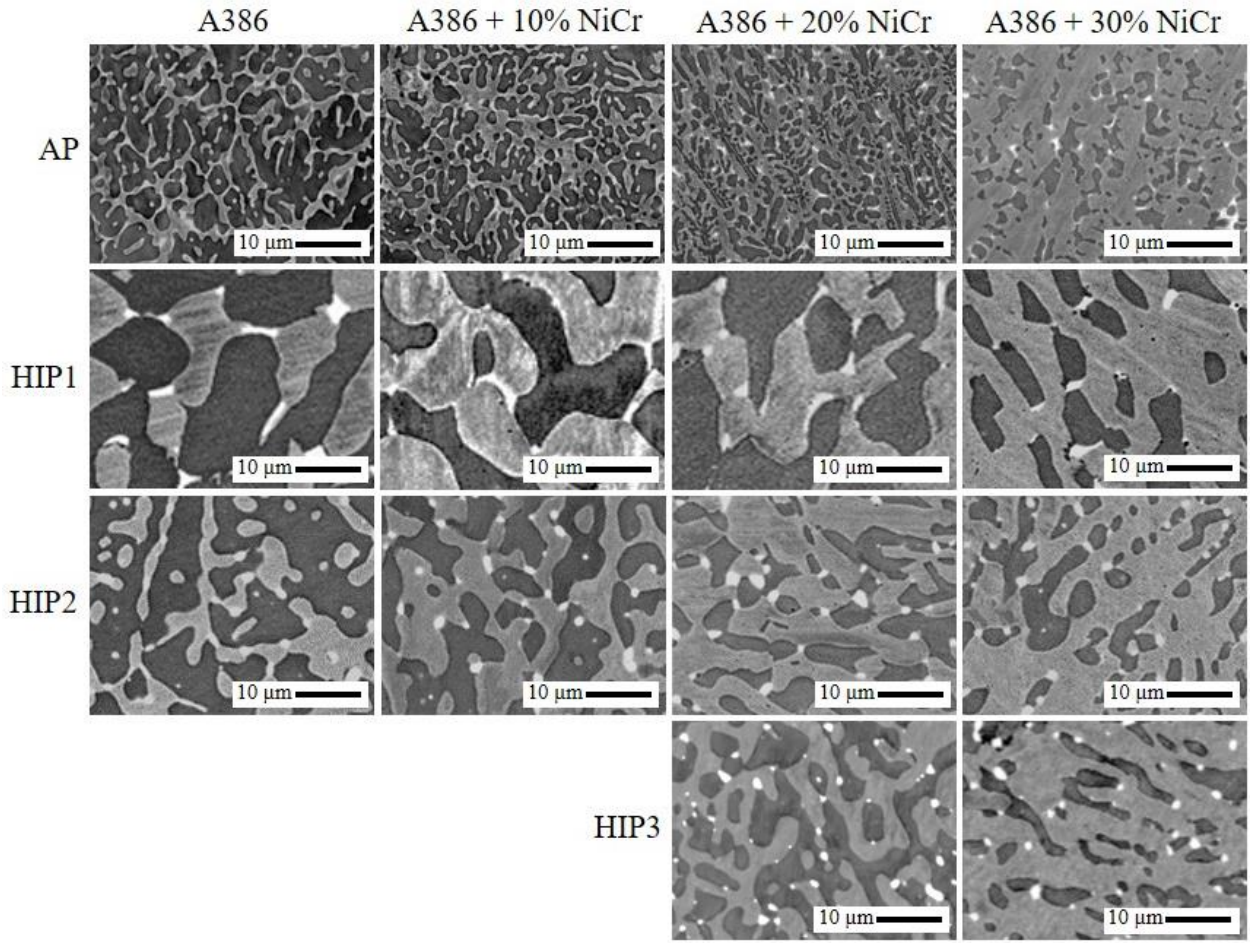

Figure 28: SEM backscatter images of laser-DED fabricated A386 + NiCr mixture coupon microstructures in the AP and HIP'd states.

The similar XRD peak intensities for samples with the same composition in Figure 29 show that the amount of β was relatively unaffected by the HIP treatments. Since HIP treatments do not change an alloys composition, no significant change in the percent area fraction of each phase was observed between the four treatments for each A386 + NiCr mixture. For example, the percent area of β in the A386 + 30% NiCr samples were 29.35 ± 4.22% for AP, 31.81 ± 1.44% for HIP1, 30.71 ± 4.68% for HIP2, and 28.94 ± 1.63% for HIP3. Different thermal histories will vary a grain's shape and size, but there should be relatively the same amount of each constituent phase present before and after the HIP treatment barring the precipitation of additional phases during heat treatment.

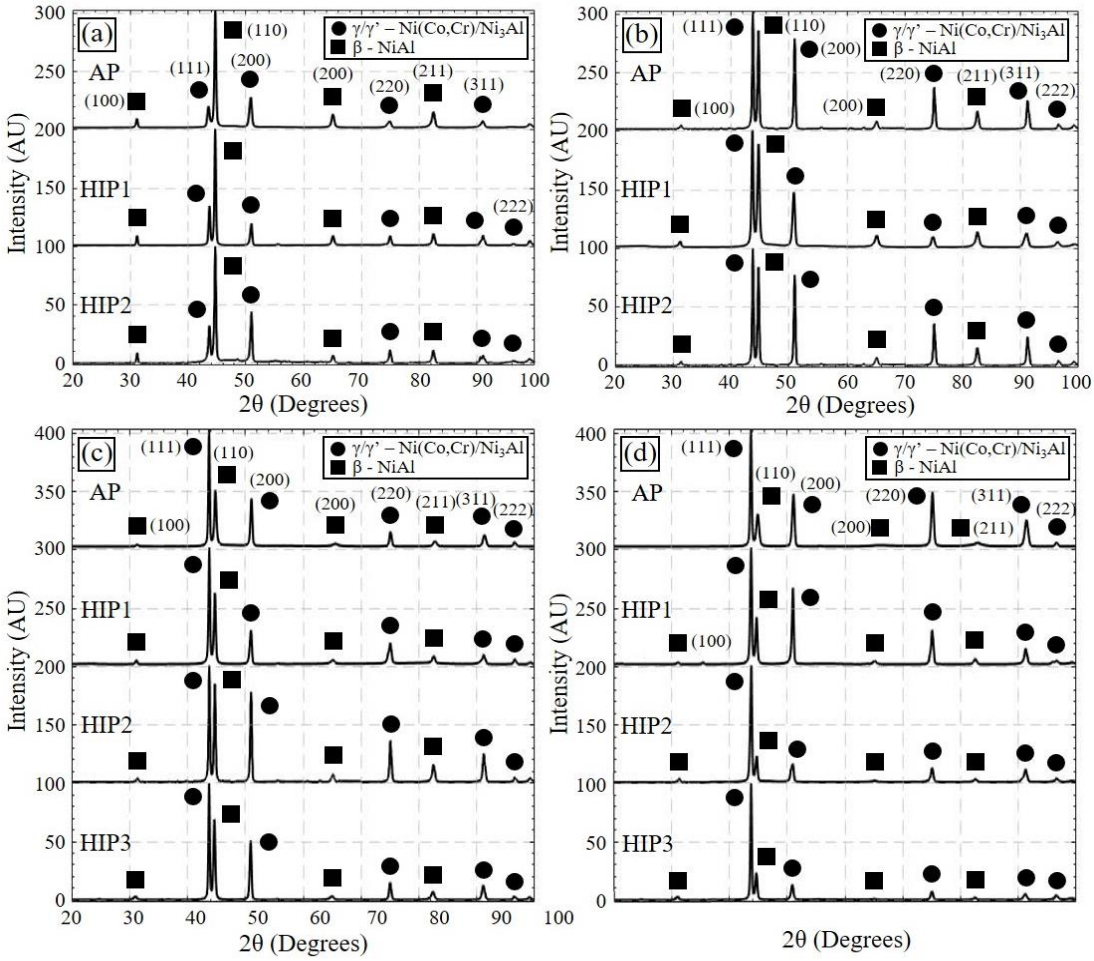

Figure 29: XRD plots of A386 + NiCr mixture coupons in the AP and HIP'd states: (a) A386, (b) A386 + 10% NiCr, (c) A386 + 20% NiCr, and (d) A386 + 30% NiCr.

Figure 30 shows small round precipitates of α–Cr within the β phase of the A386 + 30% NiCr HIP3 coupon. The α-Cr phase locally promotes the formation of chromia flakes, but is brittle, and has inferior oxidation resistance compared to the β and γ phases. The α–Cr phase also embrittles the scale/metal interface which accelerates scale spallation. Overall, the α–Cr phase precipitated during the HIP treatment is undesirable and has detrimental effects on the ductility and corrosion resistance of NiCoCrAlY alloys.

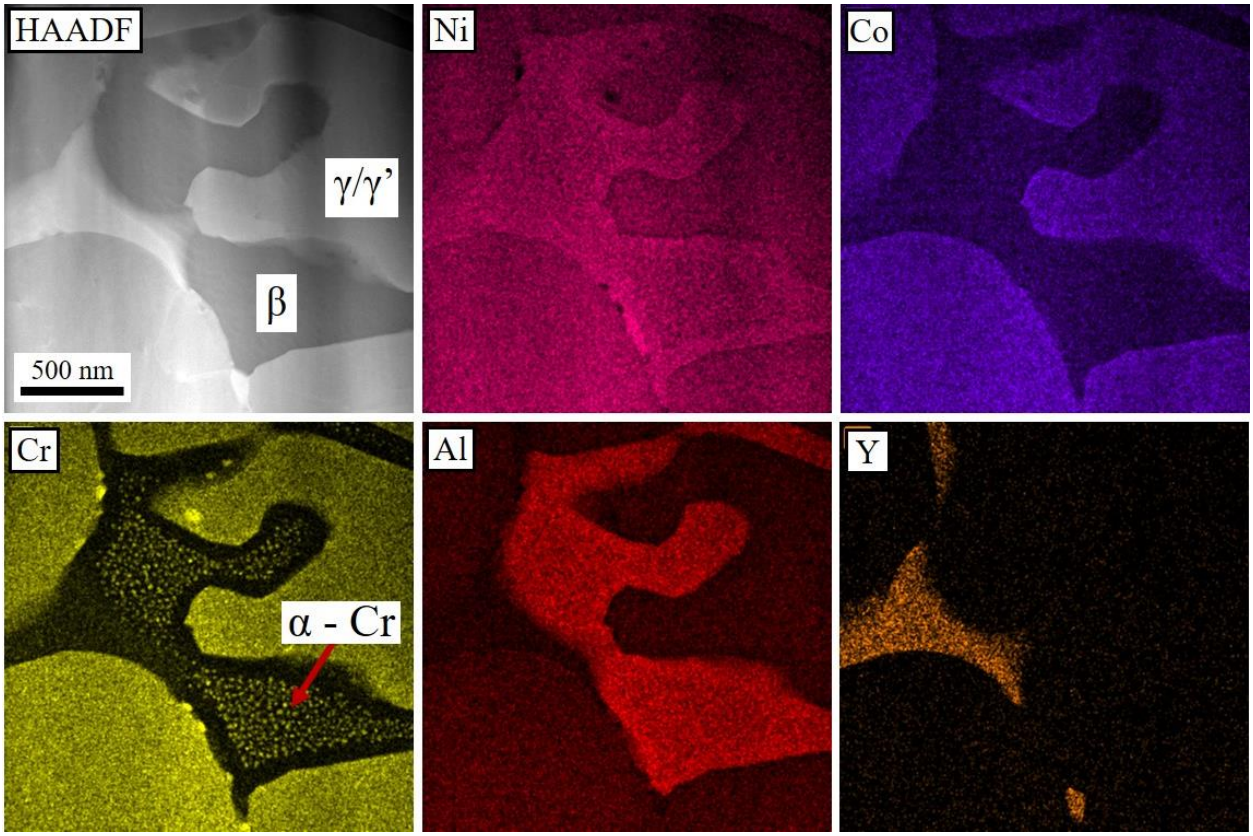

Figure 30: TEM-EDS of the A386 + 30% NiCr mixture coupon after HIP3.

4.3.4 Mechanical Behavior

4.3.4.1 Microhardness

Microhardness measurements were collected from the center of each mounted sample and the average hardness results are shown in Figure 31. The sample hardness is shown to decrease as the amount of NiCr is increased due to the higher amounts of γ/γ' present in the microstructure. Samples in the AP state show the highest hardness for each mixture, followed by HIP2, HIP3, and HIP1. The HIP1 treated samples have the lowest hardness values due to this treatment causing the highest amount of grain growth. The AP coupons have a martensitic microstructure due to the rapid cooling associated with laser AM processes and therefore have the highest hardness. HIP1 treatment had a higher temperature (1250 °C) than the HIP2 and HIP3 treatments (1150 °C) so the

HIP2 and HIP3 treated coupons underwent less annealing and grain coarsening, and therefore have slightly higher hardness than the HIP1 treated coupons.

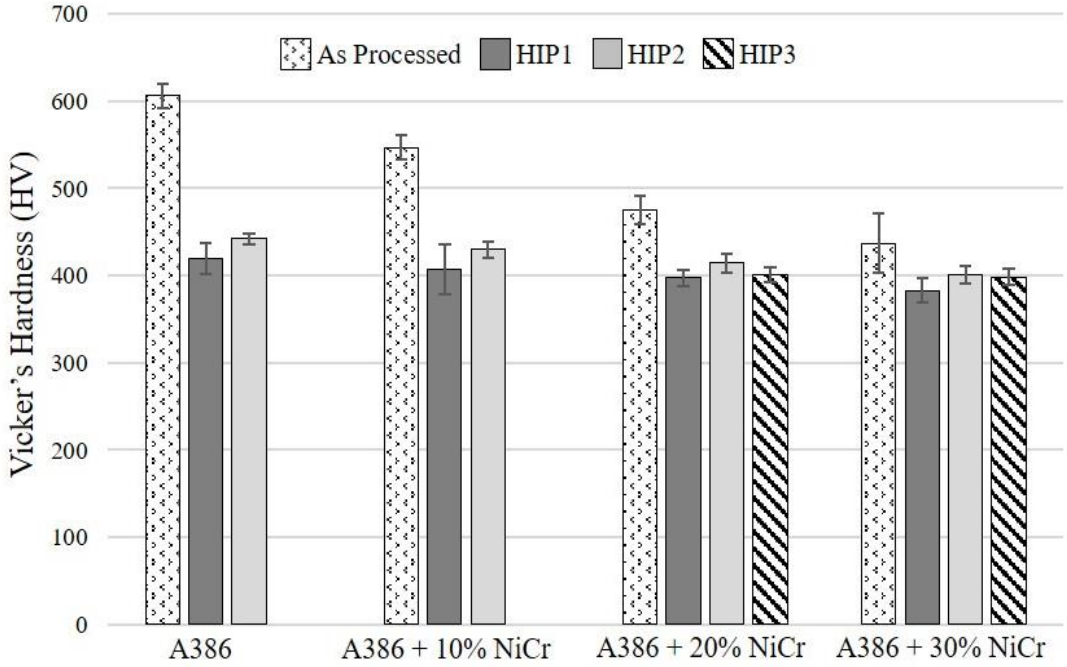

Figure 31: Vicker's hardness values for A386 + NiCr mixture coupons in the AP and HIP'd states.

4.3.4.2 High Temperature Tensile Testing

NiCo alloys are often used for high temperature applications so high temperature tensile properties are of interest. A386 +20% NiCr and A386 + 30% NiCr tensile bars were tested after HIP3. The red and green lines in Figure 32 show the results from the high temperature tensile tests. The high temperature mechanical properties drop rapidly as the temperature exceeds 700 °C. The A386 + 30% NiCr tensile bars exhibited tensile strength which was 5 – 25% higher than that of the A386 + 20% NiCr tensile bars. This result is presumed to be because of the greater amount of the brittle β phase in the A386 + 20% NiCr, and/or because there were relatively more microcracks present in the A386 + 20% NiCr coupon that were not healed during HIP3 (1150 °C). The HIP'd A386 + 20% & 30% NiCr tensile results are much lower than published values of similar heat

treated and/or single crystal alloys because these tensile bars were fully annealed during HIP'ing and did not undergo strengthening treatments thereafter. However, the HIP'd A386 + 20% & 30% NiCr tensile results are comparable to those of solution annealed Haynes 214, which is an alloy developed to provide optimum high-temperature oxidation resistance.

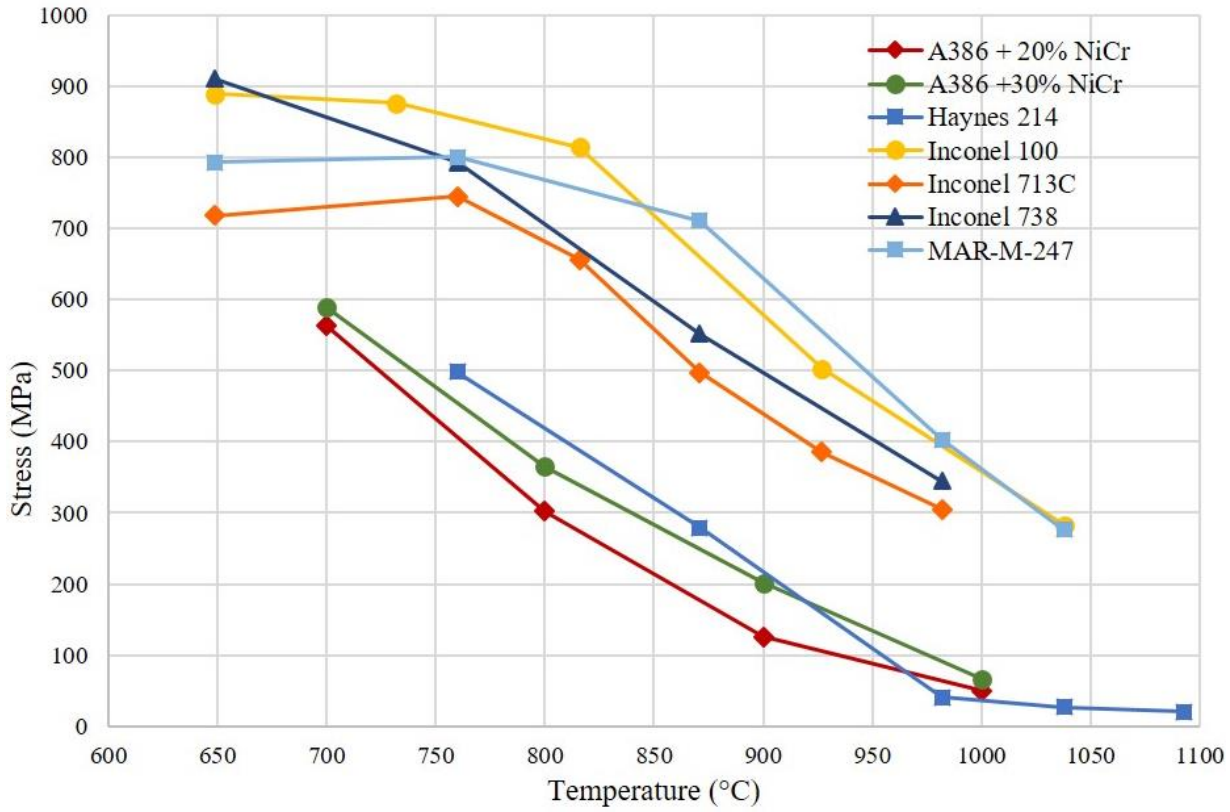

Figure 32: High temperature tensile properties of HIP'd A386 + 20% & 30% NiCr mixtures and similar alloys [127-131].

4.3.4.3 Nanoindentation

The room temperature elastic modulus of the A386 + 20% NiCr and A386 + 30% NiCr mixtures after HIP3 was found using nanoindentation and the following formula

$$E = \frac{1 - v^2}{\frac{1}{E_{eff}} - \frac{1 - v_i^2}{E_i}}$$

where E is the measured material's elastic modulus, ν is the material's Poisson ratio (assumed to be ν = 0.3), E_{eff} is the effective elastic modulus, E_i is the indenter's elastic modulus (diamond indenter: E_i = 1141 GPa), and ν_i is the indenter's Poisson ratio (diamond indenter: ν_i = 0.07). E_{eff} is calculated by the nanoindenter's software for each indentation. The room temperature elastic modulus for A386 + 20% NiCr and A386 + 30% NiCr were calculated to be 132.32 and 143.46 GPa respectively.

4.3.4.4 Residual Stress Measurement

Residual stress values were calculated using Hooke's Law, seen below

$$\sigma = E\varepsilon$$

where σ is stress in Pa, E is the elastic modulus in Pa, and ε is strain measured by the strain gage attached to the sample during slitting experiments. The elastic modulus values were obtained from nanoindentation measurements detailed in the previous section. Residual stress values for each increment are plotted in Figure 33.

Residual stress in the AP A386 + 20% NiCr and A386 + 30% NiCr samples are shown by the orange and grey lines respectively in the figure below. It can be seen that the magnitude of residual stress is nearly always higher for the A386 + 20% NiCr samples. The larger magnitude residual stresses can be directly related to the higher susceptibility to cracking of the A386 + 20% NiCr samples compared to A386 + 30% NiCr samples. After HIP'ing, the residual stresses are negligible which contributes to the increase in structural integrity observed after HIP treatments. The difference in edge conditions (stresses trending towards zero at Z = 0 mm, and trending upward at Z = 9 mm) is thought to be due to edge effects caused by EDM cutting prior to the slitting experiment. AM structures have been shown to exhibit tensile residual stresses near the edges of a sample and compressive residual stresses in the middle of a sample [132-133] which is

shown to be true in Figure 33 if the plot were cut off between Z = 1 and Z = 2 mm to remove edge effects.

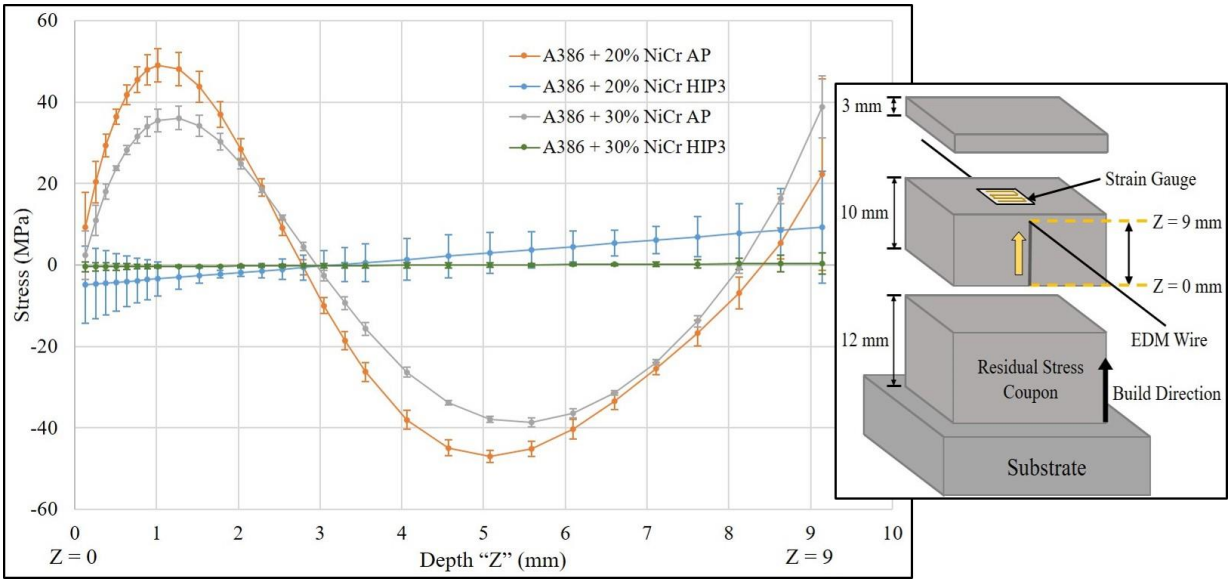

Figure 33: Residual stress plot and slitting diagram for A386 + 20% & 30% NiCr mixtures in AP and HIP3 states.

4.3.5 Crack Healing

Figure 34 shows evidence of crack healing in the 100% A386 coupons after the HIP1 treatment. During the hottest tested HIP cycle (HIP1 at 1250 °C), the lower melting point γ/γ' phase [134] began to fill open cracks, and some areas near the crack became devoid of γ/γ'. No other instances of crack healing were found for any other HIP and mixture combinations. It is thought that crack healing was only observed in the 100% A386 coupon subjected to HIP1 treatment because the 100% A386 samples had the largest cracks, highest crack density, and the compositions with more NiCr either had lesser cracks prior to HIP'ing, or the cracks were completely healed and unrecognizable after recrystallization. Also, crack healing is difficult to show or prove without high power CT or neutron scanning to characterize internal cracks and defects before and after HIP treatments, so crack healing may have taken place in other samples, but was not found.

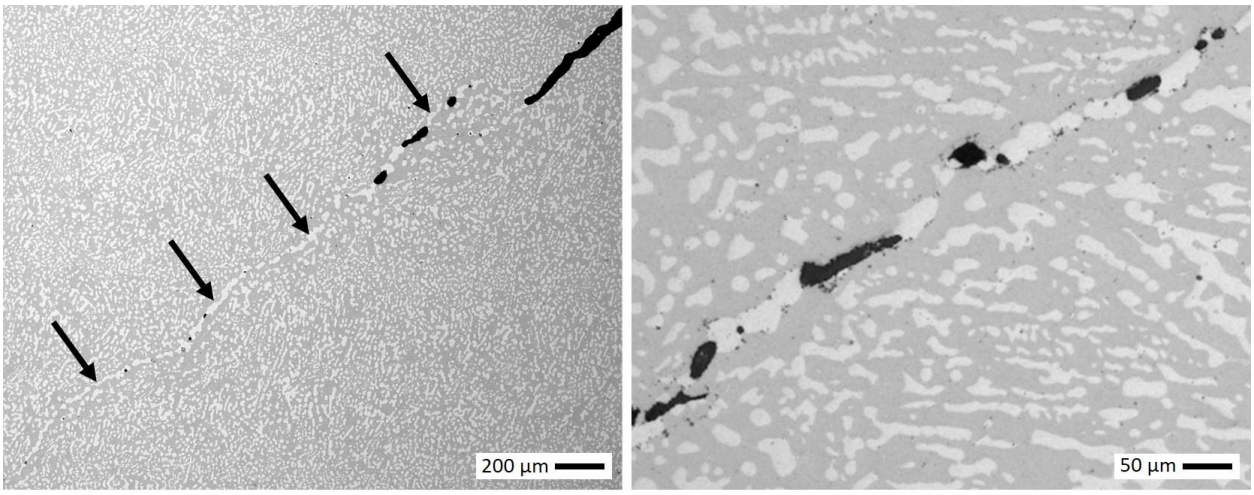

Figure 34: Partially healed crack in the 100% A386 coupon after HIP1 treatment.

4.4 Conclusions

The present work investigates the ability to increase the structural integrity of laser–DED processed NiCoCrAlY alloys using HIP. As seen previously, the NiCr additions to A386 increased the structural integrity during processing, but even the mixture coupons with the highest NiCr addition, A386 + 30% NiCr, cracked and warped during EDM machining. It was found that all A386 + NiCr coupons required stress relieving (this occurred during HIP cycles) before machining.

Various HIP parameters were explored to find a process which effectively reduced residual stresses, and densified laser–DED fabricated NiCoCrAlY coupons while causing the least amount of grain coarsening. The effects of HIP treatments on the structural integrity, residual stress, and porosity were evaluated by experimental materials characterization and testing. The residual stress and porosity in laser-DED fabricated NiCoCrAlY coupons was found to be reduced by all three HIP treatments. The microstructures after HIP1 treatment show the greatest amount of grain growth, and small pores with average diameter of 4.85 µm. The microstructures after HIP2 and HIP3 show relatively less grain growth and porosity with average diameters of 4.58 µm and 4.46

μm respectively, which is greater than that of HIP1, but less than the average pore diameter of 11.45 μm in the AP coupons.

Residual stress measurements show that the A386 + 20% NiCr coupons had a higher magnitude of residual stress than the A386 + 30% NiCr coupons which can be directly related to the lesser structural integrity of the A386 + 20% NiCr coupons compared to that of the A386 + 30% NiCr coupons. HIP1 had the highest temperature which resulted in the largest grains and lowest hardness. The HIP2 and HIP3 temperatures were 100 °C less than that of HIP1, resulting in relatively lesser grain coarsening and higher hardness. Since all three HIP treatments successfully relieved internal stresses and densified the laser–DED coupons, more investigation is needed to find the minimum temperature, pressure, and hold time necessary to achieve optimized results. Minimizing these HIP parameters would reduce cycle time and grain growth. Reductions in cycle time would increase production efficiency, and minimizing grain growth would maximize hardness and mechanical strength in the HIP'd state.

Large coupons of A386 + 20% NiCr and A386 + 30% NiCr were fabricated by laser–DED for the purpose of producing high temperature tensile bars. After fabrication, these coupons were subjected to HIP3 parameters (same as HIP2) to densify and relieve internal stresses in preparation for wire EDM cutting. The A386 + 30% NiCr tensile bars exhibited tensile strength properties which were 5 – 25% higher than that of the A386 + 20% NiCr tensile bars. This difference in tensile strength is thought to be due to a relatively higher amount of microcracks present in the A386 + 20% NiCr coupons than the A386 + 30% NiCr which were not healed during the lesser temperature (1150 °C) of HIP3.

Evidence of crack healing was found in a HIP1 treated A386 coupon. No other instances of crack healing were found for any other HIP and mixture combinations. It is thought that crack

healing was only observed in the 100% A386 coupon subjected to HIP1 treatment because the 100% A386 samples had the largest cracks, highest crack density, and the compositions with more NiCr either had no cracks prior to HIP'ing, or the cracks were completely healed and unrecognizable after recrystallization. Also, crack healing is difficult to show or prove without high power CT or neutron scanning to characterize internal cracks and defects before and after HIP treatments, so crack healing may have taken place in other samples which was not observed.

Our results show that HIP treatments can be a crucial process to substantially increase structural integrity, relieve residual stresses, reduce porosity, and potentially repair small cracks in laser–DED processed NiCoCrAlY structures. Additional studies need to be performed to find the minimum HIP parameters needed to obtain the desired results.

CHAPTER 5:

EXPLORATION OF MCrAlY HEAT TREATMENT FOR MECHANICAL STRENGTHENING

5.1 Introduction

HIP treatments are often used to densify and improve structural integrity of metal structures, but these benefits do not come without drawbacks [135-139]. For example, metal alloys are often annealed, and undergo grain coarsening during HIP treatments [140-141]. Annealing can relieve residual stresses, reduce microstructural defects, and increase ductility, but it also reduces mechanical properties. Grain growth also reduces mechanical properties even though it increases a materials resistance to creep and stress rupture. Metal alloys are often heat treated during or after HIP'ing to increase mechanical properties [142-143]. This chapter explores the heat treatability of NiCoCrAlY alloys to increase mechanical properties by quenching.

5.2 Materials and Methods

5.2.1 Production of DED Fabricated, HIP'd Heat Treatment Coupons

One small bar coupon with dimensions of 15 mm × 35 mm × 15 mm tall was fabricated for each of the A386 + 20% NiCr and A386 + 30% NiCr mixtures. The deposition parameters used to fabricate these coupons were 500 W laser power, 900 µm diameter spot size (approximate power density = 800 MW/m^2), 0.45 mm hatch spacing and layer thickness, and 25 mm/s laser scan speed. After deposition, these coupons were cut from the substrate by an abrasive cutoff saw (Presi Mecatome T260 – Eybens, FRANCE), treated with HIP3 parameters, and subsequently cut into slices measuring 15 mm × 15 mm × 3 mm thick by the aforementioned cutoff saw.

5.2.2 Solutionizing and Quenching

The 3 mm thick slices were solutionized in a tube furnace (Thermo Scientific Lindberg Blue M - Waltham, MA, USA) at 1200 °C for one hour, and then immediately submerged in water to achieve a rapid quench.

5.2.3 Metallographic Sample Preparation

Each quenched coupon was mounted in thermosetting polymer mounting compound and wet ground from 60 to 1200 grit. The mounted coupons were polished using a 0.06 μm colloidal silica solution until all scratches were removed. After polishing, the coupons were cleaned in a 100% ethanol ultrasonic bath (SharperTEK XP PRO – MI, USA).

5.3 Results and Discussion

Figure 35 shows the laser-DED fabricated coupons which are of the desired dimensions, 15 mm × 35 mm × 15 mm tall.

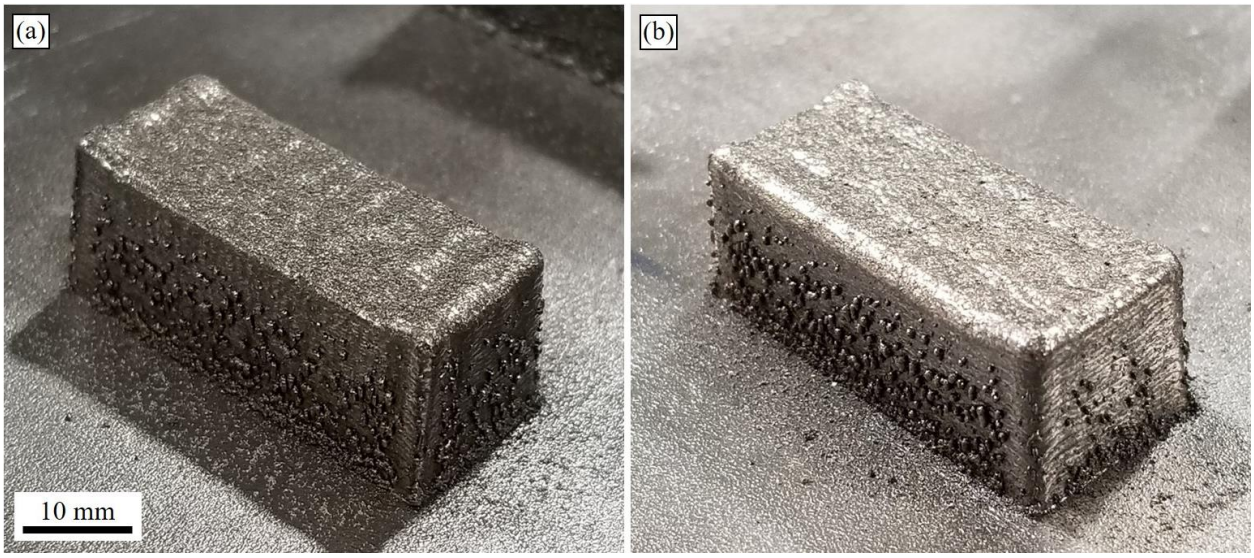

Figure 35: Heat treatment exploration coupons of: (a) A386 + 20% NiCr, and (b) A386 + 30% NiCr mixtures.

Figure 36 shows the microstructures and cracks formed during quenching. Intergranular cracking can be seen in both the A386 + 20% NiCr and A386 + 30% NiCr quenched microstructures.

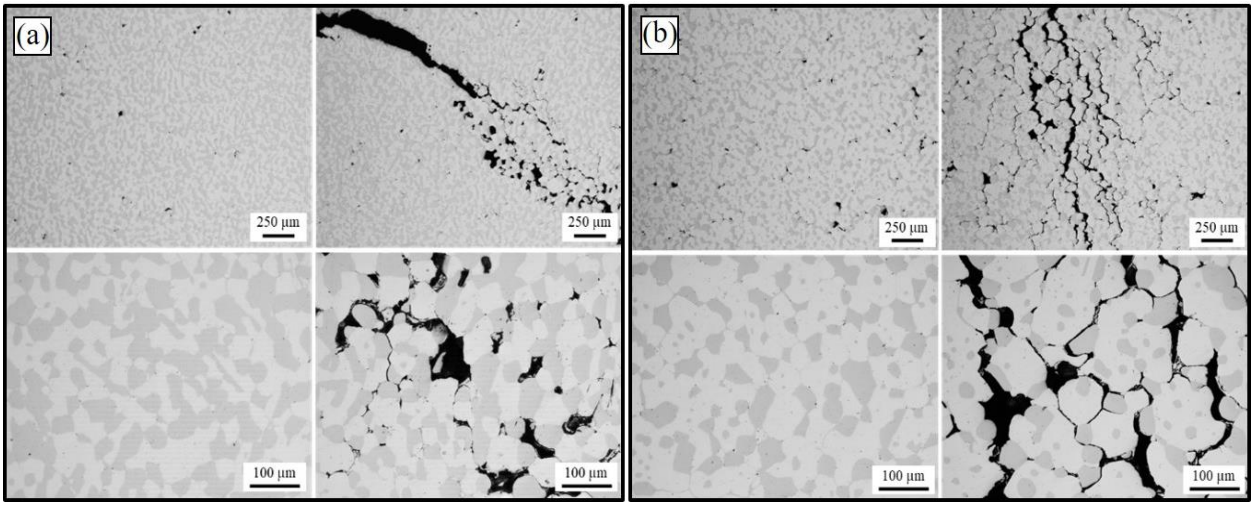

Figure 36: Optical micrographs of: (a) A386 + 20% NiCr, and (b) A386 + 30% NiCr mixture coupons after quenching.

Figure 37 shows SEM-EDS color maps of the A386 + 20% NiCr microstructure after HIP3, but before solutionizing and quenching.

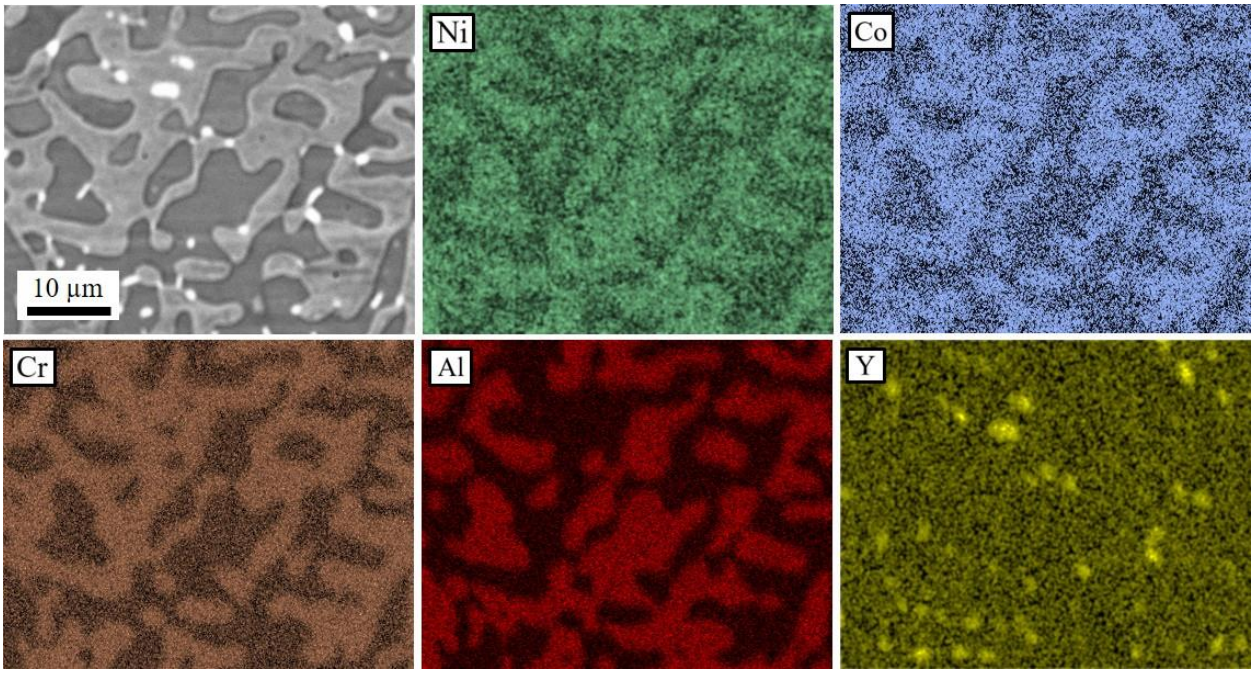

Figure 37: SEM-EDS of the A386 + 20% NiCr mixture coupon before quenching (HIP3 state).

Figure 38 shows SEM-EDS color maps of the A386 + 20% NiCr microstructure after quenching at low magnification. This figure shows yttrium rich phases which segregated to the grain boundaries causing intergranular cracking. Yttrium rich phases are pushed to the grain boundaries

because yttrium has no solubility in the γ/γ' or β phases [102]. Good alternatives to yttrium in MCrAl alloys for quenching are hafnium and zirconium which are completely soluble in the γ-Ni matrix and would not segregate to the grain boundaries if present in concentrations typical for RE-additions (up to 0.6 wt%) [144].

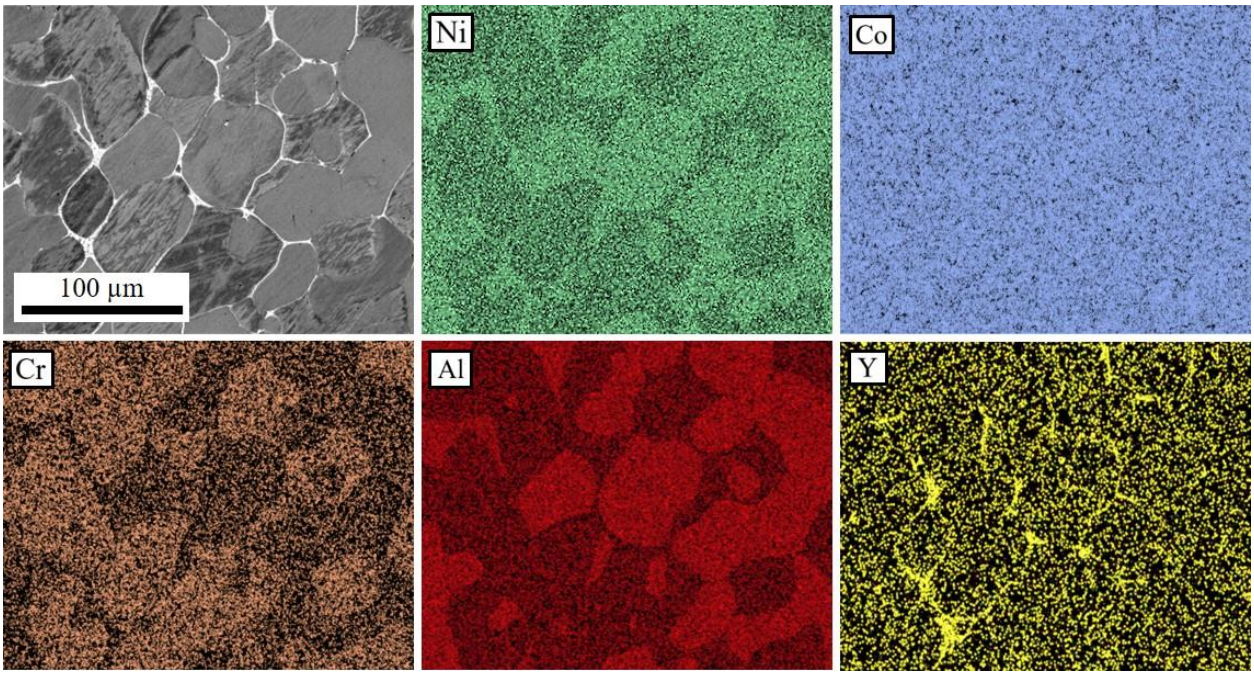

Figure 38: SEM-EDS of the A386 + 20% NiCr mixture coupon after solutionizing and quenching.

5.4 Conclusions

It can be concluded that the yttrium rich phases in the grain boundaries caused brittle, intergranular cracking during quenching. Due to this cracking, it is concluded that NiCoCrAlY alloys are not heat treatable by quenching.

CHAPTER 6:

CONCLUSIONS

The goal of the presented work was to create a method which could produce near net shape, bulk structures of a NiCoCrAlY alloy in a reasonable amount of time. Since current manufacturing processes for this alloy have either low geometric accuracy (particle spray), or low deposition rate (vapor deposition), different manufacturing processes needed to be considered. Directed energy deposition (DED) was chosen for this application because it is a freeform, near net shape manufacturing process which has relatively high geometric accuracy, and high deposition rates.

A NiCoCrAlY alloy (tradename "Amdry 386") was chosen for bulk fabrication. It was not possible to fabricate bulk structures from this alloy using DED due to hot cracking and delamination defects formed during deposition. To increase the fabricability of this alloy, a NiCr alloy was added in increasing amounts, creating three new alloy chemistries. The effects of alloy modification on the fabricability, structural integrity, and hardness were evaluated by experimental materials characterization and testing. The as-received A386 and NiCr feedstock powders were comprised of mostly β with smaller amounts of γ/γ′ phases, and almost completely γ/γ′, respectively. The constituent phases of A386 powder were retained in relatively the same proportions after laser-DED processing. The dominating phase switches from β to γ/γ' between the A386 and A386 + 10% NiCr mixtures, but the increase in structural integrity is not observed until the NiCr additions reach a minimum of 20%. The modified alloy chemistries allowed for the successful fabrication of larger-scale components. Specifically, the A386 + 30% NiCr composition is reported to be a viable mixture for direct laser fabrication of near-net shaped components. A plate and a bar geometry were successfully fabricated using laser-DED, with the largest dimensions on the order of tens of centimeters.

HIP treatments were investigated for their ability to increase the structural integrity of laser–DED processed NiCoCrAlY alloys. Due to cracking and warping in the AP coupons during EDM machining, it was found that all A386 + NiCr coupons required stress relieving (this occurred during HIP cycles) before machining. Various HIP parameters were explored to find a process which effectively reduced residual stresses and densified laser–DED fabricated NiCoCrAlY coupons while causing the least amount of grain coarsening. The effects of HIP treatments on the structural integrity, residual stress, and porosity were evaluated by experimental materials characterization and testing. The residual stress and porosity in laser-DED NiCoCrAlY coupons was found to be reduced by all three HIP treatments. The microstructures after HIP1 treatment showed the greatest amount of grain growth and small pores with an average diameter of 4.85 µm, which is greater than that of HIP2 and HIP3, but less than the average pore diameter of 11.45 µm for the AP coupons. The microstructures after HIP2 and HIP3 show relatively less grain growth and porosity with average diameter of 4.58 µm and 4.46 µm respectively. Residual stress measurements showed that the A386 + 20% NiCr coupons had a higher magnitude of residual stress than the A386 + 30% NiCr coupons which can be directly related to the lesser structural integrity of the A386 + 20% NiCr coupons compared to that of the A386 + 30% NiCr coupons. HIP1 had the highest temperature which resulted in the largest grains and lowest hardness. The HIP2 and HIP3 temperatures were 100 °C less than that of HIP1, resulting in relatively lesser grain coarsening and higher hardness. Since all three HIP treatments successfully relieved internal stresses and densified the laser–DED coupons, more investigation is needed to find the minimum temperature, pressure, and hold time necessary to achieve optimum results. Minimizing these HIP parameters would reduce cycle time, and grain growth which would increase production efficiency, and maximize hardness and mechanical strength in the HIP’d state.

Large coupons of A386 + 20% NiCr and A386 + 30% NiCr were fabricated by laser–DED for the purpose of producing high temperature tensile bars. After fabrication, these coupons were subjected to HIP3 parameters (same as HIP2) to densify and relieve internal stresses in preparation for EDM cutting. The A386 + 30% NiCr tensile bars exhibited tensile strength properties which were 5 – 25% higher than that of the A386 + 20% NiCr tensile bars. This difference in tensile strength is thought to be due to a relatively higher amount of microcracks present in the A386 + 20% NiCr coupons than the A386 + 30% NiCr which were not healed during the lesser temperature (1150 °C) of HIP3.

Evidence of crack healing was found in a HIP1 treated A386 coupon. No other instances of crack healing were found for any other HIP and mixture combinations. It is thought that crack healing was only observed in the 100% A386 coupon subjected to HIP1 treatment because the 100% A386 samples had the largest cracks, highest crack density, and the compositions with more NiCr either had no cracks prior to HIP'ing, or the cracks were completely healed and unrecognizable after recrystallization. The results show that HIP treatments can be a crucial process to substantially increase structural integrity, relieve residual stresses, reduce porosity, and repair small cracks in laser–DED processed NiCoCrAlY structures.

The heat treatability of NiCoCrAlY alloys to increase mechanical properties by quenching after being annealed by HIP'ing was explored. It is concluded that the yttrium rich phases which migrate to the grain boundaries during solutionizing cause brittle, intergranular cracking during quenching. Due to this cracking, it is concluded that NiCoCrAlY alloys are not able to be strengthened by quenching.

CHAPTER 7:

FUTURE WORKS

Metal additive manufacturing processes have completely transformed the manufacturing industry, but there are still many areas in which they are lacking. For instance, powder bed processes have slow build rates, and are unable to fabricate large and/or multi-material structures while directed energy deposition (DED) processes lack the ability to deposit structures with adequate build resolution. In addition to drawbacks/downfalls of individual processes, all metal additive manufacturing processes struggle to fabricate components from refractory metals and "unweldable" alloys as defined earlier.

Directed energy deposition leads all other metal additive manufacturing technology in deposition rate, build envelope size, range of applications, material selection, and multi material capabilities. Although the advantages are numerous, the build resolution created by DED is far worse than other processes such as powder bed fusion. DED's high deposition rates can be attributed to the process' high energy input, high material feed rates, large electron beam or laser spot size, large layer thickness, and large hatch spacing capabilities. Unfortunately, these capabilities which facilitate high deposition rates are also the largest contributors to the poor build resolution common to the DED process. The build resolution of DED structures can be improved by reducing the parameters such as laser power outlined above, but this improvement comes at the expense of the high deposition rates [145-146]. Since there are no current methods to increase build resolution without reducing deposition rates, components fabricated by DED often need to be machined after processing to meet specified geometric tolerances. To decrease overall manufacturing time, engineers have created "hybrid" machines which incorporate DED and traditional subtractive machining equipment into a single machine. Current hybrid machines only

slightly increase efficiency because they can only perform one operation (additive or subtractive machining) at a time. Future DED research will involve increasing DED build resolution while maintaining superior deposition rates, perhaps by utilizing multiple lower deposition rate (higher resolution) print heads simultaneously, or by creating hybrid machines which could perform additive and subtractive machining operations simultaneously.

Refractory and unweldable alloys are difficult to process using any manufacturing technique, but current and future research on additive manufacturing techniques will lead to new solutions. Metal additive manufacturing technologies which completely melt powder or wire feedstock using concentrated energy sources struggle to fabricate these materials due to hot cracking and the accumulation of residual stresses within a deposition. Researchers are currently working to eliminate hot cracking in additively manufactured structures by reducing energy input [147-148], and employing heated baseplates [145, 149]. Reducing energy input and the use of temperature-controlled baseplates reduces the thermal gradients within a structure during fabrication which are the driving force for hot cracking during deposition and form residual stresses during uneven cooling.

The next steps in the presented research work include corrosion testing, HIP parameter optimization, and investigating methods for strengthening HIP'd NiCoCrAlY alloys. The NiCr additions to the Amdry 386 alloy reduce the amount of aluminum which will detrimentally affect the alloy's hot corrosion resistance. Corrosion testing needs to be conducted to investigate how much of Amdry 386's corrosion resistance is lost for each NiCr addition, and for comparison with similar laser processable, corrosion resistant superalloys. The mechanical properties of the HIP'd NiCoCrAlY alloys are directly related to the effects HIP'ing has on their microstructure. As seen with the extensive amount of grain growth seen in HIP1 samples versus the lesser grain growth

in the HIP2 and HIP3 samples, the 100 °C difference in HIP temperature has a large effect on the grain size. Optimizing HIP parameters such that residual stresses are relieved, but grain growth is minimized will increase the mechanical properties of HIP'd samples. In addition to HIP parameter optimization, strengthening methods such as quenching, tempering, precipitation hardening, oxide dispersion strengthening, and solid solution strengthening should be investigated for increasing the mechanical properties of HIP'd A386 + NiCr alloys. Since yttrium has no solubility in γ/γ' or β, yttrium rich phases were pushed to the grain boundaries during solutionizing and promoted intergranular cracking upon quenching. To reduce intergranular cracking, other RE's such as hafnium and zirconium which are completely soluble in the γ/γ' matrix should be investigated.

REFERENCES

[1] Quan, Z., Wu, A., Keefe, M., Qin, X., Yu, J., Suhr, J., Byun, J.H., Kim, B.S. & Chou, T. W. (2015). Additive manufacturing of multi-directional preforms for composites: opportunities and challenges. *Materials Today*, *18*(9), 503-512

[2] Ford, S., & Despeisse, M. (2016). Additive manufacturing and sustainability: an exploratory study of the advantages and challenges. *Journal of cleaner Production*, *137*, 1573-1587.

[3] Gibson, I., Rosen, D. W., Stucker, B., Khorasani, M., Rosen, D., Stucker, B., & Khorasani, M. (2021). Additive manufacturing technologies (Vol. 17). Cham, Switzerland: Springer.

[4] Beyer, C. (2014). Strategic implications of current trends in additive manufacturing. Journal of Manufacturing Science and Engineering, 136(6).

[5] Shidid, D., Leary, M., Choong, P., & Brandt, M. (2016). Just-in-time design and additive manufacture of patient-specific medical implants. Physics Procedia, 83, 4-14.

[6] Najmon, J. C., Raeisi, S., & Tovar, A. (2019). Review of additive manufacturing technologies and applications in the aerospace industry. Additive manufacturing for the aerospace industry, 7-31.

[7] Grigor'Ev, S. N., & Tarasova, T. V. (2016). Possibilities of the technology of additive production for making complex-shape parts and depositing functional coatings from metallic powders. Metal science and heat treatment, 57, 579-584.

[8] Talignani, A., Seede, R., Whitt, A., Zheng, S., Ye, J., Karaman, & Wang, Y. M. (2022). A review on additive manufacturing of refractory tungsten and tungsten alloys. Additive Manufacturing, 103009.

[9] Hallgren, S., Pejryd, L., & Ekengren, J. (2016). (Re) Design for additive manufacturing. Procedia Cirp, 50, 246-251.

[10] Emmelmann, C., Scheinemann, P., Munsch, M., & Seyda, V. (2011). Laser additive manufacturing of modified implant surfaces with osseointegrative characteristics. Physics Procedia, 12, 375-384.

[11] Vignesh, M., Ranjith Kumar, G., Sathishkumar, M., Manikandan, M., Rajyalakshmi, G., Ramanujam, R., & Arivazhagan, N. (2021). Development of biomedical implants through additive manufacturing: A review. Journal of Materials Engineering and Performance, 30, 4735-4744.

[12] Li, C., Pisignano, D., Zhao, Y., & Xue, J. (2020). Advances in medical applications of additive manufacturing. Engineering, 6(11), 1222-1231.

[13] Liu, R., Wang, Z., Sparks, T., Liou, F., & Newkirk, J. (2017). Aerospace applications of laser additive manufacturing. In Laser additive manufacturing (pp. 351-371). Woodhead publishing.

[14] Diaz, A. (2019). Surface texture characterization and optimization of metal additive manufacturing-produced components for aerospace applications. In Additive manufacturing for the aerospace industry (pp. 341-374). Elsevier.

[15] Savitha, U., Srinivas, V., Reddy, G. J., Gokhale, A. A., & Sundararaman, M. (2018). Additive laser deposition of YSZ on Ni base superalloy for thermal barrier application. Surface and Coatings Technology, 354, 257-267.

[16] Feuerstein, A., Knapp, J., Taylor, T., Ashary, A., Bolcavage, A., & Hitchman, N. (2008). Technical and economical aspects of current thermal barrier coating systems for gas turbine engines by thermal spray and EBPVD: a review. Journal of Thermal Spray Technology, 17(2), 199-213.

[17] Gell, M., Wang, J., Kumar, R., Roth, J., Jiang, C., & Jordan, E. H. (2018). Higher temperature thermal barrier coatings with the combined use of yttrium aluminum garnet and the solution precursor plasma spray process. Journal of Thermal Spray Technology, 27(4), 543-555.

[18] Sahasrabudhe, H., Bose, S., & Bandyopadhyay, A. (2018). Laser-based additive manufacturing processes. Advances in Laser Materials Processing, 507-539.

[19] Pereira, T., Kennedy, J. V., & Potgieter, J. (2019). A comparison of traditional manufacturing vs additive manufacturing, the best method for the job. Procedia Manufacturing, 30, 11-18.

[20] Iturbe, A., Giraud, E., Hormaetxe, E., Garay, A., Germain, G., Ostolaza, K., & Arrazola, P. J. (2017). Mechanical characterization and modelling of Inconel 718 material behavior for machining process assessment. Materials Science and Engineering: A, 682, 441-453.

[21] Cormier, J., Jouiad, M., Hamon, F., Villechaise, P., & Milhet, X. (2010). Very high temperature creep behavior of a single crystal Ni-based superalloy under complex thermal cycling conditions. Philosophical magazine letters, 90(8), 611-620.

[22] Hoffelner, W. (2013). Components and Its Production. In Materials for Nuclear Plants (pp. 135-195). Springer, London.

[23] Tong, C. (2019). Advanced materials enable energy production from fossil fuels. In Introduction to Materials for Advanced Energy Systems (pp. 171-230). Springer, Cham.

[24] Liu, Q., Huang, S., & He, A. (2019). Composite ceramics thermal barrier coatings of yttria stabilized zirconia for aero-engines. Journal of Materials Science & Technology, 35(12), 2814-2823.

[25] Mercier, S., Giovannetti, I., Josso, P., & Bacos, M. P. (2006). Analysis of the co-deposition of CrAlYTa particles with nickel by an electrolytic–electroless route: The influence of solution and hydrodynamic parameters. Surface and Coatings Technology, 201(1-2), 120-128.

[26] Chattopadhyay, R. (2004). Electron Beam Processes. Advanced Thermally Assisted Surface Engineering Processes, 135-147.

[27] Cinca, N., Lima, C. R. C., & Guilemany, J. M. (2013). An overview of intermetallics research and application: Status of thermal spray coatings. Journal of Materials Research and Technology, 2(1), 75-86.

[28] Vardelle, A., Moreau, C., Akedo, J., Ashrafizadeh, H., Berndt, C. C., Berghaus, J. O & Vuoristo, P. (2016). The 2016 thermal spray roadmap. Journal of thermal spray technology, 25(8), 1376-1440.

[29] Ang, A. S. M., & Berndt, C. C. (2014). A review of testing methods for thermal spray coatings. International Materials Reviews, 59(4), 179-223.

[30] Kumar, S., Selvarajan, V., Padmanabhan, P. V. A., & Sreekumar, K. P. (2006). Characterization and comparison between ball milled and plasma processed iron-aluminium thermal spray coatings. Surface and Coatings Technology, 201(3-4), 1267-1275.

[31] Higuera, V., Belzunce, F. J., & Riba, J. (2006). Influence of the thermal-spray procedure on the properties of a CoNiCrAlY coating. Surface and Coatings Technology, 200(18-19), 5550-5556.

[32] Gu, D. D., Meiners, W., Wissenbach, K., & Poprawe, R. (2012). Laser additive manufacturing of metallic components: materials, processes and mechanisms. International materials reviews, 57(3), 133-164.

[33] Seifi, S. H., Tian, W., Doude, H., Tschopp, M. A., & Bian, L. (2019). Layer-wise modeling and anomaly detection for laser-based additive manufacturing. Journal of Manufacturing Science and Engineering, 141(8).

[34] Kenel, C., Schloth, P., Van Petegem, S., Fife, J. L., Grolimund, D., Menzel, A. & Leinenbach, C. (2016). In situ synchrotron X-ray diffraction and small angle X-ray scattering studies on rapidly heated and cooled Ti-Al and Al-Cu-Mg alloys using laser-based heating. Jom, 68(3), 978-984.

[35] Ettefagh, A. H., & Guo, S. (2018). Electrochemical behavior of AISI316L stainless steel parts produced by laser-based powder bed fusion process and the effect of post annealing process. Additive Manufacturing, 22, 153-156.

[36] Li, W., Yan, L., Chen, X., Zhang, J., Zhang, X., & Liou, F. (2018). Directed energy depositing a new Fe-Cr-Ni alloy with gradually changing composition with elemental

powder mixes and particle size effect in fabrication process. Journal of Materials Processing Technology, 255, 96-104.

[37] Wang, Z., Lin, X., Kang, N., Chen, J., Tang, Y., Tan, H., Yu, X., Yang, H. & Huang, W. (2021). Directed energy deposition additive manufacturing of a Sc/Zr-modified Al–Mg alloy: effect of thermal history on microstructural evolution and mechanical properties. Materials Science and Engineering: A, 802, 140606.

[38] Sridharan, N., Cakmak, E., & Dehoff, R. R. (2019). Microstructure evolution during laser direct energy deposition of a novel Fe-Cr-Ni-WB hardfacing coating. Surface and Coatings Technology, 358, 362-370.

[39] Moorehead, M., Bertsch, K., Niezgoda, M., Parkin, C., Elbakhshwan, M., Sridharan, & Couet, A. (2020). High-throughput synthesis of Mo-Nb-Ta-W high-entropy alloys via additive manufacturing. Materials & Design, 187, 108358.

[40] Gibson, James SK-L., et al. "On extracting mechanical properties from nanoindentation at temperatures up to 1000 C." Extreme Mechanics Letters 17 (2017): 43-49.

[41] Gurrappa, I. "Influence of alloying elements on hot corrosion of superalloys and coatings: necessity of smart coatings for gas turbine engines." Materials science and technology 19.2 (2003): 178-183.

[42] Sun, Z., Guo, W., & Li, L. (2020). Numerical modelling of heat transfer, mass transport and microstructure formation in a high deposition rate laser directed energy deposition process. Additive Manufacturing, 33, 101175.

[43] Yang, Y., Gong, Y., Li, C., Wen, X., & Sun, J. (2021). Mechanical performance of 316 L stainless steel by hybrid directed energy deposition and thermal milling process. Journal of Materials Processing Technology, 291, 117023.

[44] Zhang, J., Gao, J., Song, B., Zhang, L., Han, C., Cai, & Shi, Y. (2021). A novel crack-free Ti-modified Al-Cu-Mg alloy designed for selective laser melting. Additive Manufacturing, 38, 101829.

[45] Andersson, J. O., Helander, T., Höglund, L., Shi, P., & Sundman, B. (2002). Thermo-Calc & DICTRA, computational tools for materials science. Calphad, 26(2), 273-312.

[46] Smith, J., Xiong, W., Yan, W., Lin, S., Cheng, P., Kafka & Liu, W. K. (2016). Linking process, structure, property, and performance for metal-based additive manufacturing: computational approaches with experimental support. Computational Mechanics, 57, 583-610.

[47] https://wordlesstech.com/first-ge-supersonic-commercial-jet-engine/

[48] Pomeroy, M. J. (2005). Coatings for gas turbine materials and long term stability issues. Materials & design, 26(3), 223-231.

[49] Bunker, R. S. (2006). Axial turbine blade tips: function, design, and durability. Journal of propulsion and power, 22(2), 271-285.

[50] Padture, N. P., Gell, M., & Jordan, E. H. (2002). Thermal barrier coatings for gas-turbine engine applications. Science, 296(5566), 280-284.

[51] Bezencon, C., Schnell, A., & Kurz, W. (2003). Epitaxial deposition of MCrAlY coatings on a Ni-base superalloy by laser cladding. Scripta Materialia, 49(7), 705-709.

[52] Tobar, M. J., Amado, J. M., Yáñez, A., Pereira, J. C., & Amigó, V. (2014). Laser cladding of MCrAlY coatings on stainless steel. Physics Procedia, 56, 276-283.

[53] Pereira, J. C., Zambrano, J. C., Rayón, E., Yañez, A., & Amigó, V. (2018). Mechanical and microstructural characterization of MCrAlY coatings produced by laser cladding: The influence of the Ni, Co and Al content. Surface and Coatings Technology, 338, 22-31.

[54] Pereira, J., Zambrano, J., Licausi, M., Tobar, M., & Amigo, V. (2015). Tribology and high temperature friction wear behavior of MCrAlY laser cladding coatings on stainless steel. Wear, 330, 280-287.

[55] Pereira, J. C., Zambrano, J., Yañez, A., & Amigó, V. (2021). Laser Cladding of MCrAlY Alloys. Laser Cladding of Metals, 363-394.

[56] Boettinger, W. J. (2016). The solidification of multicomponent alloys. Journal of phase equilibria and diffusion, 37, 4-18.

[57] Keller, T., Lindwall, G., Ghosh, S., Ma, L., Lane, B. M., Zhang & Levine, L. E. (2017). Application of finite element, phase-field, and CALPHAD-based methods to additive manufacturing of Ni-based superalloys. Acta materialia, 139, 244-253.

[58] Mireles, Omar, et al. "Additive manufacture of refractory alloy C103 for propulsion applications." AIAA Propulsion and Energy 2020 Forum. 2020.

[59] Philips, N. R., Carl, M., & Cunningham, N. J. (2020). New opportunities in refractory alloys. Metallurgical and Materials Transactions A, 51, 3299-3310.

[60] Martin, J. H., Ashby, D. S., & Schaedler, T. A. (2017). Thin-walled high temperature alloy structures fabricated from additively manufactured polymer templates. Materials & Design, 120, 291-297.

[61] Bandyopadhyay, A., & Heer, B. (2018). Additive manufacturing of multi-material structures. Materials Science and Engineering: R: Reports, 129, 1-16.

[62] Cronskär, M., Bäckström, M., & Rännar, L. E. (2013). Production of customized hip stem prostheses–a comparison between conventional machining and electron beam melting (EBM). Rapid Prototyping Journal, 19(5), 365-372.

[63] Roach, D. J., Hamel, C. M., Dunn, C. K., Johnson, M. V., Kuang, X., & Qi, H. J. (2019). The m4 3D printer: A multi-material multi-method additive manufacturing platform for future 3D printed structures. Additive Manufacturing, 29, 100819.

[64] Aashranth, B., Davinci, M. A., Samantaray, D., & Borah, U. (2019). Warm working as a potential substitute for hot working of austenitic steel in selected applications. Materials Performance and Characterization, 8(5), 957-968.

[65] AlMangour, B. (Ed.). (2019). Additive manufacturing of emerging materials. New York: Springer.

[66] ASTM, D. F. (2009). 2792-09. Standard Terminology for Additive Manufacturing Technologies. ASTM International.

[67] Mohd Yusuf, S., Cutler, S., & Gao, N. (2019). The impact of metal additive manufacturing on the aerospace industry. Metals, 9(12), 1286.

[68] Gradl, P., Tinker, D. C., Park, A., Mireles, O. R., Garcia, M., Wilkerson, R., & Mckinney, C. (2022). Robust metal additive manufacturing process selection and development for aerospace components. Journal of Materials Engineering and Performance, 31(8), 6013-6044.

[69] Monteiro, H., Carmona-Aparicio, G., Lei, I., & Despeisse, M. (2022). Energy and material efficiency strategies enabled by metal additive manufacturing–A review for the aeronautic and aerospace sectors. Energy Reports, 8, 298-305.

[70] Vignesh, M., Ranjith Kumar, G., Sathishkumar, M., Manikandan, M., Rajyalakshmi, G., Ramanujam, R., & Arivazhagan, N. (2021). Development of biomedical implants through additive manufacturing: A review. Journal of Materials Engineering and Performance, 30, 4735-4744.

[71] Yuan, L., Ding, S., & Wen, C. (2019). Additive manufacturing technology for porous metal implant applications and triple minimal surface structures: A review. Bioactive materials, 4, 56-70.

[72] da Silva, L. R. R., Sales, W. F., Campos, F. D. A. R., de Sousa, J. A. G., Davis, R., Singh, A., ... & Borgohain, B. (2021). A comprehensive review on additive manufacturing of medical devices. Progress in Additive Manufacturing, 6(3), 517-553.

[73] Sun, C., Wang, Y., McMurtrey, M. D., Jerred, N. D., Liou, F., & Li, J. (2021). Additive manufacturing for energy: A review. Applied Energy, 282, 116041.

[74] Was, G. S., Petti, D., Ukai, S., & Zinkle, S. (2019). Materials for future nuclear energy systems. Journal of Nuclear Materials, 527, 151837.

[75] Fu, C., Li, J., Bai, J., Li, Y., Chen, Q., Lei & Meng, Y. (2021). Effect of helium bubbles on irradiation hardening of additive manufacturing 316L stainless steel under high temperature He ions irradiation. Journal of Nuclear Materials, 550, 152948.

[76] Sutton, B., Herderick, E., Thodla, R., Ahlfors, M., & Ramirez, A. (2019). Heat treatment of alloy 718 made by additive manufacturing for oil and gas applications. Jom, 71, 1134-1143.

[77] Zhu, Q., & Yan, J. (2021). A mixed interface-capturing/interface-tracking formulation for thermal multi-phase flows with emphasis on metal additive manufacturing processes. Computer Methods in Applied Mechanics and Engineering, 383, 113910.

[78] Akselsen, O. M., Bjørge, R., Ånes, H. W., Ren, X., & Nyhus, B. (2021). Effect of Sigma Phase in Wire Arc Additive Manufacturing of Superduplex Stainless Steel. Metals, 11(12), 2045.

[79] Busachi, A., Erkoyuncu, J., Colegrove, P., Drake, R., Watts, C., & Wilding, S. (2018). Additive manufacturing applications in Defence Support Services: current practices and framework for implementation. International Journal of System Assurance Engineering and Management, 9, 657-674.

[80] Schrand, A. M. (2016). Additive manufacturing: from form to function. Strategic Studies Quarterly, 10(3), 74-90.

[81] Pettus, E. L. (2013). Building a competitive edge with additive manufacturing. Air War College Air University Maxwell AFB United States.

[82] Richer, P., Yandouzi, M., Beauvais, L., & Jodoin, B. (2010). Oxidation behaviour of CoNiCrAlY bond coats produced by plasma, HVOF and cold gas dynamic spraying. Surface and Coatings Technology, 204(24), 3962-3974.

[83] Liu, M. J., Zhang, G., Lu, Y. H., Han, J. Q., Li, G. R., Li, C. X., ... & Yang, G. J. (2020). Plasma spray–physical vapor deposition toward advanced thermal barrier coatings: a review. Rare Metals, 39, 479-497.

[84] Rockett, A. (2008). Physical vapor deposition. The materials science of semiconductors, 505-572.

[85] LeClair, P., Berera, G. P., & Moodera, J. S. (2000). Titanium nitride thin films obtained by a modified physical vapor deposition process. Thin Solid Films, 376(1-2), 9-15.

[86] Peng, H., Guo, H., He, J., & Gong, S. (2012). Microscale lamellar NiCoCrAlY coating with improved oxidation resistance. Surface and Coatings Technology, 207, 110-116.

[87] Li, Z., Gordon, R. G., Pallem, V., Li, H., & Shenai, D. V. (2010). Direct-liquid-injection chemical vapor deposition of nickel nitride films and their reduction to nickel films. Chemistry of Materials, 22(10), 3060-3066.

[88] Carlsson, J. O., & Martin, P. M. (2010). Chemical vapor deposition. In Handbook of Deposition Technologies for films and coatings (pp. 314-363). William Andrew Publishing.

[89] Liu, Y., Koep, E., & Liu, M. (2005). A highly sensitive and fast-responding SnO2 sensor fabricated by combustion chemical vapor deposition. Chemistry of materials, 17(15), 3997-4000.

[90] Shaw, J. C., Zhou, H., Chen, Y., Weiss, N. O., Liu, Y., Huang, Y., & Duan, X. (2014). Chemical vapor deposition growth of monolayer MoSe 2 nanosheets. Nano Research, 7, 511-517.

[91] Moshkalyov, S. A., Moreau, A. L. D., Guttiérrez, H. R., Cotta, M. A., & Swart, J. W. (2004). Carbon nanotubes growth by chemical vapor deposition using thin film nickel catalyst. Materials Science and Engineering: B, 112(2-3), 147-153.

[92] Bouchaud, B., Balmain, J., & Pedraza, F. (2008). Cyclic and isothermal oxidation at 1,100° C of a CVD aluminised directionally solidified Ni superalloy. Oxidation of metals, 69, 193-210.

[93] Zeng, C., Tian, W., Liao, W. H., & Hua, L. (2016). Microstructure and porosity evaluation in laser-cladding deposited Ni-based coatings. Surface and Coatings Technology, 294, 122-130.

[94] Vilar, R. (1999). Laser cladding. Journal of laser applications, 11(2), 64-79.

[95] Falcón, J. C. P., Echeverria, A., Afonso, C. R., Carrullo, J. C. Z., & Borrás, V. A. (2019). Microstructure assessment at high temperature in NiCoCrAlY overlay coating obtained by laser metal deposition. Journal of Materials Research and Technology, 8(2), 1761-1772.

[96] Li, Z., Chen, J., Sui, S., Zhong, C., Lu, X., & Lin, X. (2020). The microstructure evolution and tensile properties of Inconel 718 fabricated by high-deposition-rate laser directed energy deposition. Additive Manufacturing, 31, 100941.

[97] Saboori, A., Gallo, D., Biamino, S., Fino, P., & Lombardi, M. (2017). An overview of additive manufacturing of titanium components by directed energy deposition: microstructure and mechanical properties. Applied Sciences, 7(9), 883.

[98] Liu, R., Wang, Z., Sparks, T., Liou, F., & Newkirk, J. (2017). Aerospace applications of laser additive manufacturing. In Laser additive manufacturing (pp. 351-371). Woodhead publishing.

[99] Gibson, I., Rosen, D. W., Stucker, B., Khorasani, M., Rosen, D., Stucker, B., & Khorasani, M. (2021). Additive manufacturing technologies (Vol. 17). Cham, Switzerland: Springer.

[100] Pérez-Andrade, L. I., Gärtner, F., Villa-Vidaller, M., Klassen, T., Muñoz-Saldaña, J., & Alvarado-Orozco, J. M. (2019). Optimization of Inconel 718 thick deposits by cold spray processing and annealing. Surface and Coatings Technology, 378, 124997.

[101] Ahlfors, M. (2020, April 6). Hot isostatic pressing with integrated heat treatment. Industrial Heating RSS. Retrieved March 23, 2023, from https://www.industrialheating.com/articles/95589-hot-isostatic-pressing-with-integrated-heat-treatment.

[102] O'Neil, A., Kinzer, B., Bala Chandran, R., & Sahasrabudhe, H. (2023). Improving Structural Integrity of Direct Laser-Deposited Ni–Co–Cr–Al–Y Superalloys by Alloy Modification. Journal of Manufacturing Science and Engineering, 145(2), 021012.

[103] Grange, D., et al. "Processing a non-weldable nickel-base superalloy by Selective Laser Melting: Role of the shape and size of the melt pools on solidification cracking." Materialia 12 (2020): 100686.

[104] Chen, Y., Lu, F., Zhang, K., Nie, P., Hosseini, S. R. E., Feng, K & Chu, P. K. (2016). Investigation of dendritic growth and liquation cracking in laser melting deposited Inconel 718 at different laser input angles. Materials & Design, 105, 133-141.

[105] Yusof, F., and M. F. Jamaluddin. "6.07- Welding Defects and Implications on Welded Assemblies." Comprehensive Materials Processing, S. Hashmi, GF Batalha, C. J. Van Tyne, and B. Yilbas, Eds. Oxford: Elsevier (2014): 125.

[106] Lu, N., Lei, Z., Hu, K., Yu, X., Li, P., Bi, J & Chen, Y. (2020). Hot cracking behavior and mechanism of a third-generation Ni-based single-crystal superalloy during directed energy deposition. Additive Manufacturing, 34, 101228.

[107] Li, Yao, Kai Chen, and Nobumichi Tamura. "Mechanism of heat affected zone cracking in Ni-based superalloy DZ125L fabricated by laser 3D printing technique." Materials & Design150 (2018): 171-181.

[108] Ogawa, T. "Prevention of weld hot cracking." Welding international 5.12 (1991): 931-935.

[109] Lu, Nannan, et al. "Hot cracking behavior and mechanism of a third-generation Ni-based single-crystal superalloy during directed energy deposition." Additive Manufacturing 34 (2020): 101228.

[110] Li, Yao, Kai Chen, and Nobumichi Tamura. "Mechanism of heat affected zone cracking in Ni-based superalloy DZ125L fabricated by laser 3D printing technique." Materials & Design150 (2018): 171-181.

[111] Zhang, X., Chen, H., Xu, L., Xu, J., Ren, X., & Chen, X. (2019). Cracking mechanism and susceptibility of laser melting deposited Inconel 738 superalloy. Materials & Design, 183, 108105.

[112] Kumara, C., Balachandramurthi, A. R., Goel, S., Hanning, F., & Moverare, J. (2020). Toward a better understanding of phase transformations in additive manufacturing of Alloy 718. Materialia, 13, 100862.

[113] McNamara, K., MS Thesis. Pennsylvania State University, (2018).

[114] Kumar, A. Y., Wang, J., Bai, Y., Huxtable, S. T., & Williams, C. B. (2019). Impacts of process-induced porosity on material properties of copper made by binder jetting additive manufacturing. Materials & Design, 182, 108001.

[115] Zhang, Q., Xie, J., Gao, Z., London, T., Griffiths, D., & Oancea, V. (2019). A metallurgical phase transformation framework applied to SLM additive manufacturing processes. Materials & Design, 166, 107618.

[116] Liang, J. J., Wei, H., Zhu, Y. L., Sun, X. F., Jin, T., Hu, Z. Q. & Yao, X. (2011). Influence of Co addition on constituent phases and performance of a NiCrAlYRe alloy system. Surface and Coatings Technology, 205(21-22), 4968-4979.

[117] Li, G., Qu, S., Xie, M., & Li, X. (2017). Effect of ultrasonic surface rolling at low temperatures on surface layer microstructure and properties of HIP Ti-6Al-4V alloy. Surface and Coatings Technology, 316, 75-84.

[118] Qiu, Y., Xin, R., Luo, J., & Ma, Q. (2019). Crack Healing and Mechanical Properties Recovery in SA 508–3 Steel. Materials, 12(6), 890.

[119] Vilanova, M., Garciandia, F., Sainz, S., Jorge-Badiola, D., Guraya, T., & San Sebastian, M. (2022). The limit of hot isostatic pressing for healing cracks present in an additively manufactured nickel superalloy. Journal of Materials Processing Technology, 300, 117398.

[120] Bassini, E., Sivo, A., Martelli, P. A., Rajczak, E., Marchese, G., Calignano, F., ... & Ugues, D. (2022). Effects of the solution and first aging treatment applied to as-built and post-HIP CM247 produced via laser powder bed fusion (LPBF). Journal of Alloys and Compounds, 905, 164213.

[121] Kaplanskii, Y. Y., Zaitsev, A. A., Levashov, E. A., Loginov, P. A., & Sentyurina, Z. A. (2018). NiAl based alloy produced by HIP and SLM of pre-alloyed spherical powders. Evolution of the structure and mechanical behavior at high temperatures. Materials Science and Engineering: A, 717, 48-59.

[122] Teng, Q., Xie, Y., Sun, S., Xue, P., Long, A., Wu, T., Cai, C., Guo, J. and Wei, Q. (2022). Understanding on processing temperature-metallographic microstructure-tensile property relationships of third-generation nickel-based superalloy WZ-A3 prepared by hot isostatic pressing. Journal of Alloys and Compounds, 909, 164668.

[123] Ruttert, B., Ramsperger, M., Roncery, L. M., Lopez-Galilea, I., Körner, C., & Theisen, W. (2016). Impact of hot isostatic pressing on microstructures of CMSX-4 Ni-base superalloy fabricated by selective electron beam melting. Materials & Design, 110, 720-727.

[124] Wang, X., Zhou, Y., Zhao, Z., & Zhang, Z. (2015). The γ′ precipitate rafting and element distribution during hot isostatic pressing in a nickel-based superalloy. Materials & Design, 86, 836-840.

[125] Xu, J., Gruber, H., Deng, D., Peng, R. L., & Moverare, J. J. (2019). Short-term creep behavior of an additive manufactured non-weldable Nickel-base superalloy evaluated by slow strain rate testing. Acta Materialia, 179, 142-157.

[126] Wang, X., Zhou, Y., Dong, J., Wang, T., Zhao, Z. & Zhang, Z. (2016). Microstructural Changes of a Creep-Damaged Nickel-Based K002 Superalloy Containing Hf Element under Different HIP Temperatures. High Temperature Materials and Processes, 35(2), 153-159.

[127] Haynes® 214® alloy. Tensile Properties. (n.d.). https://www.haynesintl.com/alloys/alloy-portfolio_/High-temperature-Alloys/haynes-214-alloy/tensile-properties

[128] Habibi, N., & Wahdatpanah, D. Creep Analysis of the Autofrettage and Non-autofrettage Inconel 100 Super Alloy Thick-walled Spherical Pressure Vessel.

[129] Cers, A. E., & Blatherwick, A. A. (1960). FATIGUE AND STRESS RUPTURE PROPERTIES OF INCONEL 713C, V-57C AND TITANIUM ALLOY 7Al-3Mo-Ti AND MST 821 (8Al-2Cb-1Ta-Ti). Period covered: January 1958 to December 1959 (No. WADD-TR-60-426; AD-243934). Minnesota. Univ., Minneapolis.

[130] Alloy IN-738 Technical Data: A Practical Guide to the Use of Nickel-Containing Aloys NO. 497. (1981) INCO.

[131] Kaufman, M. General Electric Company - Thomson Laboratory. PROPERTIES OF CAST MAR-M-247 FOR TURBINE BLISK APPLICATIONS (1984).

[132] Gordon, J. V., Haden, C. V., Nied, H. F., Vinci, R. P., & Harlow, D. G. (2018). Fatigue crack growth anisotropy, texture and residual stress in austenitic steel made by wire and arc additive manufacturing. Materials Science and Engineering: A, 724, 431-438.

[133] Rangaswamy, P., Griffith, M. L., Prime, M. B., Holden, T. M., Rogge, R. B., Edwards, J. M., & Sebring, R. J. (2005). Residual stresses in LENS® components using neutron diffraction and contour method. Materials Science and Engineering: A, 399(1-2), 72-83.

[134] Zhao, X., Lin, X., Chen, J., Xue, L., & Huang, W. (2009). The effect of hot isostatic pressing on crack healing, microstructure, mechanical properties of Rene88DT superalloy prepared by laser solid forming. Materials Science and Engineering: A, 504(1-2), 129-134.

[135] Weddeling, A., Wulbieter, N., & Theisen, W. (2016). Densifying and hardening of martensitic steel powders in HIP units providing high cooling rates. Powder Metallurgy, 59(1), 9-19.

[136] Rajasekaran, B., Mauer, G., Vaßen, R., Röttger, A., Weber, S., & Theisen, W. (2010). Development of cold work tool steel based-MMC coating using HVOF spraying and its HIP densification behaviour. Surface and coatings technology, 204(23), 3858-3863.

[137] Dahmen, T., Henriksen, N. G., Dahl, K. V., Lapina, A., Pedersen, D. B., Hattel, J. H., ... & Somers, M. A. J. (2021). Densification, microstructure, and mechanical properties of heat-treated MAR-M247 fabricated by Binder Jetting. Additive Manufacturing, 39, 101912.

[138] Burdett, W. B., & Watson, C. T. (2005, January). Hot isostatic pressing of Type 316L powder for a pressure retaining component. In ASME Pressure Vessels and Piping Conference (Vol. 4191, pp. 535-541).

[139] Sulley, J. L., Hookham, I., Burdett, B., & Bridger, K. (2010, January). Introduction of hot isostatically pressed, reactor coolant system components in PWR plant. In International Conference on Nuclear Engineering (Vol. 49330, pp. 357-367).

[140] Wang, H., Chen, L., Dovgyy, B., Xu, W., Sha, A., Li, X., ... & Pham, M. S. (2021). Micro-cracking, microstructure and mechanical properties of Hastelloy-X alloy printed by laser powder bed fusion: As-built, annealed and hot-isostatic pressed. Additive Manufacturing, 39, 101853.

[141] Gan, G., Yang, B., Zhang, X., Zhu, Z., Chen, B., & Gou, G. (2023). Tuning the mechanical properties of powder bed fusion printed CoCrFeNiMn high-entropy alloys by annealing and hot isostatic pressing. Journal of Alloys and Compounds, 946, 169376.

[142] Rao, G. A., Kumar, M., Srinivas, M., & Sarma, D. S. (2003). Effect of standard heat treatment on the microstructure and mechanical properties of hot isostatically pressed superalloy inconel 718. Materials Science and Engineering: A, 355(1-2), 114-125.

[143] Roncery, L. M., Lopez-Galilea, I., Ruttert, B., Huth, S., & Theisen, W. (2016). Influence of temperature, pressure, and cooling rate during hot isostatic pressing on the microstructure of an SX Ni-base superalloy. Materials & Design, 97, 544-552.

[144] Naumenko, D., Shemet, V., Singheiser, L., & Quadakkers, W. J. (2009). Failure mechanisms of thermal barrier coatings on MCrAlY-type bondcoats associated with the formation of the thermally grown oxide. Journal of materials science, 44, 1687-1703.

[145] Svetlizky, D., Das, M., Zheng, B., Vyatskikh, A. L., Bose, S., Bandyopadhyay, & Eliaz, N. (2021). Directed energy deposition (DED) additive manufacturing: Physical characteristics, defects, challenges and applications. *Materials Today, 49*, 271-295.

[146] Gradl, P. R., Protz, C. S., & Wammen, T. (2019). Additive manufacturing and hot-fire testing of liquid rocket channel wall nozzles using blown powder directed energy deposition inconel 625 and JBK-75 Alloys. In *AIAA Propulsion and Energy 2019 Forum* (p. 4362).

[147] Bi, X., Li, R., Li, T., Zhang, X., Cheng, J., & Tian, Y. (2023). Cracks suppression strategies for CoCrNi medium entropy alloy fabricated by laser directed energy deposition. Materials & Design, 226, 111579.

[148] Lu, N., Lei, Z., Hu, K., Yu, X., Li, P., Bi, J., ... & Chen, Y. (2020). Hot cracking behavior and mechanism of a third-generation Ni-based single-crystal superalloy during directed energy deposition. *Additive Manufacturing*, *34*, 101228.

[149] Dang, X., Li, Y., Chen, K., Ramamurty, U., Luo, S., Liang, X., & He, W. (2022). Avoiding cracks in additively manufactured non-weldable directionally solidified Ni-based superalloys. *Additive Manufacturing*, *59*, 103095.